РОССИЙСКИЙ ГОСУДАРСТВЕННЫЙ ПЕДАГОГИЧЕСКИЙ УНИВЕРСИТЕТ им. А. И. ГЕРЦЕНА
HERZEN STATE PEDAGOGICAL UNIVERSITY of RUSSIA

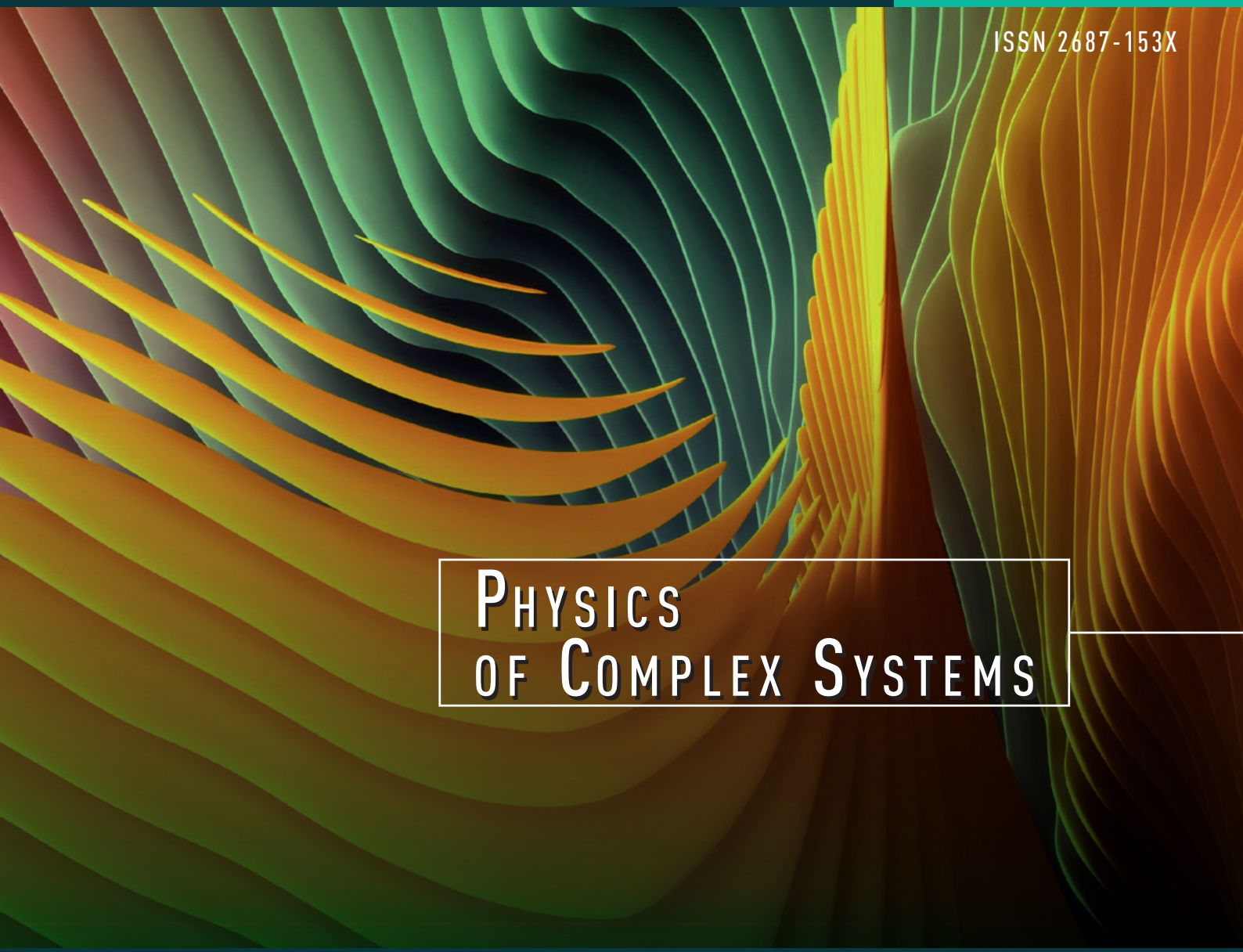

ISSN 2687-153X

Physics of Complex Systems

Т. 7 № 1 2026

Vol. 7 No. 1 2026

Herzen State Pedagogical University of Russia

ISSN 2687-153X (online)
physcomsys.ru
https://www.doi.org/10.33910/2687-153X-2026-7-1
2026. Vol. 7, no. 1

PHYSICS OF COMPLEX SYSTEMS

Mass Media Registration Certificate El No. FS77-77889, issued by Roskomnadzor on 10 February 2020
Peer-reviewed journal
Open Access
Published since 2020
4 issues per year

Publishing house of Herzen State Pedagogical University of Russia
48 Moika Emb., Saint Petersburg 191186, Russia
E-mail: izdat@herzen.spb.ru
Phone: +7 (812) 312-17-41

Data size 11,2 Mbyte
Published at 30.03.2026

Editors of the English text *I. A. Nagovitsyna, K. Yu. Rybachuk*
Corrector *N. A. Sinenikolskaya*
Cover design by *O. V. Rudneva*
Layout by *D. V. Romanova*

Saint Petersburg, 2026

CONTENTS

Physics of Semiconductors.
Solid state physics

UDC 538.915:538.95

EDN SOAOFH
https://www.doi.org/10.33910/2687-153X-2026-7-1-3-15

SERS effect on the surface of ZnO nanorods coated with $CsPbBr_3$

V. A. Gushchina ✉[1], E. P. Averochkin [2], M. A. Teplonogova [1], E. A. Lebedev [2], S. A. Kozyukhin [1]

[1] Kurnakov Institute of General and Inorganic Chemistry of the Russian Academy of Sciences (IGIC RAS),
31 Leninsky Prospekt, Moscow 119991, Russia
[2] National Research University of Electronic Technology (MIET),
1 Shokin Square, Zelenograd, Moscow 124498, Russia

Authors

Valeriya A. Gushchina, ORCID: 0009-0008-9530-1864, e-mail: ya.l2er0us0ya2012@yandex.ru

Evgenii P. Averochkin, ORCID: 0009-0003-4543-3045, e-mail: aep1997@rambler.ru

Maria A. Teplonogova, ORCID: 0000-0002-4820-8498, e-mail: ma_teplonogova@igic.ras.ru

Egor A. Lebedev, ORCID: 0000-0002-5085-5408, e-mail: dr.beefheart@gmail.com

Sergei A. Kozyukhin, ORCID: 0000-0002-7405-551X, e-mail: sergkoz@igic.ras.ru

For citation: Gushchina, V. A., Averochkin, E. P., Teplonogova, M. A., Lebedev, E. A., Kozyukhin, S. A. (2026) SERS effect on the surface of ZnO nanorods coated with $CsPbBr_3$. *Physics of Complex Systems*, 7 (1), 3–15. https://www.doi.org/10.33910/2687-153X-2026-7-1-3-15 EDN SOAOFH

Received 11 December 2025; reviewed 19 January 2026; accepted 20 January 2026.

Funding: The study did not receive any external funding.

Abstract. Heterostructures based on ZnO nanorods and $CsPbBr_3$ nanocrystals were investigated for their potential as semiconductor SERS substrates. We found that ZnO morphology governs the efficiency of interfacial energy transfer, leading to enhanced photoluminescence under 390 nm excitation and a noticeable reduction of the bandgap in the composites. Raman analysis revealed a pronounced intensity enhancement and the emergence of low-frequency $CsPbBr_3$ modes isolated via Gaussian deconvolution, which confirms the SERS-like behavior of the hybrid structures. Our results highlight the strong prospects of ZnO/$CsPbBr_3$ heterostructures for sensing and optoelectronic applications.

Keywords: ZnO nanorods, $CsPbBr_3$ quantum dots, SERS effect, Raman enhancement, heterostructures, energy transfer, low-frequency phonons

Introduction

Over the past decades, rapid development of nanotechnology has opened new avenues in spectroscopy, among which Surface-Enhanced Raman Spectroscopy (SERS) features prominently. Based on the resonant enhancement of the Raman scattering cross-section from molecules adsorbed on metallic nanostructures, this method enables detection limits down to the single-molecule level. For instance, in the case of certain dye molecules adsorbed onto silver colloidal clusters, SERS can provide true single-molecule sensitivity. Moreover, local enhancement factors in specific regions ('hot spots') of metallic clusters can reach values on the order of 10^{10}–10^{12} (Yi et al. 2025). SERS has found widespread application in biomedicine, chemical sensing, photocatalysis, nanolaser technology, and materials science due to its ability to provide detailed information about the chemical composition and structural features of analytes (Ahmed et al. 2019; Kim et al. 2008; Sharma et al. 2012; Vo-Dinh et al. 2015; Song et al. 2022). The central component of the SERS effect is the nanostructured surface, which enables both electromagnetic and chemical enhancement of the Raman signal. The electromagnetic contribution arises from

the intense optical near-field generated in the vicinity of the nanostructure as a result of the resonant excitation of localized surface plasmon oscillations in metallic clusters, which strongly amplifies the Raman response of nearby molecules. The parameters of plasmon resonance excitation and the magnitude of near-field enhancement are governed by the morphology of the nanostructure, the electronic conductivity of the metal, and the dielectric properties of the surrounding medium. Traditionally, noble-metal nanostructures — such as gold and silver nanoparticles — serve as SERS-active substrates, where localized surface plasmon resonances (LSPR) generate electromagnetic 'hot spots' with highly amplified optical fields. For isolated spherical silver nanoparticles, the plasmon resonance typically lies in the ~350–450 nm range, and the corresponding electromagnetic enhancement factors of SERS reach values on the order of 10^6–10^7 (Jin et al. 2016; Xu et al. 2025).

For the adsorbate located in direct contact with the metal surface, an additional SERS enhancement mechanism may arise from the coupling between the molecular electronic orbitals and the conduction-band states of the metal. This phenomenon is referred to as the chemical enhancement mechanism, or, alternatively, first-layer enhancement. The contribution of chemical enhancement is not universal, as it strongly depends on the molecular species and its chemical affinity to the metal surface. The magnitude of this mechanism is generally estimated to be no more than two orders of magnitude (Xia et al. 2014; Zhou et al 2025).

A search for nanostructured materials that can serve as alternatives to gold and silver — while offering lower cost, greater stability, and broader multifunctionality — has stimulated active research into semiconductor nanostructures, including ZnO (Kumar et al. 2021) and perovskite materials such as $CsPbBr_3$ (Wang et al. 2023; Wang et al. 2025).

Zinc oxide, a wide-bandgap semiconductor with an energy gap of approximately 3.3–3.7 eV, has long attracted significant research interest due to its unique optical, electronic, and structural properties. ZnO can adopt a wide variety of morphologies, including nanoparticles, nanorods, nanoneedles, nanocages, and nanoflowers (Averochkin et al. 2024; Deng et al. 2009; Djurisic et al. 2012; Majee et al. 2020; Sinha et al. 2011), which makes it a versatile material for applications in solar energy conversion, optoelectronics, biomedicine, and chemical sensing. These structures also exhibit high biocompatibility, pronounced photocatalytic activity, and excellent chemical stability (Kim et al. 2014; Kumar et al. 2017; Samanta, Bandyopadhyay 2012; Shah 2008). In the context of SERS, ZnO exhibits a strong potential both as an independent nanomaterial and as a component in hybrid systems with noble metals. Electromagnetic enhancement in ZnO-based semiconductor structures arises from plasmonic resonances associated with transitions in the valence and conduction bands; however, this enhancement is considerably weaker than that observed in metals, with the corresponding LSPR features typically located in the UV and near-IR spectral regions (Han et al. 2017). To enhance this effect, ZnO is often combined with metals such as Au or Ag (Chiu et al 2018; Dubkov et al. 2024; Novikov et al. 2021), which shifts the LSPR features into the visible spectral range and facilitates the formation of electromagnetic 'hot spots' through interparticle coupling effects.

Another promising alternative is a class of fully inorganic perovskites of the $CsPbX_3$ type (X = Br, Cl, I), which exhibit exceptional optical properties, including high charge-carrier mobility, bright photoluminescence in the visible range, and a tunable bandgap (Djurisic et al. 2012; Wang et al. 2023; Wang et al. 2025). Fully inorganic perovskites are generally more stable than their hybrid organic–inorganic counterparts, in which the organic cation (e. g., methylammonium, MA^+) is replaced by Cs^+ (Gushchina et al. 2024). Their optical characteristics, including absorption and photoluminescence, strongly depend on composition and nanocrystal size, with bandgap energies ranging from 1.68 to 3.25 eV for $CsPbBr_3$, $CsPbCl_3$, and $CsPbI_3$, respectively (Lee et al. 2025; Miao et al. 2025; Zhao et al. 2023).

Combining ZnO nanorods with $CsPbBr_3$ offers new opportunities for SERS. By integrating a ZnO nanorod surface with a layer of perovskite nanocrystals, it is possible to create heterostructures with enhanced interfacial charge transfer. Such systems enable a simultaneous realization of strong electromagnetic enhancement and additional charge-transfer — mediated (chemical) amplification — while also allowing control over molecular selectivity, since electronic interactions may arise between the analyte molecule and the substrate (Alagurasu et al. 2025). This interaction manifests itself in Fermi-level alignment and the formation of intermediate states that facilitate charge transfer upon excitation. Such processes provide an additional chemical contribution to the overall SERS enhancement, potentially increasing the signal intensity by one to two orders of magnitude beyond that achievable through purely electromagnetic mechanisms (Majumdar et al. 2024). In this context, potential 'hot spots' may arise at the ZnO + $CsPbBr_3$ interface due to defect-induced states in the ZnO nanorods

 https://www.doi.org/10.33910/2687-153X-2026-7-1-3-15

(Wu et al. 2019) or resonance phenomena occurring between the coupled layers (Saran et al. 2017; Toma et al. 2025).

The aim of this work is to fabricate ZnO + $CsPbBr_3$ heterostructures, study their optical properties (optical transmittance and photoluminescence), examine the SERS response, and determine the key parameters governing their enhancement behavior.

Experiment

Reagents. Cs_2CO_3 (99.9%, Sigma-Aldrich), $PbBr_2$ (99.999%, Sigma-Aldrich), oleic acid (OA, 97.4%, Ruskhim), oleylamine (OLA, 98%, Sigma-Aldrich), mineral oil (VM-5c, FOXY), and toluene (reagent grade, Khimmed) were used without further purification. Glass substrates coated with fluorine-doped SnO_2 (FTO, Sigma-Aldrich), hydrogen peroxide (H_2O_2, analytical grade, Ruskhim), H_2SO_4 (high purity grade, Ruskhim), C_3H_8O (reagent grade, Khimmed), $Zn(NO_3)_2{\cdot}6H_2O$ (chemically pure grade, Ruskhim), and NaOH (chemically pure grade, Ruskhim) were also employed.

The suspensions were purified using a Sigma 3-30 KS centrifuge operated at 2,000 and 15,000 rpm.

Surface and fracture images of the samples were obtained using a Tescan Amber GMH scanning electron microscope (SEM). SEM micrographs were acquired with Everhart–Thornley secondary electron detectors and a backscattered electron detector at magnifications of ×1,000–300,000 and an accelerating voltage of 1–10 kV.

Absorption spectra of the colloidal solutions were recorded using a dual-beam Cary 5000 spectrophotometer with a spectral resolution of 0.05 nm. Photoluminescence (PL) spectra were collected at room temperature using a single-beam PerkinElmer LS-55 spectrofluorometer (0.5 nm resolution) in the emission range of 350–600 nm, with excitation wavelengths varied from 300 to 420 nm. The slit widths were set to 5 nm.

Electronic absorption spectra of the colloidal dispersions were acquired using a dual-beam Cary 5000 spectrophotometer, operating at a spectral resolution of 0.05 nm. Steady-state photoluminescence measurements were performed at ambient conditions on a PerkinElmer LS-55 spectrofluorometer (0.5 nm resolution). Emission spectra were collected over the 350–600 nm range, while the excitation wavelength was systematically varied between 300 and 420 nm. Both excitation and emission monochromators were set to a slit width of 5 nm to ensure a well-defined spectral bandwidth and high signal fidelity.

Raman spectra were recorded using a 3D scanning confocal Raman microscope (Confotec NR500, SOL Instruments) with a laser $\lambda = 633$ nm. The spectra were collected in the 50–600 cm^{-1} range using a 600 grooves/mm diffraction grating. A 20× / 0.45 NA dry objective was used for focusing. Signal detection was performed with a PROSCAN CCD detector (16 bit, 2048 × 122 pixels) cooled to −25 °C. The spectra were acquired with an exposure time of 2 s and a single accumulation.

Synthesis of $CsPbBr_3$. A mixture containing Cs_2CO_3 (0.6 mmol), mineral oil (10 mL), and oleic acid (0.625 mL) was loaded into a 50-mL three-neck flask. The suspension was heated to 150 °C under Ar atmosphere with magnetic stirring (500 rpm) until complete reaction of cesium carbonate with oleic acid, yielding a clear brown solution. Separately, $PbBr_2$ (1 g, 2.7 mmol) was combined with mineral oil (20 mL) in another three-neck flask. The mixture was degassed under vacuum (10^{-2} mbar) with continuous stirring (1,000 rpm) and subsequently heated to 160 °C for 1 h. Oleic acid (2 mL) and oleylamine (2 mL) were then added, and once the solution became fully transparent (≈15 min), 6 mL of Cs-oleate was swiftly injected, followed by immediate quenching in an ice bath.

The resulting dispersion was centrifuged at 15,000 rpm for 5 min. Ethyl acetate (EA) was added to induce precipitation, and the mixture was transferred into cuvettes and sonicated for 10 min. The suspension was centrifuged again (15,000 rpm, 5 min), the supernatant removed, and the precipitate redispersed in EA:toluene (2:1), followed by an additional 10-min sonication. The precipitation–centrifugation cycle was repeated twice with EA:toluene ratios of 1:1 and 1:2. The final product was dispersed in toluene, sonicated for 10 min, and centrifuged at 2,000 rpm for 5 min to remove large aggregates. The obtained colloidal solution exhibited bright green photoluminescence.

Synthesis of ZnO Nanorods. FTO-coated glass substrates were first cleaned in a 1:1 mixture of H_2O_2 and H_2SO_4 for 20 min. After cleaning, the substrates were sequentially rinsed with hot and cold deionized water and dried in isopropanol vapor. A chemically resistant lacquer was then applied to the FTO surface. ZnO seed layers were deposited by magnetron sputtering for 20 min at a power of 500 W, with the resulting film thickness varying between the samples. Argon was used as the working gas. Prior to deposition, the substrate surfaces underwent ion cleaning for 2 min. After sputtering, the lacquer

layer was removed mechanically. For the hydrothermal growth precursor solution, $Zn(NO_3)_2 \cdot 6H_2O$ (0.74 g) and NaOH (3.98 g) were dissolved in 250 mL of deionized water at room temperature under stirring at 1,000 rpm for 10 min. The solution was then heated to 80 °C for 10 min. Substrates bearing the ZnO seed layer were immersed face-down into the solution for 30–120 min, depending on the desired nanorod length. During growth, the solution was stirred at 800 rpm. The initial pH of each reaction batch was 13. All syntheses were carried out under ambient pressure. After growth, the ZnO nanorod arrays were rinsed with deionized water and dried at room temperature under a stream of compressed air.

Results and Discussion

Four samples (Fig. 1) were investigated, each of them differing in the morphological parameters of the ZnO nanorods (Table 1), which were grown on FTO-coated substrates and subsequently coated with a layer of $CsPbBr_3$ quantum dots. The diagram illustrates the multilayer architecture of the FTO/ZnO NRs/$CsPbBr_3$ heterostructure, accompanied by TEM images of the perovskite nanocrystals and SEM micrographs of the nanorod arrays.

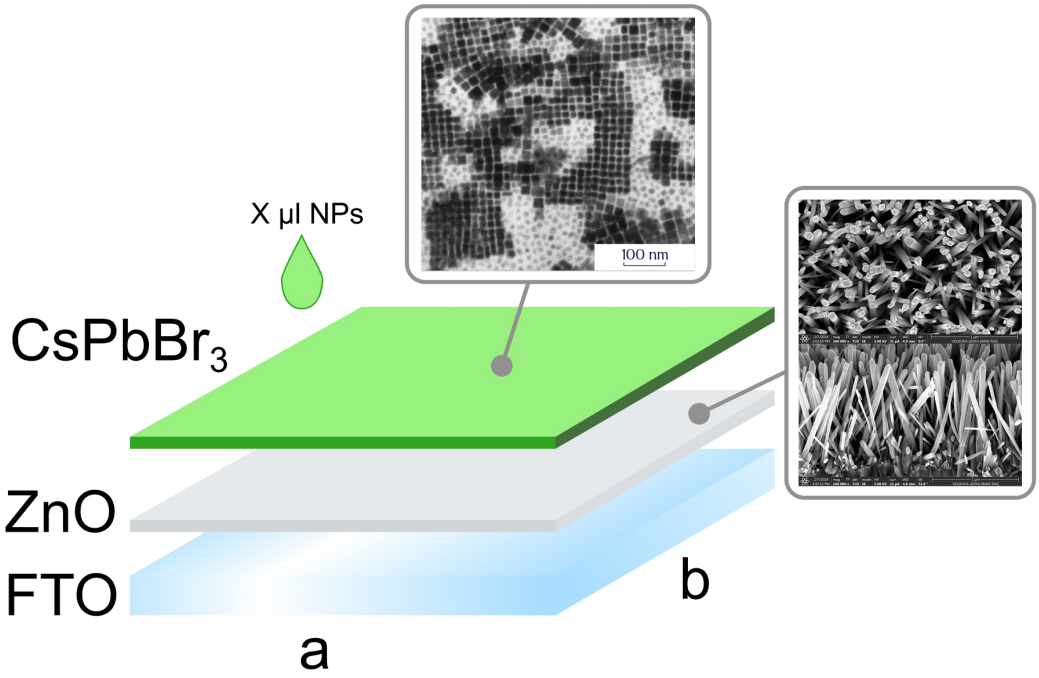

Fig. 1. Diagram of the FTO/ZnO/$CsPbBr_3$ heterostructure

Table 1. Description of the samples

Sample	H NRs, µm	S a. l., mm²	V $CsPbBr_3$, µl
ZnO + $CsPbBr_3$ (1)	1.6 ± 0.1	100	22
ZnO + $CsPbBr_3$ (2)	2.4 ± 0.1	225	50
ZnO + $CsPbBr_3$ (3)	2.7 ± 0.1	192	43

Fig. 2 presents SEM images of ZnO nanorod arrays with various morphologies and corresponding coatings of $CsPbBr_3$ nanoparticles (NPs). Samples a–b serve as references and display a dense, vertically aligned array of pristine ZnO NRs, whereas samples c–h differ in nanorod height (1.6–2.7 µm), which affects the degree of inter-rod filling and the surface coverage density of the deposited perovskite NPs, clearly visible in the top-view images. Cross-sectional views (b, d, f, h) confirm the vertical alignment and thickness variations of the arrays, as well as the distribution of $CsPbBr_3$ across the surfaces and side facets of the nanorods — an important factor for subsequent analysis of the optical and photoelectronic properties of the composite systems.

https://www.doi.org/10.33910/2687-153X-2026-7-1-3-15

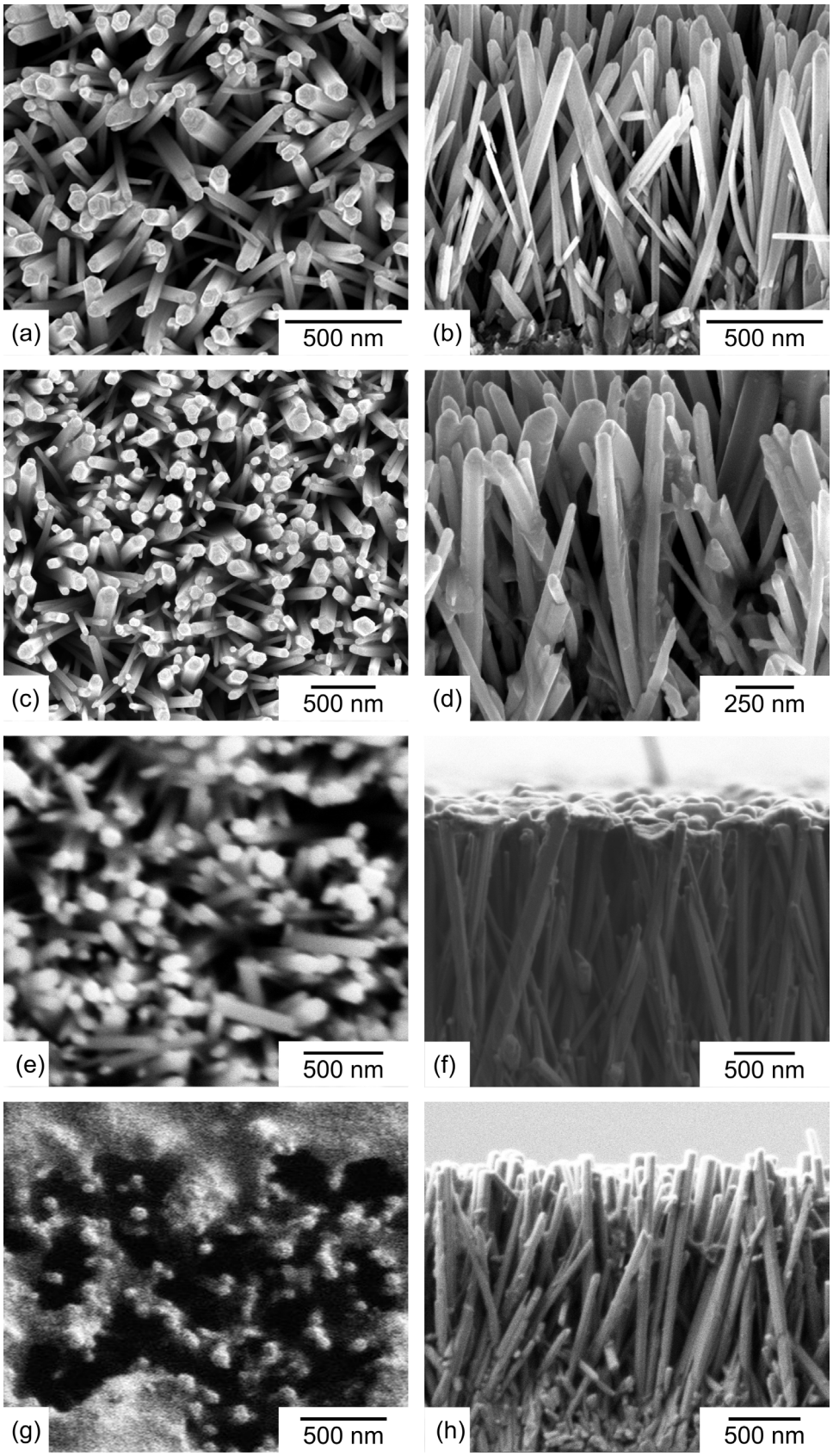

Fig. 2. SEM images of the nanorods and the deposited $CsPbBr_3$: a — ZnO NRs; b — ZnO NRs (fracture); c — 1; d — 1 (fracture); e — 2; f — 2 (fracture); g — 3; h — 3 (fracture)

Across all the three systems (Fig. 3), the ZnO NRs + $CsPbBr_3$ NPs heterostructures exhibit the highest optical density. This enhancement arises from the combined contribution of three factors: an increased effective thickness of the absorbing layer resulting from the incorporation of perovskite NPs into the dense ZnO NR array (Wang et al. 2020); multiple scattering and an extended optical path within the vertically aligned ZnO NRs, which guide and confine the incident radiation (Salem et al. 2025); and the formation of interfacial electronic states at the ZnO + $CsPbBr_3$, which promote stronger absorption and more efficient energy transfer (Peng et al. 2023). Together, these mechanisms lead to an absorption response in the composites that significantly surpasses that of both pristine ZnO NRs and isolated perovskite NPs.

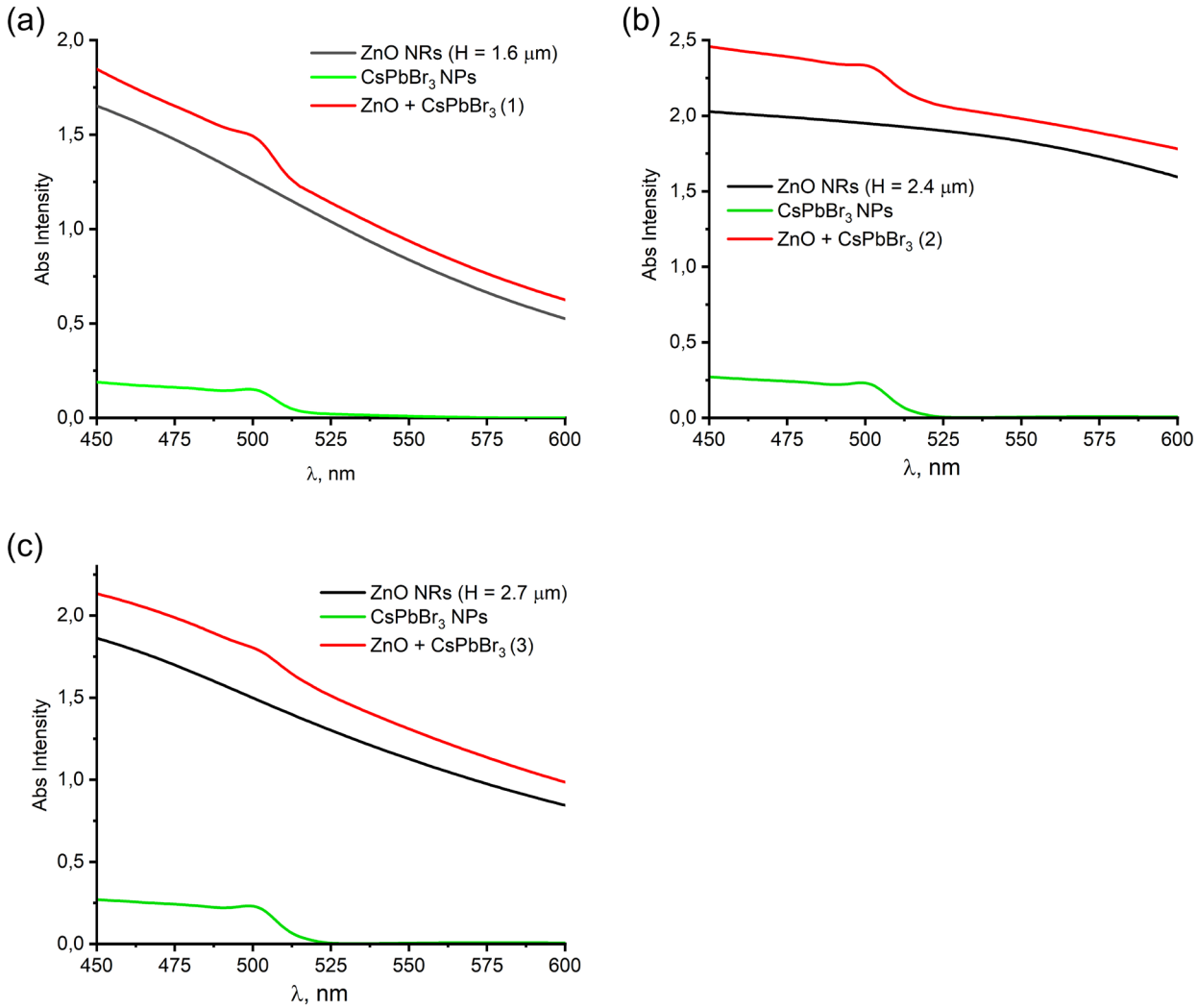

Fig. 3. Absorption spectra of the samples: a — 1 (H = 1.6 μm); b — 2 (H = 2.4 μm); c — 3 (H = 2.7 μm)

The normalized spectra near the absorption edge (Fig. 4) exhibit a characteristic direct band-gap transition with a linear region in the range of ~2.1–2.5 eV. The optical bandgap of the samples was evaluated using the Tauc relation (Tauc, Scott 1967):

$$(\alpha h\nu)^n = B \cdot (h\nu - E_g),$$

where α is the absorption coefficient, h is Planck's constant (6.626×10^{-34} $m^2 \cdot kg \cdot s^{-1}$), ν is the photon frequency, n is the exponent determined by the nature of the electronic transition, and E_g is the optical bandgap energy. Since both ZnO and $CsPbBr_3$ are direct-bandgap semiconductors, the appropriate exponent in this case is n = 2 (Coulter, Birnie 2018).

 https://www.doi.org/10.33910/2687-153X-2026-7-1-3-15

All heterostructures exhibit a reduced bandgap ($E_g \approx 2.20–2.34$ eV) compared to the pristine $CsPbBr_3$ (2.42 eV). This decrease in E_g is attributed to the formation of additional defect-related and surface states at the ZnO + perovskite interface, which introduce a finite density of states near the band edge and facilitate interband transitions at lower energies, resulting in the observed bathochromic shift (Leelavathi et al. 2013).

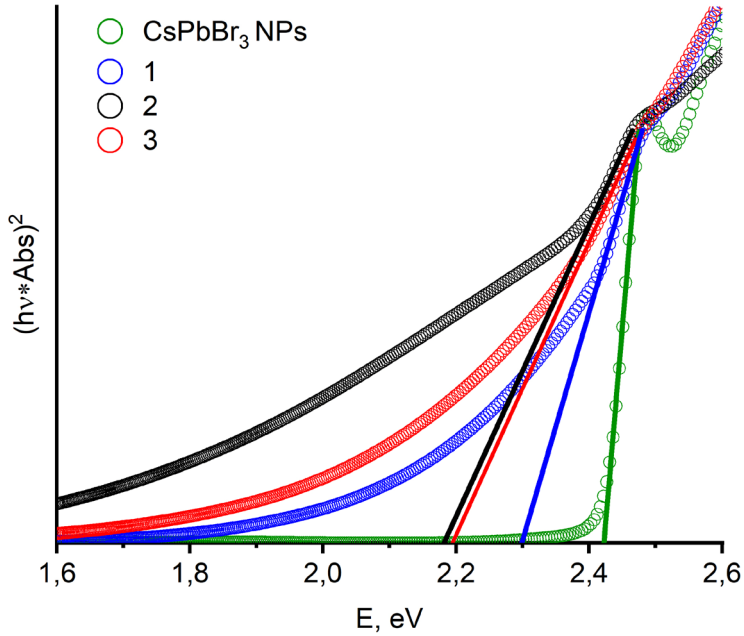

Fig. 4. Normalized absorption spectra of samples near the absorption edge:
1 — H = 1.6 μm; 2 — H = 2.4 μm; 3 — H = 2.7 μm

The most pronounced bathochromic shift and the strongest absorption enhancement are observed for plot 3 (2.7 μm, 50 nm) and plot 2 (2.4 μm, 100 nm), which is attributed to the greater NR height and the more developed interfacial region. These NR arrays provide a larger contact area with the $CsPbBr_3$ layer, including a higher density of grooves, facets, sidewalls, and microscale irregularities capable of hosting the NPs. Collectively, these factors facilitate more efficient modification of the electronic states and enhanced interfacial energy transfer (Leelavathi et al. 2013).

Fig. 5 presents the three-dimensional PL spectra of pristine $CsPbBr_3$ NPs (a) and the ZnO NRs/$CsPbBr_3$ composites with different NR morphologies (b–d). The x-axis corresponds to the photoluminescence wavelength, the y-axis to the PL intensity, and the z-axis to the excitation wavelength, varied from 365 to 400 nm. Pristine $CsPbBr_3$ nanoparticles display an intense and stable emission maximum at ~510 nm for all excitation wavelengths. In the composite samples, a substantial increase in PL intensity is observed, accompanied by a more pronounced dependence on the excitation wavelength: as λ_{exc} increases above ~370 nm, the intensity rises sharply, indicating the involvement of an additional excitation pathway associated with the electronic contribution of the ZnO NRs. In this region, ZnO begins to absorb the excitation light and efficiently transfers energy to the $CsPbBr_3$ NPs through interfacial excited-state transfer processes, leading to enhanced emission from the perovskite NPs (Hasabeldaim et al. 2019; Wu et al. 2005). The magnitude of this enhancement depends on the ZnO NR morphology — specifically their height and diameter — which determines the density of interfacial states and the efficiency of energy transfer, thereby explaining the observed differences among samples 1, 2, and 3.

Fig. 6 shows a projection of the data, equivalent to a rotation of the three-dimensional PL spectra (Fig. 5) such that the excitation wavelength (λ_{exc}) becomes the x-axis, enabling analysis of the evolution of fluorescence as a function of excitation energy. The PL intensity was evaluated at a fixed emission wavelength corresponding to the PL maximum (λ_{em} = 509 nm). The graph reveals that the composite samples exhibit a pronounced increase in intensity within the 370–400 nm region, significantly exceeding the emission levels of the reference $CsPbBr_3$ NPs.

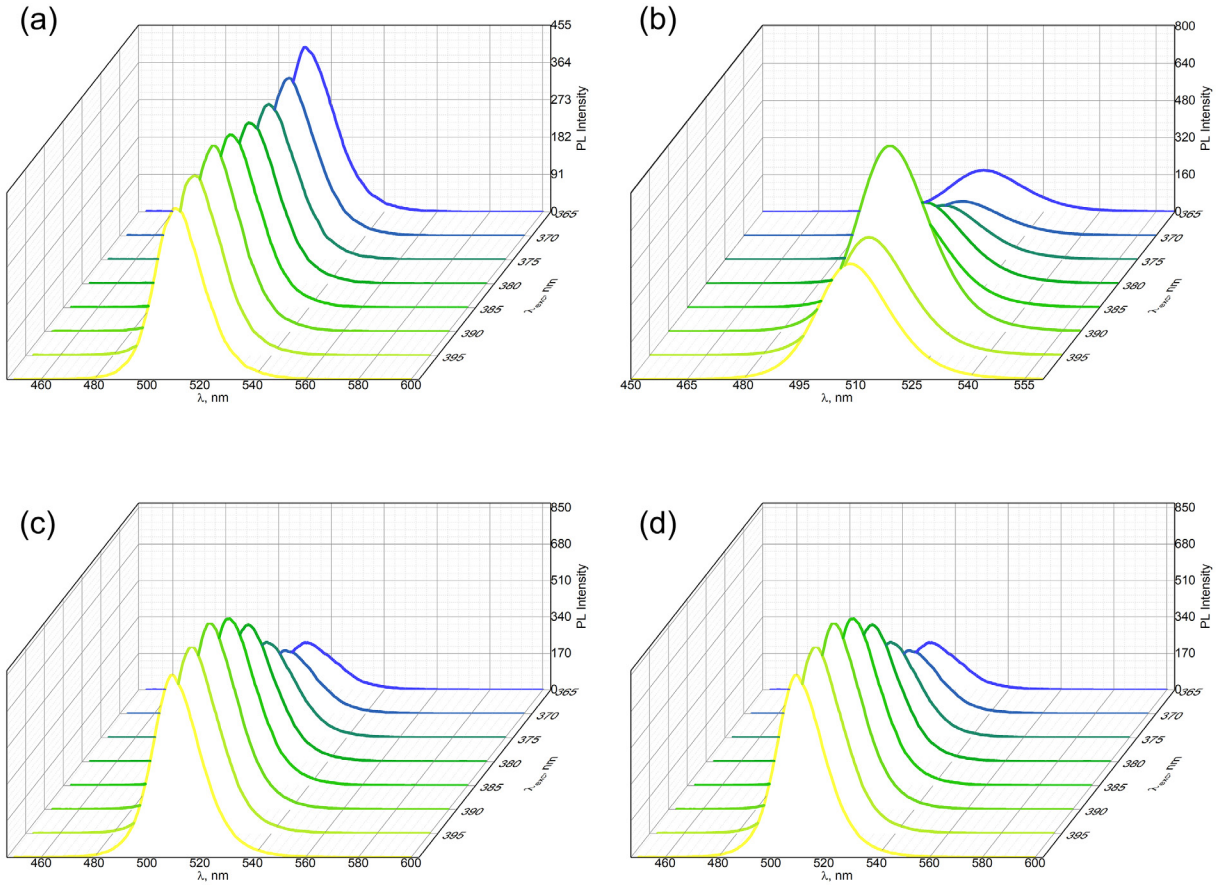

Fig. 5. A series of fluorescence spectra of the samples:
a — $CsPbBr_3$; b — 1 (H = 1.6 μm); c — 2 (H = 2.4 μm); d — 3 (H = 2.7 μm)

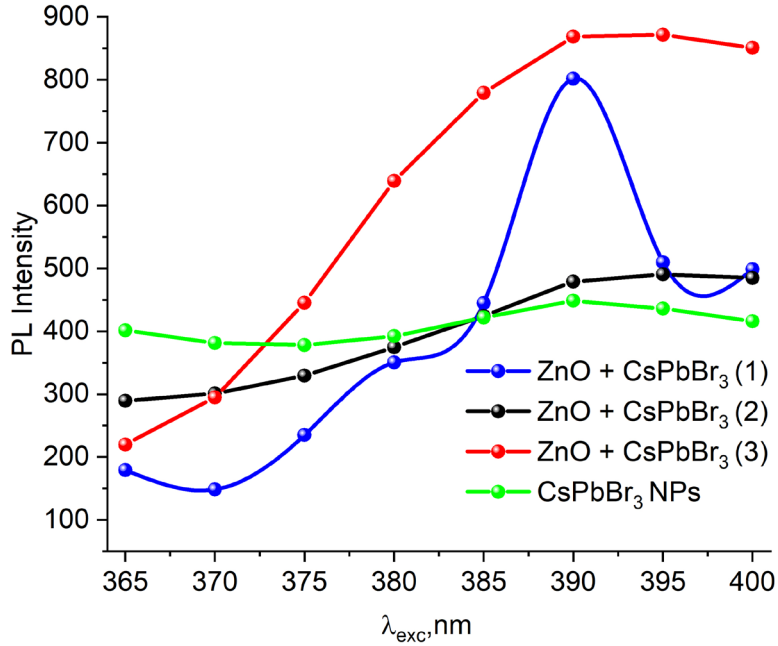

Fig. 6. Dependence of photoluminescence intensity at a fixed emission wavelength of 509 nm on excitation wavelength for ZnO + $CsPbBr_3$ composites and comparison with the reference $CsPbBr_3$: green spectrum — $CsPbBr_3$ NPs; blue — 1 (H = 1.6 μm); black — 2 (H = 2.4 μm); red — 3 (H = 2.7 μm)

https://www.doi.org/10.33910/2687-153X-2026-7-1-3-15

Among the investigated heterostructures, samples 2 (H = 2.4 μm) and 3 (H = 2.7 μm) exhibit the most pronounced and reproducible dependence of photoluminescence intensity on the excitation wavelength. Their spectral profiles are nearly identical in shape, indicating similar mechanisms of interfacial excitation transfer and efficient coupling between the ZnO NRs and the perovskite NPs. Sample 1 (H = 1.6 μm) shows a comparable trend, although its intensity behavior deviates from that of the two selected heterostructures.

Increasing the NR height extends the optical path within the array, enhances light scattering, and promotes deeper penetration of the excitation radiation. These effects raise the probability of ZnO absorption and subsequent energy transfer to $CsPbBr_3$, thereby accounting for the higher photoluminescence observed for the longer NR arrays, such as 2 and 3 (Table 2).

Table 2. Characteristics of the photoluminescence spectra

Sample	$\lambda_{\lambda exc=390\ nm}$, nm	FWHM, nm	Q	Intensity, a.u.	E_g, eV
1	509	23	22.13	802	2.30
2	509.5	20.5	24.85	479	2.18
3	509.5	20.5	24.85	869	2.19
$CsPbBr_3$ NPs	509	21	24.2	448	2.42
ZnO NRs	–	–	–	–	3.22

The same effect plays an important role in the context of SERS. Longer and denser ZnO NRs form a highly developed nanostructured surface with an increased number of electromagnetic 'hot spots,' thereby enhancing local fields and amplifying the Raman response of adsorbed species (Bakry et al. 2024; Korepanov et al. 2019; Thyr et al. 2021). Thus, the morphology that yields higher PL intensity in ZnO + $CsPbBr_3$ heterostructures simultaneously creates favorable conditions for stronger SERS enhancement, as further evidenced by the analysis of the Raman spectra.

In the Raman spectra (Fig. 7) of heterostructures 1, 2, and 3, the $CsPbBr_3$ NPs do not exhibit well-defined vibrational modes. The NPs possess inherently weak Raman activity due to their soft ionic lattice and pronounced anharmonicity, which leads to fluorescence dominating over Raman scattering. In contrast, the ZnO NR substrates display their characteristic phonon modes — E_2 (low) (~99 cm^{-1}), $2E_2$ (~332 cm^{-1}), A_1(TO) (~380 cm^{-1}), and the intense E_2 (high) (~438 cm^{-1}) (Bakry et al. 2024; Korepanov et al. 2019; Thyr et al. 2021).

In the Raman spectra of the ZnO + $CsPbBr_3$ heterostructures, a substantial enhancement of the signal is observed compared to pristine ZnO, indicating the contribution of the perovskite NPs. Additional vibrational features appearing at ~73, 127, 160, and 312 cm^{-1} — identified through multistage Gaussian deconvolution (Fig. 8) — are entirely absent in the spectra of pure ZnO but correspond well to previously reported low-frequency modes of $CsPbBr_3$ (Benadia et al. 2025; Iaru et al. 2021; Li et al. 2021). These modes are typically obscured by strong fluorescence and the inherently weak Raman cross-section of the perovskite; however, in the presence of ZnO NRs, they become enhanced due to local electromagnetic field amplification and the formation of interfacial states at the ZnO + perovskite boundary, consistent with a SERS-like enhancement mechanism.

Conclusions

This work demonstrates that integrating ZnO NRs with $CsPbBr_3$ NPs enables substantial modulation of their optical and vibrational properties through the development of strong interfacial interactions. Analysis of the absorption and photoluminescence spectra revealed that the morphology of the ZnO nanorods — primarily their length — governs the efficiency of energy transfer and the degree of optical enhancement in the hybrid structures. Heterostructures 2 and 3, characterized by greater NR height, exhibit a pronounced bathochromic shift of the absorption edge, the highest PL intensity, and the most favorable conditions for the formation of interfacial electronic states. Raman spectroscopy further confirmed the presence of SERS-like enhancement: in addition to the characteristic ZnO phonon modes, additional low-frequency features corresponding to $CsPbBr_3$ vibrations emerge, enabled

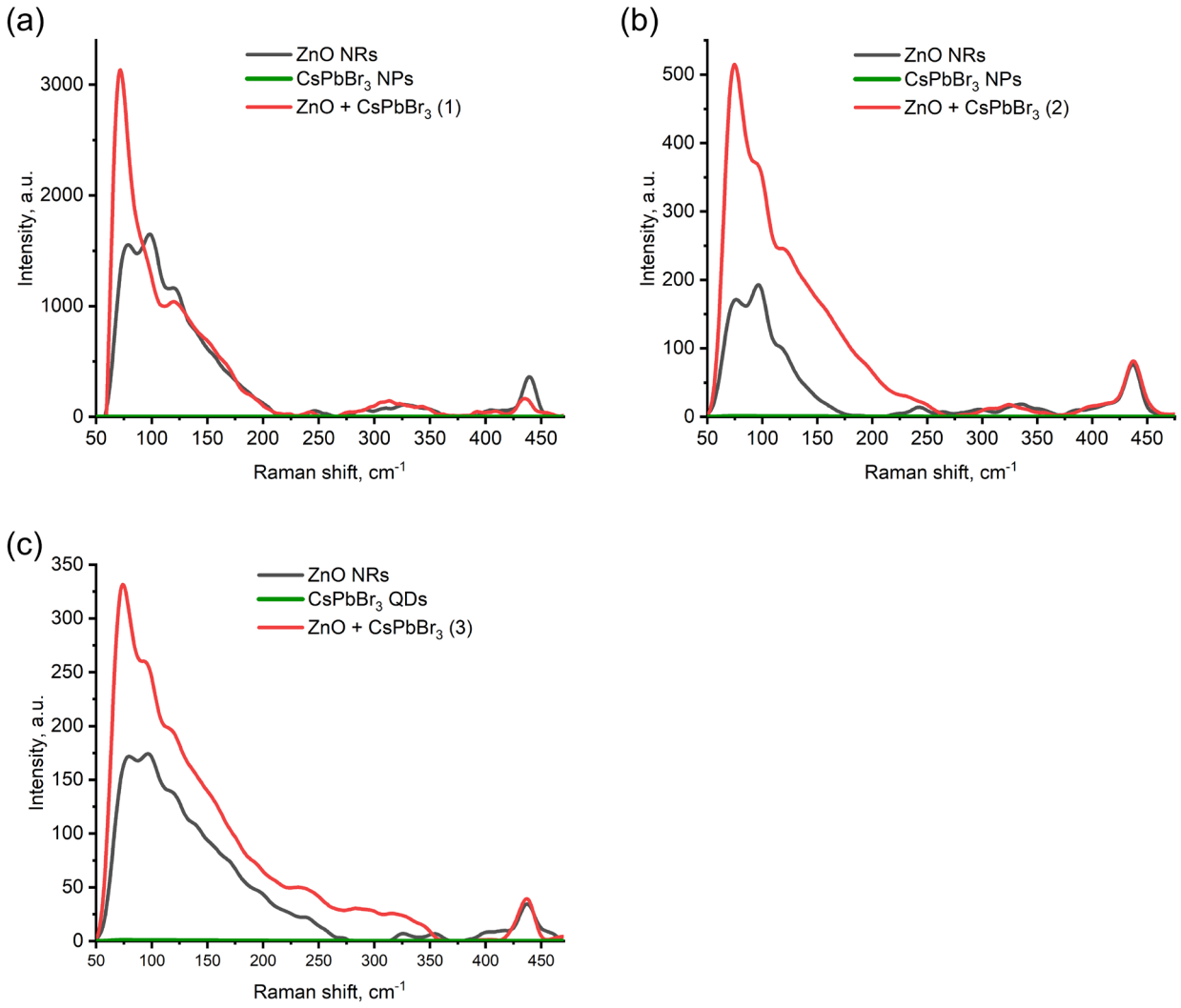

Fig. 7. Raman spectra of heterostructures

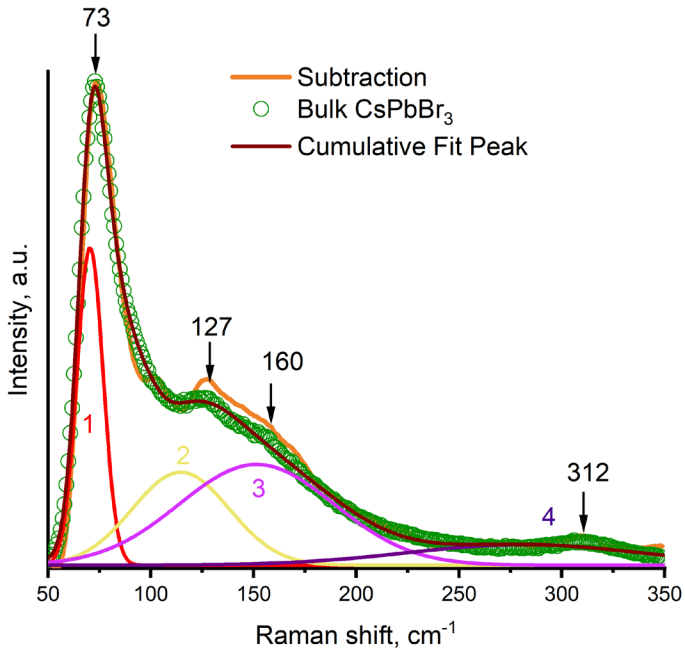

Fig. 8. Revealed low-frequency $CsPbBr_3$ modes enhanced by a ZnO substrate

https://www.doi.org/10.33910/2687-153X-2026-7-1-3-15

by local electromagnetic field amplification and defect-induced interfacial states at the ZnO/perovskite boundary. These findings indicate that ZnO NRs + $CsPbBr_3$ NPs heterostructures represent a promising platform for the development of stable semiconductor-based SERS substrates and hold significant potential for next-generation sensing and optical detection technologies.

Conflict of Interest

The authors declare that there is no conflict of interest, either existing or potential.

Acknowledgements

This research was performed using the equipment of the Joint Research Center of Physical Methods of Research of the Kurnakov Institute of General and Inorganic Chemistry of the Russian Academy of Sciences.

The authors express their deep gratitude to Lydia Sergeevna Volkova, a graduate student at NIU MIET, for her assistance in preparing the manuscript and SEM images of the nanostructures.

Author Contributions

All authors made an equivalent contribution to the preparation of the publication.

References

Ahmed, M. A., Abou-Gamra, Z. M., Alshakhanbeh, M. A. Medien, H. (2019) Control synthesis of metallic gold nanoparticles homogeneously distributed on hexagonal ZnO nanoparticles for photocatalytic degradation of methylene blue dye. *Environmental Nanotechnology, Monitoring & Management*, 12, article 100217. https://doi.org/10.1016/j.enmm.2019.100217 (In English)

Alagurasu, A., Behera, S., Yang, J.-M. et al. (2025) Large-area nanogap platforms for surface-enhanced Raman spectroscopy toward sensing applications: Comparison between Ag and Au. *Biosensors*, 15 (6), article 369. https://doi.org/10.3390/bios15060369 (In English)

Averochkin, E. P., Steparuk, A. S., Teksina, E. V. et al. (2024) Photoactive Layers based on ZnO Nanorods obtained by hydrothermal synthesis for dye-sensitized solar cells. *Russian Journal of Inorganic Chemistry*, 69 (6), 925–932. https://doi.org/10.1134/S0036023624600734 (In English)

Bakry, M., Ismail, W., Abdelfatah, M., El-Shaer, A. (2024) Low-cost fabrication methods of ZnO nanorods and their physical and photoelectrochemical properties for optoelectronic applications. *Scientific Reports*, 14, article 23788. https://doi.org/10.1038/s41598-024-73352-5 (In English)

Benadia, A. G., Pan, L., Bayikadi, K. S. et al. (2025) Progress in solution growth of cuboid $CsPbBr_3$ single crystals with low defect densities and high-sensitivity X-ray detection. *Crystal Growth & Design*, 25 (21), 9288–9299. https://doi.org/10.1021/acs.cgd.5c01107 (In English)

Chiu, Y.-H., Chang, K.-D., Hsu, Y.-J. (2018) Plasmon-mediated charge dynamics and photoactivity enhancement for Au-decorated ZnO nanocrystals. *Journal of Materials Chemistry A*, 6 (10), 4286–4296. https://doi.org/10.1039/C7TA08543E (In English)

Coulter, J. B., Birnie, D. P. III (2018) Degradation mechanism in methylammonium lead iodide perovskite by water: Formation of hydrated HI and PbI2. *Physica Status Solidi B*, 255 (3), article 1700393. https://doi.org/10.1002/pssb.201700393 (In English)

Deng, S., Fan, H. M., Zhang, X. et al. (2009) An effective surface-enhanced Raman scattering template based on a Ag nanocluster–ZnO nanowire array. *Nanotechnology*, 20, article 175705. https://doi.org/10.1088/0957-4484/20/17/175705 (In English)

Djurisic, A. B., Chen, X., Leung, Y. H., Ng, A. M. C. (2012) ZnO nanostructures: Growth, properties and applications. *Journal of Materials Chemistry*, 22, 6526–6535. https://doi.org/10.1039/C2JM15548F (In English)

Dubkov, S. V., Novikov, D. V., Bandarenka, H. V. et al. (2024) Express formation and characterization of SERS-active substrate from a non-degradable Ag-Nb-N-O film. *Applied Surface Science*, 645, article 158682. https://doi.org/10.1016/j.apsusc.2023.158682 (In English)

Gushchina, V. A., Son, A. G., Egorova, A. A. et al. (2024) Synthesis, structures, and optical properties of semiconductor perovskite nanoparticles CsBX3 (B = Pb, Mn; X = Br, Cl). *Russian Journal of Inorganic Chemistry*, 69, 940–948. https://doi.org/10.1134/S0036023624600928 (In English)

Han, X. X., Ji, W., Zhao, B. Ozaki, Y. (2017) Semiconductor-enhanced Raman scattering: active nanomaterials and applications. *Nanoscale*, 9, 4847–4861. https://doi.org/10.1039/C6NR08693D (In English)

Hasabeldaim, E. H. H., Ntwaeaborwa, O. M., Kroon, R. E. et al. (2019) Enhanced green luminescence from ZnO nanorods. *Journal of Vacuum Science & Technology B*, 37 (1), article 011201. https://doi.org/10.1116/1.5052543 (In English)

Iaru, C. M., Brodu, A., van Hoof, N. J. J. et al. (2021) Fröhlich interaction dominated by a single phonon mode in $CsPbBr_3$. *Nature Communications*, 12 (1), article 5844. https://doi.org/10.1038/s41467-021-26192-0 (In English)

Jin, L. She, G., Li, J. et al. (2016) A facile fabrication of Ag-Au-Ag nanostructures with nanogaps for intensified surface-enhanced Raman scattering. *Applied Surface Science*, 389, 67–72. http://dx.doi.org/10.1016/j.apsusc.2016.07.066 (In English)

Kim, K. H., Utashiro, K., Abe, Y., Kawamura, M. (2014) Structural Properties of Zinc Oxide Nanorods Grown on Al-Doped Zinc Oxide Seed Layer and Their Applications in Dye-Sensitized Solar Cells. *Materials*, 7 (4), 2522–2533. https://doi.org/10.3390/ma7042522 (In English)

Kim, S., Jin, J., Kim, Y.-J. et al. (2008) High-harmonic generation by resonant plasmon field enhancement. *Nature*, 453, 757–760. https://doi.org/10.1038/nature07012 (In English)

Korepanov, V. I. Chan, Si-Y., Hsu, H.-C., Hamaguchi, H. (2019) Phonon confinement and size effect in Raman spectra of ZnO nanoparticles. *Heliyon*, 5 (2), article e01222. https://doi.org/10.1016/j.heliyon.2019.e01222 (In English)

Kumar, R., Umar, A., Kumar, G. et al. (2017) Zinc oxide nanostructure-based dye-sensitized solar cells. *Journal of Materials Science*, 52, 4743–4795. https://doi.org/10.1007/s10853-016-0668-z (In English)

Kumar, V., Gupta, R., Bansal, A. (2021) Hydrothermal growth of ZnO nanorods for use in dye-sensitized solar cells. *ACS Applied Nano Materials*, 4, 6212–6222. https://doi.org/10.1021/acsanm.1c01012 (In English)

Lee, S., Cho, S., Jeong, S.-H. et al. (2025) Inverted $CsPbI_3$ perovskite solar cells with all solution processed layers fabricated in high humidity. *Communications Materials*, 6, article 72. https://doi.org/10.1038/s43246-025-00796-1 (In English)

Leelavathi, A., Madrasa, G., Ravishankar, N. (2013) Size-dependent optical properties of ZnO nanocrystals. *Physical Chemistry Chemical Physics*, 15, 10795–10803. https://doi.org/10.1039/C3CP51058A (In English)

Li, S., Yuan, M., Zhuang, W. et al. (2021) Optically-controlled quantum size effect in a hybrid nanocavity composed of a perovskite nanoparticle and a thin gold film. *Laser & Photonics Reviews*, 15 (12), article 2000480. https://doi.org/10.1002/lpor.202000480 (In English)

Majee, B. P., Bhawna, Mishra, A. K. (2020) Bi-functional ZnO nanoparticles as a reusable SERS substrate for nanomolar detection of organic pollutants. *Materials Research Express*, 6, article 1250j1. https://doi.org/10.1088/2053-1591/ab6f31 (In English)

Majumdar, D. (2024) 2D material-based surface-enhanced Raman spectroscopy platforms (either alone or in nanocomposite form)-from a chemical enhancement perspective. *ACS Omega*, 9 (38), 40242–40258. https://doi.org/10.1021/acsomega.4c06398 (In English)

Miao, J., Liu, Y., Xiao, Y. et al. (2025) Water-stable perovskite/metallic nanocomposites-based SERS aptasensor for detection of neuron-specific enolase. *Biosensors and Bioelectronics*, 280, article 117462. https://doi.org/10.1016/j.bios.2025.117462 (In English)

Novikov, D. V., Malakhov, N. S, Tarasov, A. M. et al. (2021) Development of self-cleaning SERS-active nanostructures based on ZnO nanorods and Ag nanoparticles. *Journal of Physics: Conference Series*, 2103, article 012128. https://doi.org/10.1088/1742-6596/2103/1/012128 (In English)

Peng, Y., Jiang, D., Zhao, M. et al. (2023) High-performance UV–visible photodetectors based on ZnO/perovskite heterostructures. *Journal of Alloys and Compounds*, 965, article 171372. https://doi.org/10.1016/j.jallcom.2023.171372 (In English)

Salem, M., Amor, O., Haouas, A. et al. (2025) Improved optoelectronic efficiency of $CsPbBr_3$ perovskite thin films decorated by ZnO nanoparticles. *Optical and Quantum Electronics*, 57, article 446. https://doi.org/10.1007/s11082-025-08383-x (In English)

Samanta, P. K., Bandyopadhyay, A. K. (2012) Chemical growth of hexagonal zinc oxide nanorods and their optical properties. *Applied Nanoscience*, 2, 111–117. https://doi.org/10.1007/s13204-011-0038-8 (In English)

Saran, R., Heuer-Jungemann, A., Kanaras, A. G., Curry, R. J. (2017) Giant bandgap renormalization and exciton–phonon scattering in perovskite nanocrystals. *Advanced Optical Materials*, 5 (17), article 1700231. https://doi.org/10.1002/adom.201700231 (In English)

Shah, M. A. (2008) Zinc oxide nanorods prepared at low temperatures without catalyst. *Modern Physics Letters B*, 22 (26), 2617–2621. https://doi.org/10.1142/S0217984908017126 (In English)

Sharma, B., Frontiera, R. R., Henry, A.-I. (2012) SERS: Materials, applications, and the future. *Materials Today*, 15 (1–2), 16–25. https://doi.org/10.1016/S1369-7021(12)70017-2 (In English)

Sinha, G., Depero, L. E., Alessandri, I. (2011) Recyclable SERS substrates based on Au-Coated ZnO nanorods. *ACS Applied Materials & Interfaces*, 3 (7), 2557–2563. https://doi.org/10.1021/am200396n (In English)

Song, G., Cong, S. Zhao, Z. (2022) Defect engineering in semiconductor-based SERS. *Chemical Science*, 13 (5), 1210–1224. https://doi.org/10.1039/D1SC05940H (In English)

Tauc, J., Scott, T. A. (1967) Direct determination of optical absorption edge in amorphous semiconductors. *Physics Today*, 20 (10), 105–116. https://doi.org/10.1063/1.3033945 (In English)

Thyr, J., Osterlund, L., Edvinsson, T. (2021) Polarized and non-polarized Raman spectroscopy of ZnO crystals: Method for determination of crystal growth and crystal plane orientation for nanomaterials. *Journal of Raman Spectroscopy*, 52 (8), 1395–1405. https://doi.org/10.1002/jrs.6148 (In English)

Toma, F. T. Z., Rahman, M. S., Maria, K. H. (2025) A review of recent advances in ZnO nanostructured thin films by various deposition techniques. *Discover Materials*, 5, 60. https://doi.org/10.1007/s43939-025-00201-1 (In English)

Vo-Dinh, T., Liu, Y., Fales, A. M. et al. (2015) SERS nanosensors and nanoreporters: Golden opportunities in biomedical applications. *WIREs Nanomedicine and Nanobiotechnology*, 7 (1), 17–33. https://doi.org/10.1002/wnan.1283 (In English)

Wang, H., Zhang, P., Zang, Z. (2020) High performance $CsPbBr_3$ quantum dots photodetectors by using zinc oxide nanorods arrays as an electron-transport layer. *Applied Physics Letters*, 116, 162103. https://doi.org/10.1063/5.0005464 (In English)

Wang, J., Zou, L., Yang, M. et al. (2023) Improvement of the stability and optical properties of $CsPbBr_3$ QDs. *Nanomaterials*, 13 (16), article 2372. https://doi.org/10.3390/nano13162372 (In English)

Wang, X., Chen, Y., Zhang, W. et al. (2025) Highly sensitive and reproducible SERS substrates based on a novel 3D waffle-like PMMA–$CsPbBr_3$–Au ternary film. *Sensors and Actuators B: Chemical*, 431, article 137434. https://doi.org/10.1016/j.snb.2025.137434 (In English)

Wu, L., Wu, Y, Lu, W. (2005) Preparation of ZnO Nanorods and optical characterizations. *Physica E*, 28 (1), 76–82. https://doi.org/10.1016/j.physe.2005.02.005 (In English)

Wu, T., Wang, A., Zheng, L. et al. (2019) Evolution of native defects in ZnO nanorods irradiated with hydrogen ion. *Scientific Reports*, 9, article 17393. https://doi.org/10.1038/s41598-019-53951-3 (In English)

Xia, L., Chen, M., Zhao, X. et al. (2014) Visualized method of chemical enhancement mechanism on SERS and TERS. *Journal of Raman Spectroscopy*, 45 (6), 524–530. https://doi.org/10.1002/jrs.4504 (In English)

Xu, Y., Aljuhani, W., Zhang, Y. et al. (2025) A practical approach to quantitative analytical surface-enhanced Raman spectroscopy. *Chemical Society Reviews*, 54 (1), 62–84. https://doi.org/10.1039/D4CS00861H (In English)

Yi, J., You, E. M., Hu, R. et al. (2025) Surface-enhanced Raman spectroscopy: a half-century historical perspective. *Chemical Society Reviews*, 54 (3), article 1453. https://doi.org/10.1039/D4CS00883A (In English)

Zhao, Y., Xu, Y., Jing, X., Ma, W. (2023) SERS-active plasmonic metal NP-$CsPbX_3$ films for multiple veterinary drug residues detection. *Food Chemistry*, 412, article 135420. https://doi.org/10.1016/j.foodchem.2023.135420 (In English)

Zhou, J., Du, Z., Xie, B., Wang, B. (2025) Potential-controlled interfacial charge transfer and chemical enhancement of SERS spectra in plasmonic molecular junctions. *Journal of Physical Chemistry C*, 129 (7), 3646–3652. https://doi.org/10.1021/acs.jpcc.4c07711 (In English)

Physics of Semiconductors.
Computer materials science

UDC 538.9

EDN YXMPGU
https://www.doi.org/10.33910/2687-153X-2026-7-1-16-21

The formation of dimers in the gaseous phase of GeTe as a way to fabricate vacancy-free crystalline thin films

A. V. Kolobov ✉[1, 2]

[1] Institute of Physics, Herzen State Pedagogical University of Russia,
48 Moika Emb., Saint Petersburg 191186, Russia
[2] Research Institute of Physical Studies, Herzen State Pedagogical University of Russia,
48 Moika Emb., Saint Petersburg 191186, Russia

Author

Alexander V. Kolobov, ORCID: 0000-0002-8125-1172**,** e-mail: akolobov@herzen.spb.ru

For citation: Kolobov, A. V. (2026) The formation of dimers in the gaseous phase of GeTe as a way to fabricate vacancy-free crystalline thin films. *Physics of Complex Systems*, 7 (1), 16–21. https://www.doi.org/10.33910/2687-153X-2026-7-1-16-21
EDN YXMPGU

Received 18 December 2025; reviewed 16 January 2026; accepted 16 January 2026.

Funding: The research was supported by an internal grant of Herzen State Pedagogical University of Russia (project No. 43-ВГ).

Abstract. Germanium telluride (GeTe) is a multifunctional material with a plethora of useful properties. In particular, it is one of the best thermoelectric materials. Its thermoelectric properties are affected by intrinsic Ge vacancies that are always present in the crystalline phase because of the low formation energy of such defects. This work draws on ab initio molecular dynamics simulations, demonstrating that due to a very special nature of bonding, often called 'resonant' and/or 'metavalent', the materials evaporate as GeTe dimers rather than individual molecules. We argue that this feature can be used to fabricate oriented vacancy-free GeTe films when the material is thermally evaporated onto a heated templating substrate.

Keywords: phase-change materials, germanium telluride, ab initio molecular dynamics, resonant bonding, evaporation, dimers

Introduction

GeTe is a multifunctional material which is (i) a semiconductor (Li et al. 2025), (ii) a superconductor at high pressure (Cheng et al. 2024), (iii) a ferroelectric (Kolobov et al. 2014), (iv) a material with a giant Rashba effect (Liebmann 2016), (v) one of the best thermoelectric materials (Perumal 2016) and (vi) a prototypical phase-change material (Singh 2023). Obviously, such a plethora of useful properties is determined by its structure. In this work, we demonstrate that despite its three-dimensional structure, strong covalent bonding exists between *pairs of atoms* that form Ge-Te *dimers*. The interaction between the dimers is much weaker, yet it is this weaker interaction that determines the integrity of its crystal structure (Kolobov et al. 2011). This work shows that GeTe consequentially evaporates as dimers rather than individual molecules. We suggest that the dimerised gaseous phase of GeTe may pave the way for fabricating vacancy-free GeTe films.

In order to understand the function, one has to study the structure (Jones 2025). What is therefore unusual about the structure GeTe? The first question is how a cubic structure can be formed when Ge tends to be sp3-hybridised and tetrahedrally coordinated. The reason for the unusual geometry

of bonds in GeTe lies in the mutual electronic configurations of Ge and Te. Germanium is a group 14 element and as such has 2 electrons located on 3 p-orbitals. Consequently, one p-orbital is empty. Tellurium, on the other hand, has 4 electrons on 3 p-orbitals, so that one orbital has two electrons called a 'lone-pair'. This electronic configuration allows for the formation of a cubic structure where one covalent bond is formed using the Te lone-pair electrons as shown in Fig. 1.

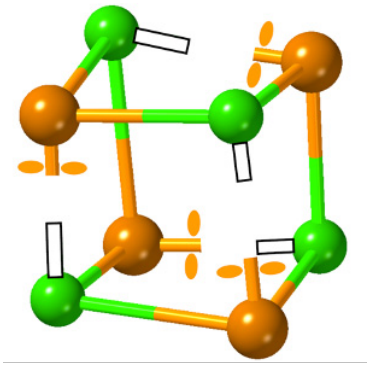

Fig. 1. Formation of a cubic GeTe building block

It is clear that all covalent electrons are consumed in the shown structure. The next question is therefore how a three-dimensional rock-salt structure of GeTe can be formed from these cubes (Fig. 2a). To answer this question, Fig. 2b presents the formation of a covalent bond using two p-orbitals. When the wave functions on the two atoms (shown as '+' and '–' signs in the Figure) have the same symmetry, a covalent bond is formed. On the other hand, when the symmetry is opposite, an antibonding state is formed. One can thus imagine that covalent bonds develop between pairs of Ge and Te atoms with the '+' symmetry of the wave functions along the …Ge–Te–Ge–Te–Ge–Te… atomic sequence in the rock-salt-like structure as shown in Fig. 2c. A careful examination of this linear structure reveals that the symmetry of the wave functions *between* the covalently bonded *pairs* is also the same ('–' as shown in Fig. 2c, above). The same symmetry of the wave functions associated with the back-lobes of the p-orbitals used for bonding suggests that bonding could have taken place between alternative pairs of atoms with the '–' symmetry of the wave functions as shown in Fig. 2c (below).

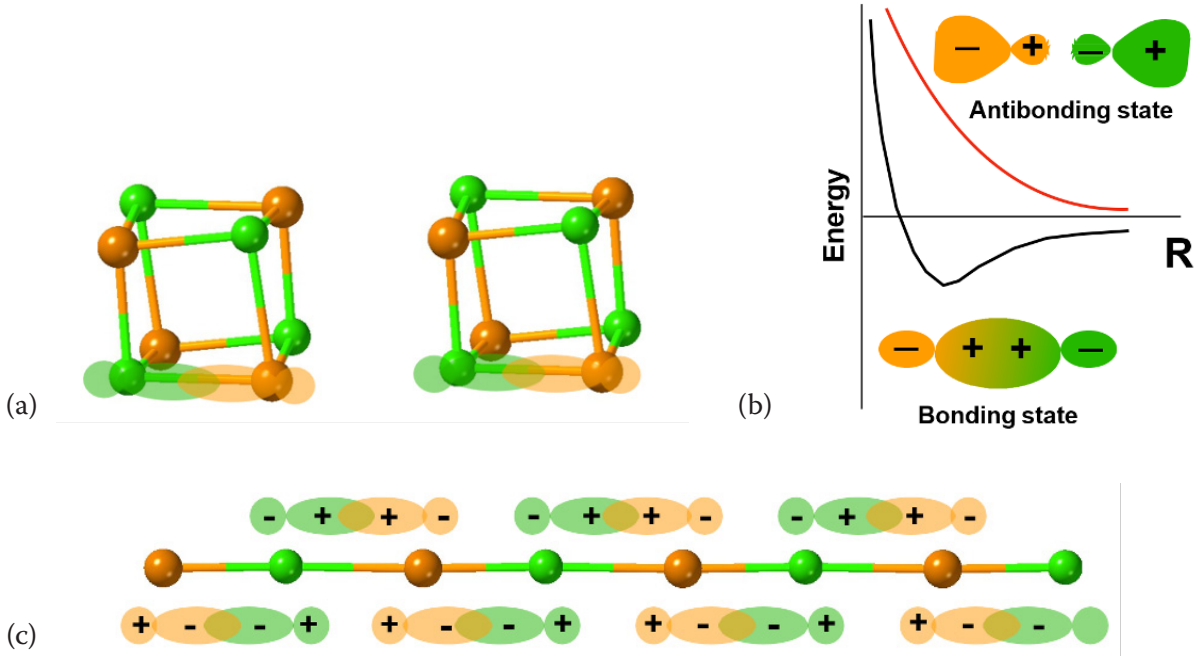

Fig. 2. (a) Individual Ge_4Te_4 cubes with all saturated covalent bonds. (b) Interaction of p-orbitals with the same symmetry (+ and +) leads to the formation of a bonding state, while the orbitals with the opposite symmetry (+ and –) give rise to an antibonding state. (c) Two possible bonding configurations in a linear chain of Ge/Te atoms result in the formation of a resonant/metavalent bond

Since the two structures have the same energy, a resonance between them is possible, and this kind of bonding in GeTe was called 'resonant' in the pioneering paper (Lucovsky, White 1973). Subsequently, the approach was developed in (Shportko 2008), and eventually the term 'metavalent bonding' was suggested (Wuttig 2018). We shall use these terms below, although the concept of metavalency has recently been debated (Jones et al. 2023). Since p-orbitals are orthogonal, the overlap between them is minimal, and the three directions can be considered independently. Within this framework, the structure is a one-dimensional linear chain of alternating Ge and Te atoms. As such, it is subject to the Peierls distortion, which results in the formation of alternating shorter and longer bonds in three directions. In other words, the structure can be viewed as Ge-Te dimers connected by weaker bonds through the back-lobe interaction. It may be interesting to note here that due to the p-orbital bonding Se confined in channels of cancrinite also formed dimers (Kolobov et al. 1999).

(Bragg) neutron diffraction measurements suggested that upon heating to 720 K, the rhombohedral distorted structure with shorter and longer bonds changes to the rock-salt cubic phase with all equal Ge-Te bonds (Chattopadhyay, Boucherle 1987). It should be kept in mind, however, that Bragg diffraction measures the average structure that is not sensitive to local distortions (Stern 1996). Techniques that are sensitive to local distortions, such as extended X-ray absorption fine structure (EXAFS) or pair-distribution function (PDF) analysis of diffraction patterns, unambiguously demonstrated that, in fact, the shorter and longer bonds persist through the ferroelectric-paraelectric transition (Fons et al. 2010; Matsunaga et al. 2011). The presence of the shorter and longer bonds was further found in liquid GeTe, which was named 're-entrant Peierls distortion' (Raty 2000). We note here that this term is apparently incorrect, since, as just mentioned above, the shorter and longer bonds never disappeared in the first place. Since the bonding hierarchy between the shorter and longer bonds persists from low temperature to molten phase, it is thus natural to expect that GeTe will evaporate as Ge-Te dimers when the weaker shorter bonds break, while the stronger shorter bonds will be preserved. This hypothesis was verified in this work by ab initio molecular dynamics (AIMD) simulations.

AIMD simulations were performed using density functional theory (DFT) within the generalized gradient approximation (GGA) with the PBE exchange-correlation functional (Perdew 1996) and the plane wave basis set as implemented in the pseudopotential-based CASTEP code (Clark et al. 2005; Segall 2002). To describe the electron-ionic interactions, Vanderbilt ultrasoft pseudopotentials (Vanderbilt 1990) and cut-off energy $E_{cut\text{-}off}$ = 230 eV were chosen. The starting structure was a GeTe cube with the Te–Ge–Te–Ge atomic sequence (i. e. two connected dimers) along each edge placed in a simulation box with the 30 × 30 × 30 nm size (Fig. 3a). Taking into account the relatively large size of the supercell and consequently the small volume of the Brillouin zone (BZ) used for AIMD simulations, only G-point was used when integrating over the BZ. The GeTe cube was heated to 4,000 K, i. e. well above the melting point (T_m ~ 1,000 K) and held at this temperature for 15 ps. The simulations were carried out using the NVT ensemble with a Langevin thermostat (to maintain ergodicity) with a time step of 4 fs.

As the system was heated and kept at the high temperature, the crystal structure melted, and the evaporation process started. Fig. 3 shows several frames of this process. Note that the simulation box is not shown in the figure. One can see that what is evaporated are not individual molecules but Ge-Te dimers, which confirms the idea that the structure is formed by weakly interconnected dimers.

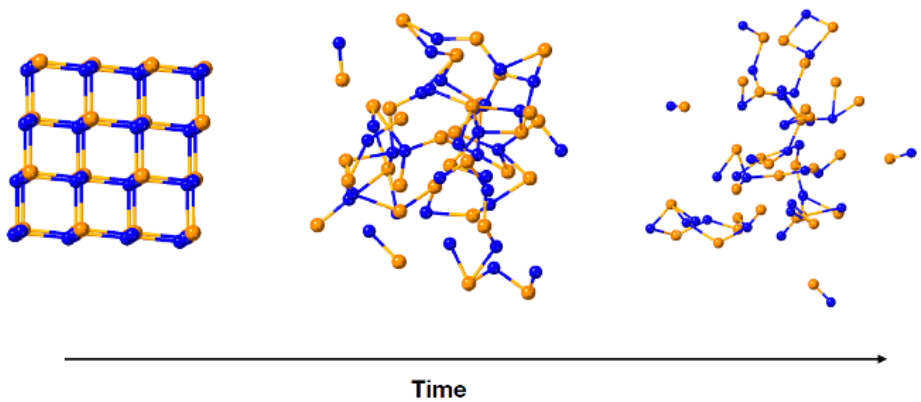

Fig. 3. Ab initio molecular dynamics simulations of the evaporation of GeTe

 https://www.doi.org/10.33910/2687-153X-2026-7-1-16-21

This finding has an important consequence and suggests a way to fabricate vacancy-free GeTe. This is an important technological problem, since bulk GeTe crystals and crystallised GeTe films always contain 5–10% vacancies on Ge sites. Below we propose a way to fabricate vacancy-free GeTe. Indeed, RF sputtering that is usually used for thin film fabrication is a rather energetic process breaking all bonds in the target materials and is likely to generate a flux of individual Ge and Te ions randomly arriving at the substrate and forming a random amorphous chemically disordered network. At the same time, thermal evaporation at elevated temperatures is likely to produce a chemically ordered phase. This is illustrated in Figs. 4 and 5.

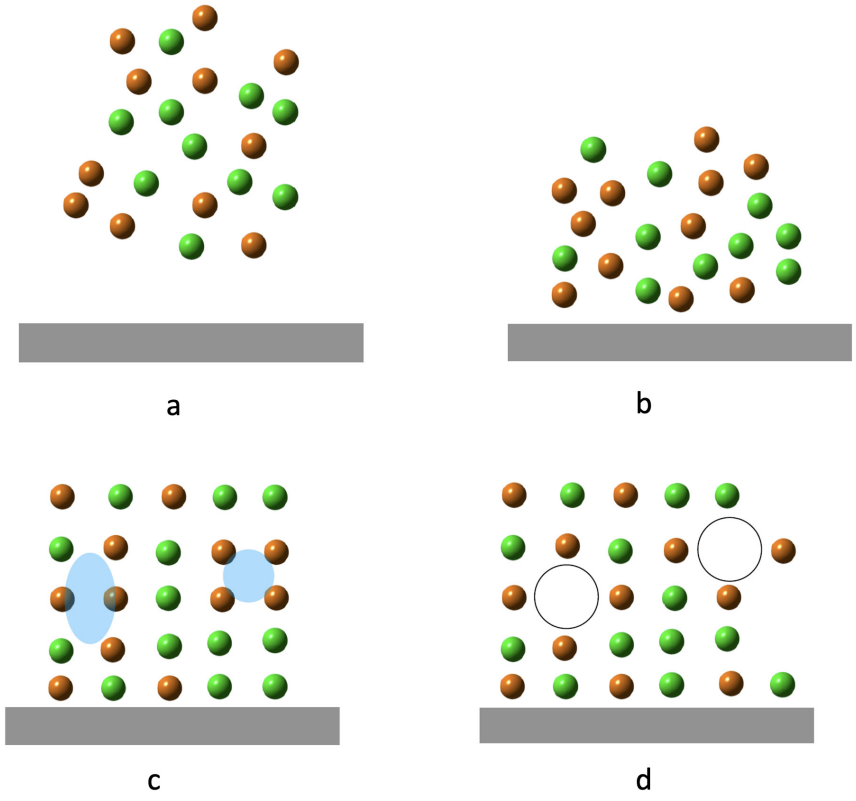

Fig. 4. Vacancy formation upon crystallisation from an amorphous phase. (a) Ge and Te atoms deposition, (b) amorphous phase, (c) chemically disordered crystalline phase. Increased electron density in Te-rich regions (shown in light blue) leads to repulsion between Te atoms leading to the formation of a structure with vacancies

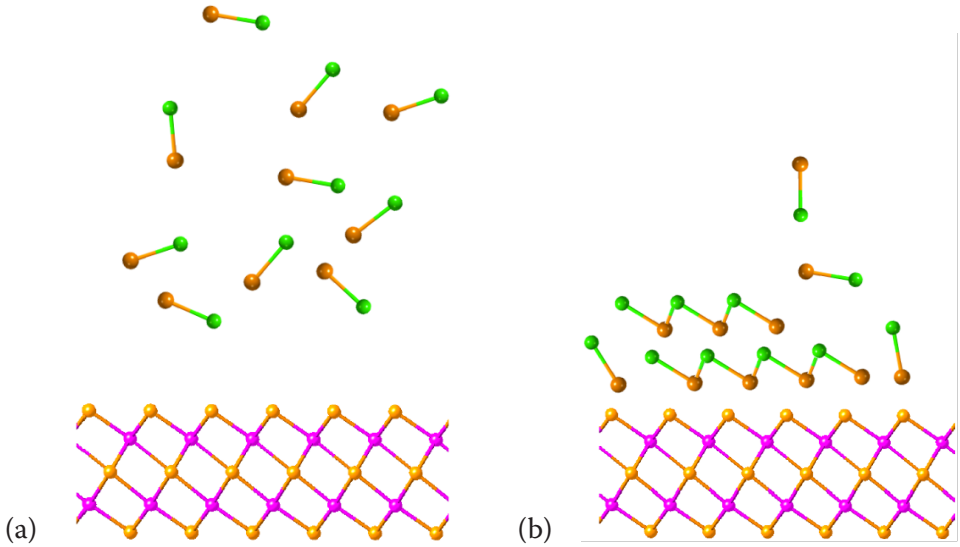

Fig. 5. Formation of vacancy-free GeTe from Ge-Te dimers on a heated templating substrate. (a) Dimers in the vapour phase. (b) Dimers get ordered by the substrate forming vacancy-free GeTe

In the case of RF sputtering, upon crystallisation, there may be Ge-rich and Te-rich microregions as shown in Fig. 4. Since Te atoms possess non-bonding lone-pair electrons, they will repel each other, leading to the formation of vacancies. The presence of vacancies in GeTe films obtained through solid state crystallisation has been demonstrated using EXAFS (Kolobov et al. 2003), and the low formation energy of this process was argued to be the origin of p-type conductivity of GeTe (Edwards et al. 2005).

On the other hand, if a film is obtained by thermal evaporation onto a heated substrate acting as a template, such as Sb_2Te_3 (Simpson 2012), one can expect that dimers, at certain temperature regimes, will arrange themselves into a vacancy-free phase (Fig. 5). Experiments to verify this idea are currently underway. If successful, they may pave the way for creating GeTe with desired vacancy concentration, which may be very beneficial for the fabrication of GeTe-based thermoelectric devices, where the presence and distribution of vacancies play an important role (Zhang 2018).

Conflict of Interest

The authors declare that there is no conflict of interest, either existing or potential.

Acknowledgements

I am grateful to my students for preparing input files for the simulations.

References

Chattopadhyay, T., Boucherle, J. X. (1987) Neutron diffraction study on the structural phase transition in GeTe. *Journal of Physics C: Solid State Physics*, 20 (10), article 1431. https://doi.org/10.1088/0022-3719/20/10/012 (In English)

Cheng, H., Yao, H., Xu, Y. et al. (2024) Pressure-induced alloying and superconductivity in GeTe. *Chemistry of Materials*, 36 (8), 3764–3775. http://dx.doi.org/10.1021/acs.chemmater.4c00087 (In English)

Clark, S. J., Segall, M. D., Pickard, C. J. et al. (2005) First principles methods using CASTEP. *Zeitschrift für Kristallographie — Crystalline Materials*, 220 (5-6), article 567. https://doi.org/10.1524/zkri.220.5.567.65075 (In English)

Edwards, A. H., Pineda, A. C., Schultz, P. A. et al. (2005) Theory of persistent, p-type, metallic conduction in c-GeTe. *Journal of Physics: Condensed Matter*, 17 (32), article L329. https://doi.org/10.1088/0953-8984/17/32/L01 (In English)

Fons, P., Kolobov, A. V., Krbal, M. et al. (2010) Phase transition in crystalline GeTe: Pitfalls of averaging effects. *Physical Review B*, 82 (15), article 155209. https://doi.org/10.1103/PhysRevB.82.155209 (In English)

Jones, R. O. (2025) The properties of solids: "If you want to understand function, study structure". *Journal of Physics: Condensed Matter*, 37, article 113001. http://dx.doi.org/10.1088/1361-648X/ada412 (In English)

Jones, R. O., Elliott, S. R., Dronskowski, R. (2023) The myth of "metavalency" in phase-change materials. *Advanced Materials*, 35 (30), article 2300836. https://doi.org/10.1002/adma.202300836 (In English)

Kolobov, A. V., Kim, D. J., Giussani, A. et al. (2014) Ferroelectric switching in epitaxial GeTe films. *APL Materials*, 2 (6), article 066101. http://dx.doi.org/10.1063/1.4881735 (In English)

Kolobov, A. V., Krbal, M., Fons, P. et al. (2011) Distortion-triggered loss of long-range order in solids with bonding energy hierarchy. *Nature Chemistry*, 3 (4), 311–316. http://dx.doi.org/10.1038/nchem.1007 (In English)

Kolobov, A. V., Oyanagi, H., Poborchii, V. V., Tanaka, K. (1999) Dimerization of single selenium chains confined in nanochannels of cancrinite: An x-ray absorption study. *Physical Review B*, 59 (14), article 9035. https://doi.org/10.1103/PhysRevB.59.9035 (In English)

Kolobov, A. V., Tominaga, J., Fons, P., Uruga, T. (2003) Local structure of crystallized GeTe films. *Applied Physics Letters*, 82 (3), article 382. https://doi.org/10.1063/1.1539926 (In English)

Li, Q., Yang, Z., Yang, X. et al. (2025) Quantum transport simulation of α-GeTe ferroelectric semiconductor transistors. *Journal of Materials Chemistry C*, 13 (2), 568-77. http://dx.doi.org/10.1039/D4TC04706K (In English)

Liebmann, M., Rinaldi, C., Di Sante, D. et al. (2016) Rashba-type spin splitting in ferroelectric GeTe (111). *Advanced Materials*, 28 (3), 560–565. http://dx.doi.org/10.1002/adma.201503459 (In English)

Lucovsky, G., White, R. M. (1973) Effects of resonance bonding on the properties of crystalline and amorphous semiconductors. *Physical Review B*, 15 (2), article 660. http://dx.doi.org/10.1103/PhysRevB.8.660 (In English)

Matsunaga, T., Fons, P., Kolobov, A. V. et al. (2011) The order-disorder transition in GeTe: Views from different length-scales. *Applied Physics Letters*, 99 (23), article 231907. https://doi.org/10.1063/1.3665067 (In English)

Perdew, J. P., Burke, K., Ernzerhof, M. (1996) Generalized gradient approximation made simple. *Physical Review Letters*, 77 (18), article 3865. https://doi.org/10.1103/PhysRevLett.77.3865 (In English)

Perumal, S., Roychowdhury, S., Biswas, K. (2016) High performance thermoelectric materials and devices based on GeTe. *Journal of Materials Chemistry C*, 4 (32), 7520–7536. http://dx.doi.org/10.1039/C6TC02501C (In English)

Raty, J. Y., Godlevsky, V., Ghosez, P. et al. (2000) Evidence of a reentrant Peierls distortion in liquid GeTe. *Physical Review Letters*, 85 (9), article 1950. https://doi.org/10.1103/PhysRevLett.85.1950 (In English)

Segall, M. D., Lindan, P. J. D., Probert, M. J. et al. (2002) First-principles simulation: Ideas, illustrations and the CASTEP code. *Journal of Physics: Condensed Matter*, 14 (11), article 2717. https://doi.org/10.1088/0953-8984/14/11/301 (In English)

Shportko, K., Kremers, S., Woda, M. et al. (2008) Resonant bonding in crystalline phase-change materials. *Nature Materials*, 7 (8), 653–658. http://dx.doi.org/10.1038/nmat2226 (In English)

Simpson, R. E., Fons, P., Kolobov, A. V. et al. (2012) Enhanced crystallization of GeTe from an Sb_2Te_3 template. *Applied Physics Letters*, 100 (2), article 021911. https://doi.org/10.1063/1.3675635 (In English)

Singh, K., Kumari, S., Singh, H. et al. (2023) A review on GeTe thin film-based phase-change materials. *Applied Nanoscience*, 13 (1), 95–110. http://dx.doi.org/10.1007/s13204-021-01911-7 (In English)

Stern, E. A., Yacoby, Y. (1996) Structural disorder in perovskite ferroelectric crystals as revealed by XAFS. *Journal of Physics and Chemistry of Solids*, 57 (10), 1449–1555. http://dx.doi.org/10.1016/0022-3697(96)00012-1 (In English)

Vanderbilt, D. (1990) Soft self-consistent pseudopotentials in a generalized eigenvalue formalism. *Physical Review B*, 41 (11), article 7892. https://doi.org/10.1103/PhysRevB.41.7892 (In English)

Wuttig, M., Deringer, V. L., Gonze, X. et al. (2018) Incipient metals: Functional materials with a unique bonding mechanism. *Advanced materials*, 30 (51), article 1803777. https://doi.org/10.1002/adma.201803777 (In English)

Zhang, X., Li, J., Wang, X. et al. (2018) Vacancy manipulation for thermoelectric enhancements in GeTe alloys. *Journal of the American Chemical Society*, 140 (46), article 15883. https://doi.org/10.1021/jacs.8b09286 (In English)

Physics of Semiconductors.
Functional materials in electronics

UDC 538.915

EDN JKAFHD
https://www.doi.org/10.33910/2687-153X-2025-7-1-22-30

The effects of the precursors $K_2Cr_2O_7$ and NH_4I on the composition, morphology and dark resistance of photosensitive elements based on PbS

K. S. Makaruk ✉[1,2], I. N. Miroshnikova [2], B. N. Miroshnikov [2], A. I. Popov [2], L. N. Maskaeva [3,4], L. S. Volkova [1]

[1] Nanotechnology of Microelectronics Institute, Russian Academy of Sciences, 16A Nagatinskaya Str., Moscow 115533, Russia
[2] National Research University 'Moscow Power Engineering Institute', 14 Krasnokazarmennaya Str., Moscow 111250, Russia
[3] Ural Federal University (named after the First President of Russia B. N. Yeltsin), 19 Mira Str., Yekaterinburg 620002, Russia
[4] Ural Institute of State Fire Service of EMERCOM of Russia, 22 Mira Str., Yekaterinburg 620062, Russia

Authors

Kristina S. Makaruk, ORCID: 0009-0000-6132-3645, e-mail: krismkrk@yandex.ru

Irina N. Miroshnikova, ORCID: 0000-0001-5745-4087, e-mail: miroshnikovain@mpei.ru

Boris N. Miroshnikov, ORCID: 0000-0002-2359-3836, e-mail: miroshnikovbn@gmail.com

Anatoly I. Popov, ORCID: 0000-0002-4078-5303, e-mail: popovai@mpei.ru

Larisa N. Maskaeva, ORCID: 0000-0002-1065-832X, e-mail: larisamaskaeva@yandex.ru

Lidiya S. Volkova, ORCID: 0000-0003-4860-0585, e-mail: lidiya.volkova.96@mail.ru

For citation: Makaruk, K. S., Miroshnikova, I. N., Miroshnikov, B. N., Popov, A. I., Maskaeva, L. N., Volkova, L. S. (2026) The effects of the precursors $K_2Cr_2O_7$ and NH_4I on the composition, morphology and dark resistance of photosensitive elements based on PbS. *Physics of Complex Systems*, 7 (1), 22–30. https://www.doi.org/10.33910/2687-153X-2026-7-1-22-30 EDN JKAFHD

Received 17 December 2025; reviewed 14 January 2026; accepted 15 January 2026.

Funding: The study did not receive any external funding.

Abstract. The results of structural, morphological, and chemical compositional studies of photosensitive elements based on lead sulfide (PbS) thin films are presented. The films were obtained by chemical bath deposition in the presence of one (potassium dichromate — $K_2Cr_2O_7$) or two (ammonium iodide — NH_4I together with $K_2Cr_2O_7$) precursors. The data obtained from scanning electron and atomic force microscopy show that the surface of samples deposited in the presence of only $K_2Cr_2O_7$ consists of crystallites ranging in size from 300 to 900 nm, with a cubic facet. Adding NH_4I to the reaction bath results in a reduction in grain size (more than 75% of the surface consists of crystallites between 100 and 325 nm) and in the appearance of two percent of nanoscale structures (up to 100 nm). At the same time, the surface morphology becomes smoother. It has been established that iodine and its compounds lead to a significant increase in dark resistance (by 10...250 times), which in turn ensures an increase in film sensitivity.

Keywords: lead sulfide, thin films, morphology, chemical deposition method, photosensitive elements

Introduction

Lead sulfide (PbS) is a direct-gap semiconductor with a band gap of 0.4 eV at 300 K and an absorption coefficient of $\alpha \sim 10^5$ cm^{-1} (Ravich et al. 1968). The lifetime of charge carriers in bulk crystals was measured by Moss (Moss 1953), who obtained values from $6 \cdot 10^{-4}$ to 6 μs and attributed these differences to the influence of Auger recombination. According to the Pb–S phase diagram, lead sulfide has an excess of lead atoms relative to sulfur (Naşcu et al. 1996) and is therefore an *n*-type semiconductor.

In order to increase the lifetime of at least one type of charge carriers that determines the main parameters of photosensitive elements (PSEs), technologies for producing thin polycrystalline PbS films have been developing since the 1960s. These films are now used to manufacture PSEs for various optoelectronic systems operating in the IR spectral region from 1 to 3 μm (Butkevich et al. 1999; Baryshev et al. 2000; Pentia et al. 2004; Sadovnikov et al. 2013), sensors for various gases and highly selective sensors for detecting toxic compounds in the air (Burungale et al. 2016; Beatriceveena et al. 2018; Chen et al. 2021), solar cells (Huo et al. 2019, Mengting et al. 2019) and obtain quantum dots (Al-Ahmed et al. 2022; Babaev 2023; Popov et al. 2023; Ren et al. 2017; Shuklov et al. 2020).

Photosensitive polycrystalline films are deposited or sputtered using various methods, which can be divided into 'physical' (thermal evaporation) (Kumar et al. 2003, Patel et al. 2017; Rosario et al. 2019; Singh et al. 2015)) and 'chemical' (spray pyrolysis (Rajashree et al. 2014), SILAR (Successive Ionic Layer Adsorption and Reaction) method (Gülen 2014) and chemical deposition (Ahmed et al. 2020; Markov et al. 2006; Maskaeva et al. 2020; Maskaeva et al. 2019; Palomino-Merino et al. 2013; Touati et al. 2017)).

The chemical bath deposition (CBD) method has a number of advantages: simple equipment is used; films can be deposited on various substrates (Makaruk et al. 2025); and the introduction of precursors during the synthesis process allows for variation in the photosensitive properties of the elements (sensitivity and spectral characteristics). However, none of the numerous theories explaining the behavior of impurities in $A^{IV}B^{VI}$ compounds can predict which element or precursor added to the reaction bath will improve the basic parameters or lead to the development of unusual properties (Maskaeva et al. 2021).

The key technological step in producing highly sensitive structures is sensitization, which involves introducing acceptor-type traps that localize electrons, thereby increasing the hole lifetime. Oxygen, an isoelectronic impurity, is most often used, causing deformation of the PbS crystal lattice and the creation of localized electron trapping centers. The introduction of oxygen, in addition to structural disorder, is accompanied by a violation of the stoichiometric composition, the appearance of a large number of components and phases containing oxygen: PbO, $PbSO_4$, $PbO \cdot PbSO_4$, etc. (Jiang et al. 2021; Quanjiang et al. 2023).

It should be noted that introducing oxygen from a solution during hydrochemical precipitation does not allow for control over the concentration of the introduced impurity. For this reason, other methods for sensitizing the material are currently explored and developed. Common methods for increasing the lifetime of charge carriers include annealing samples in the air (Miroshnikov et al. 2014; Miroshnikov et al. 2015; Mohamed et al. 2014) or two-step annealing: first in an oxygen-containing environment and then in nitrogen (Fan et al. 2023).

To obtain elements with high sensitivity after their synthesis, oxidizing agents are added to the reaction bath beside the main components, which promote inclusion of oxygen atoms in the crystal lattice: H_2O_2, $K_2S_2O_8$ (Blount et al. 1973; Ghamsari et al. 2006; Kul 2019; Naşcu et al. 1996; Wolten 1975), or activators in the form of salts of various metals (silver, mercury, copper, calcium, cadmium, iron (II), gallium, magnesium) (Maskaeva et al. 2017; Simic et al. 1968; Venkoba Rao et al. 1963).

Halogen-containing compounds (for example, with iodine) are able to control the penetration of oxygen into the microcrystallites of the thin-film structure or promote the inclusion of oxygen into the lattice during chemical deposition. In addition, iodine-containing compounds can act as a catalyst, accelerating the formation of oxide phases in the film and ensuring high sensitivity of the PSE due to the penetration of oxygen deep into the grain, which leads to a change in the type of conductivity (Markov et al. 2000; Suh et al. 2016; Maskaeva et al. 2025). As follows from the above studies, doping PbS with iodine changes the photovoltaic parameters due to the formation of point defects in the form of PbI_2. This leads to an inversion of the conductivity type ($n \rightarrow p$) with optimization of the charge carrier concentration in the semiconductor layer.

Sensitization of PbS films with both oxygen and iodine is accompanied by a change in the conductivity type (from *n*-type to *p*-type) and an increase in the concentration of quasi-free holes (Espevik et al.

1971), while the hole lifetime, dark conductivity, and the sensitivity of the photosensitive element also increase.

The chromium (Cr) contained in the precursor (potassium dichromate — $K_2\,Cr_2\,O_7$) is a transition metal that can also influence the parameters of PbS-based photosensitive elements. It was found (Maskaeva et al. 2021) that chromium can use not only the electrons of the outer shell to form chemical bonds, but also d-electrons, which allow changing the concentration of electrons in d-states and having a variable valence (II, III, IV). Information on the photoconductivity of thin-film PbS:Cr cell is presented in the work (Huo et al. 2019), which found that the introduction of chromium leads to an increase in its photoconductivity.

Another study (Maskaeva et al. 2021) showed that the introduction of NH_4I and $CrCl_3$ precursors into the reaction solution preserves the cubic B1 structure of lead sulfide and leads to an increase in the gap width (E_g) by 0.16–0.20 eV, a decrease in the dark resistance R_T and an increase in the voltage sensitivity (U_s). The dependences of E_g and U_s on the chromium salt concentration in the reaction bath exhibit an extreme character with a maximum at 0.016 mol/l, which is due to the non-monotonic incorporation of chromium into the PbS lattice. The results of studies of the current-voltage characteristics of PbS(I) and PbS(I, Cr) thin-film layers are in good agreement with the results of structural, optical, and photosensitive properties.

This work seeks to investigate and compare the morphology, composition, and dark resistance of chemically deposited lead sulfide films obtained in a solution with precursors: potassium dichromate — $K_2\,Cr_2\,O_7$ and ammonium iodide — NH_4I.

Materials and methods

Thin lead sulfide films were synthesized by chemical precipitation from an ammonia-citrate reaction bath containing lead acetate $Pb(CH_3COO)_2$, sodium citrate $Na_3C_6H_5O_7$, ammonium hydroxide NH_4OH, and thiourea N_2H_4CS (source of sulfide ions), with varying concentrations of the oxidizing agent potassium dichromate ($K_2Cr_2O_7$) in a molar content from 10^{-5} mol/l to 10^{-4} mol/l and ammonium iodide (NH_4I) in a molar content of 0.2 mol/l. Film deposition was carried out for 90 min at a temperature of 353 K in sealed molybdenum glass reactors into which degreased glass slide substrates (72.2% SiO_2, 14.3% Na_2O; 1.2% K_2O, 6.4% CaO, 4.3% MgO, 1.2% Al_2O_3, 0.03% Fe_2O_3, 0.3% SO_3) fixed in fluoroplastic fixtures were immersed. The reactors were installed in a TS-TB-10 thermostat with a temperature control accuracy of ±0.1 K. All films were deposited on pre-degreased glass substrates. After synthesis, the samples were rinsed with distilled water and air-dried. The film thickness did not exceed 400 nm. The contacts were formed by electron beam evaporation of a nickel target with a preliminary stage of ion cleaning of the surface from the oxide layer and contaminants.

Film composition was analyzed at five different points on the surface (with subsequent averaging) using X-ray microanalysis on a Vega II SBU scanning electron microscope (Tescan, Czech Republic) equipped with an Inca X-act energy-dispersive spectrometer (Oxford Instruments, UK). The accelerating voltage was 10 kV; the detector acceptance angle, 15°; the working distance, 15 mm; and the data acquisition duration, 60 s.

The morphology of the film samples was studied using scanning electron microscopy (Vega II SBU, Tescan) and atomic force microscopy (AFM) using an INTEGRA Prima NanoLaboratory probe (NT-MDT, Zelenograd). The images were taken using a semicontact scanning technique with an NSG01 cantilever (rigidity 1.45–15.10 N/m). Crystallite size analysis was performed using Gwyddion v. 2.67 software.

The electrophysical parameters of the elements, their current-voltage characteristics, and their contact quality were studied using the ASEC-03E automated measurement system (SKB IRE RAS, Fryazino). The dark resistance of the elements was calculated from the experimental current-voltage characteristics.

Results and discussion

The study of the composition of lead sulfide film samples obtained by chemical deposition from a reaction bath containing the oxidizer $K_2Cr_2O_7$ at concentrations of 10^{-5} mol/l and 10^{-4} mol/l and NH_4I at a concentration of 0.2 mol/l for the main elements (lead, sulfur, and iodine) was carried out using the method of X-ray spectral microanalysis. The atomic oxygen content of the samples was not included in the analysis because the method under consideration is unable to separate the oxygen incorporated into the lead sulfide lattice from the oxygen contained in the glass substrate.

 https://www.doi.org/10.33910/2687-153X-2026-7-1-22-30

The results of measurements averaged over five points for samples obtained only in the presence of potassium dichromate (samples 2 and 4) and for those obtained in the presence of potassium dichromate at concentrations of 10^{-5} mol/l and 10^{-4} mol/l and ammonium iodide (5 and 7) are given in Table 1.

The table demonstrates that all the film samples obtained with an oxidizer have the sulfur content of 51.77–52.22 at.% and the lead content of 47.78–48.23 at.%, at a rough ratio of 1.08. When ammonium iodide is added to the reaction bath, the sulfur content ranges from 51.04 to 51.71 at.% and lead, from 46.77 to 47.42 at.%. The atomic content of iodine changes insignificantly with variations in the oxidizer concentration in the reaction bath. The sulfur to lead ratio is 1.09. According to data available in literature (Suh et al. 2016), lead iodide (PbI_2) and oxide phases PbI_2O_2, Pb_2O_4 are formed in samples deposited with the NH_4I precursor. A slight decrease in the atomic sulfur content in the samples prepared with the additional ammonium iodide precursor, relative to samples obtained using only the oxidizer (potassium dichromate), may indicate the replacement of atoms of the main substance with iodine and/or oxygen.

The stoichiometry between the metal and the chalcogen is not observed in all cases, which indicates the *p*-type conductivity of the considered groups of samples as a result of a lack of lead.

Table 1. Elemental composition and dark resistance of lead sulfide films obtained using different concentrations and combinations of precursors

No.	Composition of the reaction bath, mol/l	[Pb], at. %	[S], at. %	[I], at. %	Dark resistance (R_T, kOhm
1	$K_2Cr_2O_7 = 10^{-5}$	48.23 ± 0.53	51.77 ± 0.53	–	3.3
2	$K_2Cr_2O_7 = 10^{-4}$	47.78 ± 0.47	52.22 ± 0.47	–	15
3	$K_2Cr_2O_7 = 10^{-5}$ $NH_4I = 0.2$	47.42 ± 0.46	51.04 ± 0.21	1.54 ± 0.27	820
4	$K_2Cr_2O_7 = 10^{-4}$ $NH_4I = 0.2$	46.77 ± 0.52	51.71 ± 0.85	1.52 ± 0.43	216

The efficiency of photosensitive elements depends largely on the reflectivity of the incident radiation. Reflectivity, in turn, is determined by the surface morphology of the samples (grain size and shape). Scanning electron microscopy was used to study the effect of the reaction bath composition used for PSE deposition on their surface morphology. Typical images of the PSE surface for the studied sample groups at various magnifications are shown in Figs. 1 and 2. As suggested by the figures, the surface of the samples obtained in the presence of potassium dichromate (Fig. 1) consists of crystallites with a pronounced cubic faceting, characteristic of lead sulfide, which has a face-centered cubic structure of the NaCl (rock salt) type with the space group $Fm\bar{3}m$ (Seghaier et al. 2006). Adding ammonium iodide to the reaction bath smooths the crystallite facets, but individual globules up to one micrometer in size form (Fig. 2). Maskaeva et al. (2021) noted that a similar surface appearance was also observed for chromium-containing samples.

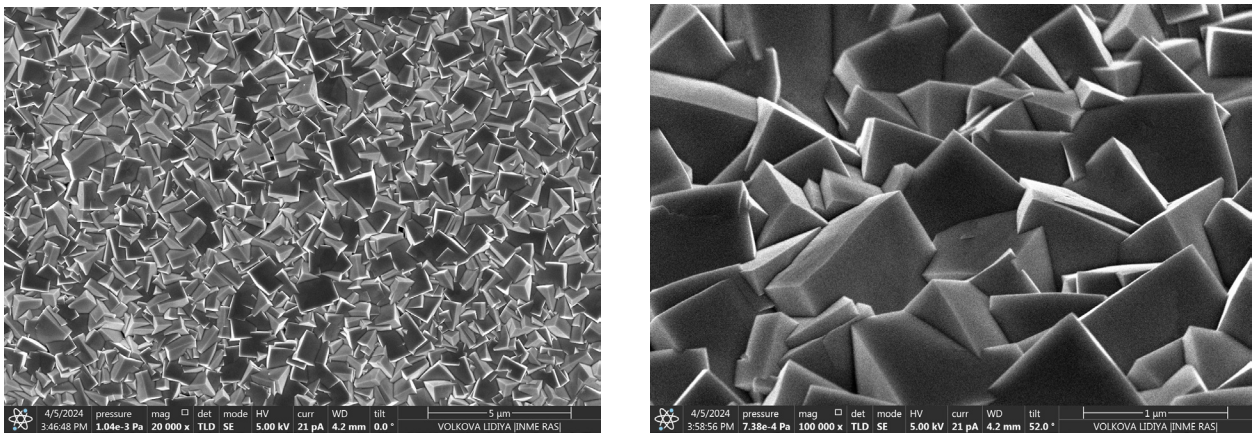

Fig. 1. Electron microscopic images of the surface of a typical sample obtained in a solution with $K_2Cr_2O_7$

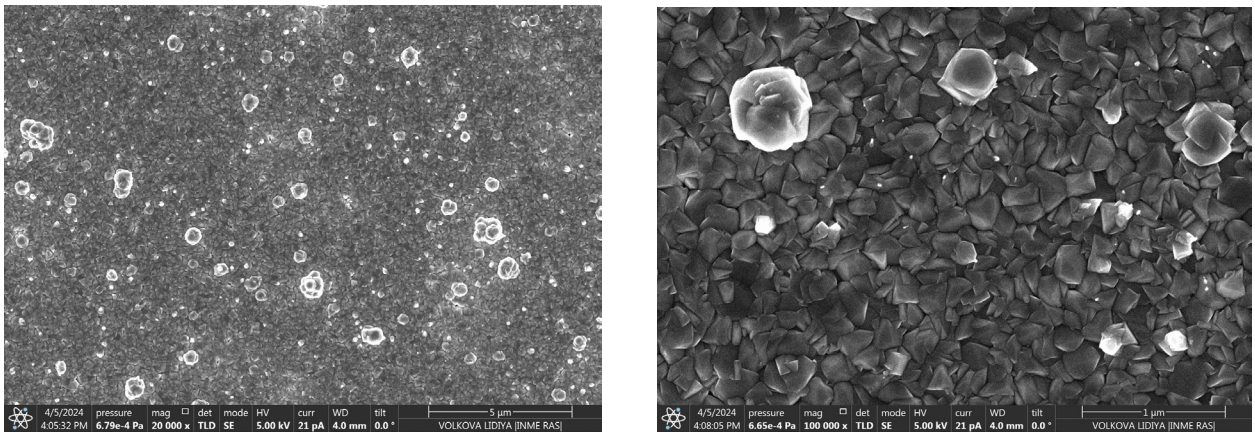

Fig. 2. Electron microscopic images of the surface of a typical sample obtained in a solution with $K_2Cr_2O_7$ and NH_4I

Electron microscopy studies were supplemented by atomic force microscopy (AFM) measurements. The resulting AFM images confirmed the surface morphology data obtained using scanning electron microscopy for two groups of samples (Fig. 3).

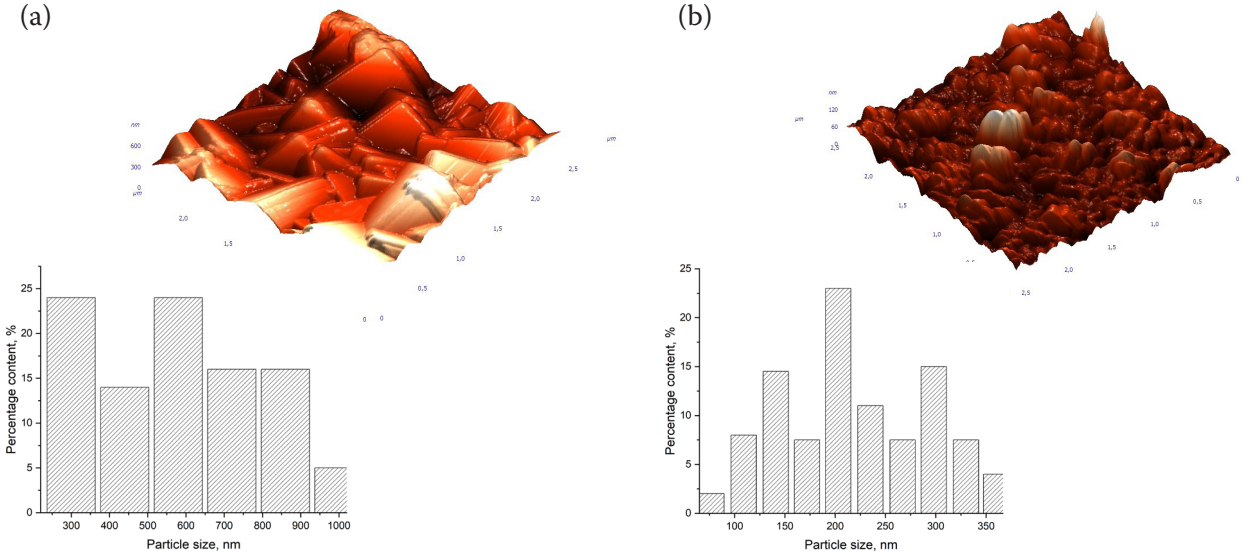

Fig. 3. AFM images of the surface of photosensitive elements based on PbS films chemically deposited in the presence of $K_2Cr_2O_7$ (a) and $K_2Cr_2O_7$ with NH_4I (b). The insets show histograms of the grain size distribution on scans of 5×5 µm^2

The histogram in Fig. 3a was calculated based on the faces of cubic grains. The grain size distribution shows that the samples synthesized in the presence of only the oxidizer are quite homogeneous, as evidenced by the uniform distribution of the percentage of grains ranging in size from 300 to 900 nm. Adding NH_4I to the reaction bath results in a decrease in particle size (histogram in Fig. 3b). Over most of the surface, crystallites range in size from 100 to 325 nm, with approximately two percent of particles smaller than 100 nm present. The presence of nanoscale crystallites can influence the band gap width of the material and, consequently, the spectral dependence of photosensitivity. The obtained data are consistent with the results presented in a study (Markov et al. 2022) in which PbS film samples were deposited in a reaction bath in the presence of ammonium iodide alone. The authors demonstrated that the PSE exhibited a broadening of the band gap and a shift in sensitivity toward higher energies (shorter wavelengths).

Table 2 shows the results of calculating the microrelief parameters of the studied groups of samples, obtained as a result of processing their AFM images.

 https://www.doi.org/10.33910/2687-153X-2026-7-1-22-30

Table 2. Microrelief parameters of the studied groups of samples

Microrelief parameter	Sample number			
	1	2	3	4
Roughness average (R_a), nm	35.63	40.33	12.81	12.17
Root mean square roughness, (R_q), nm	45.51	53.02	18.76	17.65
Maximum average profile height (P_z), nm	228.20	248.50	97.02	116.10

A comparison of the microrelief parameters (roughness (R_a and R_q) and maximum average profile height (P_Z)) can indicate that samples 1 and 2, deposited in the presence of only an oxidizer, have a height difference 2.8–3.3 times greater than samples 3 and 4 with ammonium iodide, which suggests a smoother surface of the latter despite the presence of globules.

Changes in the type and concentration of precursors affect not only the chemical composition and morphology of the resulting samples, but also their electrophysical properties. Table 1 thus shows that elevating the oxidizer (potassium dichromate) concentration in the reaction bath from 10^{-5} mol/L to 10^{-4} mol/L increases the dark resistance of the samples by a factor of 4.5 (from 3.3 to 15 kOhm). The addition of ammonium iodide increases dark resistance by orders of magnitude. Augmenting the oxidizer concentration in the presence of ammonium iodide, however, decreases dark resistance from 820 to 216 kOhm.

The rise in resistance with increasing oxidizer concentration can be explained by the incorporation of more oxygen atoms into the lead sulfide crystal lattice, as well as the possible formation of the oxygen-containing thin layers observed before (Mohamed et al. 2014). Our previous works showed that the presence of ammonium iodide during the deposition of lead sulfide films leads to a decrease in the dark resistance (R_T) compared to samples obtained with the participation of sodium dithionite — $Na_2S_2O_4$ or sodium sulfite — Na_2SO_3 oxidizers. However, this combination demonstrates an increase in dark resistance by 10...250 times at the same concentrations of $K_2Cr_2O_7$. It should be noted that high R_T (low dark conductivity σ_0) contributes to an increase in the sensitivity of the PSE; the sensitivity criterion is not the increase in conductivity (photoconductivity — $\Delta\sigma$), but $\Delta\sigma/(\sigma_0\,\Phi)$, where Φ is the effective value of the radiant power. A decrease in dark conductivity leads to an increase in the sensitivity of the PSE.

Previous results of a study of lead sulfide films deposited in the presence of ammonium iodide using Auger spectroscopy and high-resolution transmission microscopy showed that iodine and oxygen atoms are concentrated to a greater extent near the PSE substrate. Consequently, iodine-containing compounds are formed at the initial stage of film deposition simultaneously with the formation of lead hydroxide crystallization centers — $Pb(OH)_2$. Due to this, the introduction of the ammonium iodide precursor into the reaction bath leads to the formation of a *p*-type conductivity layer near the substrate. As a result, a *p-n* junction is formed, the depth of which depends on the thickness of the iodine-enriched lower layer. This leads to a decrease in the effective cross-section of the *n*-type material and increases the dark resistance of the elements, which explains the significant change in the resistance of the photosensitive element described above.

Conclusion

Polycrystalline films of lead sulfide obtained in solutions with one (potassium dichromate) or two (potassium dichromate and ammonium iodide) precursors were studied.

We showed that the introduction of chromium salt into the reaction mixture neither changes the cubic crystalline structure of lead sulfide nor has a significant effect on the morphology of the films: the crystallite sizes are from 300 to 900 nm and are uniformly distributed over the entire surface of the PSE.

The simultaneous use of potassium dichromate and ammonium iodide precursors leads to a change in the crystallite faceting to a smoother one, a decrease in the particle size (sizes from 100 to 325 nm in the presence of about two percent of particles smaller than 100 nm) and the formation of segregate globules up to one μm in size.

It was established that iodine and its compounds formed at the early stage of thin film deposition lead to a significant increase in the dark resistance of photosensitive elements, which in turn contributes to an increase in their photosensitivity.

The obtained results indicate that the combined use of the precursors $K_2Cr_2O_7$ and NH_4I during the deposition of lead sulfide layers is an effective method for improving the technology of producing photosensitive elements for photoelectronic devices. Further studies of lead sulfide films obtained in a solution containing potassium dichromate will focus on investigating their magnetic properties, as chromium is a d-element, important for the development of spintronics.

Conflict of Interest

The authors declare that there is no conflict of interest, either existing or potential.

Author Contributions

The authors have made an equal contribution to the preparation of the paper.

References

Ahmed, A. M., Rabia, M., Shaban, M. (2020) The structure and photoelectrochemical activity of Cr-doped PbS thin films grown by chemical bath deposition. *RSC Advances*, 10 (24), 14458–14470. https://doi.org/10.1039/c9ra11042a (In English)

Amir, Al-A., Mohammad, A., Nasurullah, M. et al. (2022) The Synergy of Lead Chalcogenide Nanocrystals in Polymeric Bulk Heterojunction Solar Cells. *ACS Omega*, 7 (50), 45981. https://doi.org/10.1021/acsomega.2c06759 (In English)

Babaev, A. A., Skurlov, I. D., Cherevkov, S. A. et al. (2023) PbSe/PbS Core/Shell Nanoplatelets with Enhanced Stability and Photoelectric Properties. *Nanomaterials*, 13 (23), 3051. https://doi.org/10.3390/nano13233051 (In English)

Baryshev, N. S. (2000) *Svojstva i primenenie uzkozonnih poluprovodnikov [Properties and application of narrow-band semiconductors]*. Kazan: UNIPRUSS Publ., 437 p. (In Russian)

Beatriceveena, T. V., Prabhu, E., Sree Rama Murthy, A. et al. (2018) Highly selective PbS thin film based ammonia sensor for inert ambient: In-situ Hall and photoelectron studies. *Applied Surface Science*, 456, 430–436. https://doi.org/10.1016/j.apsusc.2018.06.145 (In English)

Blount, G. H., Schreiber, P. J., Smith, D. K., Yamada, R. T. (1973) Variation of the properties of chemically deposited lead sulfide film with the use of an oxidant. *Journal of Applied Physics*, 44 (3), 978–981. https://doi.org/10.1063/1.1662381 (In English)

Burungale, V. V., Devan, R. S., Pawar, S. A. et al. (2016) Chemically synthesized PbS Nano particulate thin films for a rapid NO2 gas sensor. *Materials Science-Poland*, 34 (1), 204–211. https://doi.org/10.1515/msp-2016-0001 (In English)

Butkevich, V. G., Globus, E. R., Zalevskaya, L. N. (1999) Upravlenie charakteristikami khimicheski osagdennih plenok sernistogo svintsa [Control of the characteristics of chemically deposited lead sulfide films]. *Prikladnaya fizika –Applied Physics*, 2, 52-56. (In Russian)

Chen, X., Hu, J., Chen, P. et al. (2021) UV-light-assisted NO2 gas sensor based on WS2/PbS heterostructures with full recoverability and reliable anti-humidity ability. *Sensors and Actuators B: Chemical*, 339, 129902. https://doi.org/10.1016/j.snb.2021.129902 (In English)

Espevik, S., Wu, C., Bube, R. H. (1971). Mechanism of Photoconductivity in Chemically Deposited Lead Sulfide Layers. *Journal of Applied Physics*, 42 (9), 3513–3529. https://doi.org/10.1063/1.1660763 (In English)

Fan, L., Huang, Z., Lü, Q. et al. (2023) Effect of Two-Step Annealing on Optoelectronic Properties of Lead Sulfide Thin Films. *Acta Optica Sinica*, 43 (10), 1031001. https://doi.org/10.3788/AOS222038 (In English)

Ghamsari, M. S., Araghi, M. K.,Farahani, S. J. (2006) The influence of hydrazine hydrate on the photoconductivity of PbS thin film. *Materials Science and Engineering: B*, 133 (1–3), 113–116. https://doi.org/10.1016/j.mseb.2006.06.021 (In English)

Gülen, Y. (2014) Characteristics of Ba-Doped PbS Thin Films Prepared by the SILAR Method. *Acta Physica Polonica A*, 126 (3), 763–768. https://doi.org/10.12693/aphyspola.126.763 (In English)

Huo, J., Li, W., Wang, T. (2019) Effect of Cr Doping Concentration on the Structural, Optical, and Electrical Properties of Lead Sulfide (PbS) Nanofilms. *Coatings*, 9 (6), 376: https://doi.org/10.3390/coatings9060376 (In English)

Jiang, W. L., Deng, H., Feng, Q., Li, X. Y. (2021) A method for preparing high-quality PbS thin films. *Chalcogenide Lett*, 18, 449. DOI: https://doi.org/10.15251/ cl.2021.188.449 (In English)

Kul, M. (2019) Characterization of PbS film produced by chemical bath deposition at room temperature. *Journal of Science and Technology B- Theoretical Scien*ces, 7 (1), 46. https://doi.org/10.20290/aubtdb.465445 (In English)

Kumar, S., Sharma, T. P., Zulfequar, M., Husain, M. (2003) Characterization of vacuum evaporated PbS thin films. *Physica B: Condensed Matter*, 325, 8–16. https://doi.org/10.1016/s0921-4526(02)01272-3 (In English)

Makaruk, K. S., Beltseva, A. V., Maskaeva, L. N. et al. (2025) Vliyanie podlogki na mikrostrukturu fotochuvstvitelnih elementov na osnove sulfide svintsa [Effect of the substrate on the microstructure of photosensitive elements based on lead sulfide]. In: *XIV International Conference Amorphous and microcrystalline semiconductors*, p. 140. (In Russian)

Markov, V. F., Maskaeva, L. N., Kitaev, G. A. (2000) Microstructure and properties of lead sulfide films deposited from solutions containing ammonium halides. *Inorganic Materials*, 36 (7), 657–659. https://doi.org/10.1007/bf02758415 (In English)

Markov, V. F., Maskaeva, L. N., Ivanov, P. N. (2006) Gidrohimicheskoe osagdenie plenok sulfidov metallov: modelirovanie I eksperiment [Hydrochemical deposition of metal sulfide films: modeling and experiment]. Yekaterinburg: Ural otdelenie Rossijskoj akademii nauk Publ. – Ural Branch of the Russian Academy of Sciences Publ., 216 p. (In Russian)

Markov, V. F., Maskaeva, L. N., Mostovshchikova, E. V. et al. (2022) The influence of iodide addition on the composition, morphology, crystal structure, and semiconductor and photoelectric properties of PbS films. *Physical Chemistry Chemical Physics*, 24, 16085-16100. https://doi.org/10.1039/d2cp01815b (In English)

Maskaeva, L. N., Forostyanaya, N. A., Markov, V. F. et al. (2017) Vliyanie dopantov na funktsionalnie svojstva himicheski osagdennih plenok PbS [The effect of dopants on the functional properties of chemically deposited PbS films]. *Butlerovskie soobshchenia – The Butlerite messages*, 51 (7), 115-124. (In Russian)

Maskaeva, L. N., Mostovshchikova, E. V., Markov, V. F., Voronin, V. I. (2019) Strukturnie, opticheskie i fotochuvstvitelnie svojstva plenok PbS, osagdennih v prisutstvii CaCl2 [Structural, optical, and photosensitive properties of PbS films deposited in the presence of CaCl2]. *Fisika i tehnika poluprivodnikov – Physics and technology of semiconductors*, 53 (2), 174-180. (In Russian)

Maskaeva, L. N., Mostovshchikova, E. V., Voronin, V. I. et al. (2020) Strukturnie, opticheskie i fotochuvstvitelnie svojstva plenok sulfida svintsa, legirovannih strontsiem i bariem [Structure, optical and photoelectric properties of lead sulfide films doped with strontium and barium]. *Fisika i tehnika poluprivodnikov – Physics and technology of semiconductors*, 54 (10), 1041-1051. (In Russian)

Maskaeva, L. N., Mostovshchikova, E. V., Voronin, V. I. et al. (2021) Strukturnie i elektrofizicheskie svoistva plenok PbS, legirovannih Cr^{3+} v protsesse himicheskogo osagdenia [Structural and electrophysical properties of PbS films doped with Cr3+ during chemical deposition]. *Fisika i tehnika poluprivodnikov – Physics and technology of semiconductors*, 55 (10), 937-946. (In Russian)

Maskaeva, L. N., Beltseva, A. V., Mostovshchikova, E. V. (2025) Structural and functional features of photoactive lead sulfide films with iodine-containing impurity phases. *Thin Solid Films*, 817, 140654. https://doi.org/10.1016/j.tsf.2025.140654 (In English)

Mengting, L. Qiuqiang, Z., Wei, L. et al. (2019) Effect of Zn doping concentration on optical band gap of PbS thin films. *Journal of Alloys and Compounds*, 792, 1000-1007. https://doi.org/10.1016/j.jallcom.2019.04.117 (In English)

Miroshnikov, B. N., Miroshnikova I. N., Popov, A. I., Zinchenko, M. Y. (2014) Polycrystalline and Nanocrystalline Photosensitive Layers Based on Lead Sulfide. *Journal of Nanoelectron. and Optoelectron*, 9, 783. https://doi.org/10.1166/jno.2014.1677 (In English)

Miroshnikov, B. N., Miroshnikova, I. N., Mohamed, H. S. H., Popov, A. I. (2015) 1/F α-Type Noise in Lead Sulfide-Based Photosensitive Elements. *Measurement Techniques*, 58 (2), 167–172. https://doi.org/10.1007/s11018-015-0680-8 (In English)

Mohamed, H. S. H., Abdel-Hafiez, M., Miroshnikov, B. N. et al. (2014) Spectral characteristics and morphology of nanostructured Pb–S–O thin films synthesized via two different methods. *Materials Science in Semiconductor Processing*, 27, 725–732. https://doi.org/10.1016/j.mssp.2014.08.010 (In English)

Moss, T. S. (1953) Photoelectromagnetic and Photoconductive Effects in Lead Sulphide Single Crystals. *Proceedings of the Physical Society. Section B*, 66 (12), 993-1002. https://doi.org/10.1088/0370-1301/66/12/301 (In English)

Naşcu, C., Vomi, V., Pop, I. et al. (1996) The study of lead sulphide films. VI. Influence of oxidants on the chemically deposited PbS thin films. *Materials Science and Engineering: B*, 41 (2), 235-240. https://doi.org/10.1016/S0921-5107(96)01611-X (In English)

Palomino-Merino, R., Portillo-Moreno, O., Chaltel-Lima, L. A. et al. (2013) Chemical Bath Deposition of PbS:Hg2+ Nanocrystalline Thin Films. *Journal of Nanomaterials*, 2013 (1), 507647. https://doi.org/10.1155/2013/507647 (In English)

Patel, M. H., Chaudhuri, T. K., Patel, V. K. et al. (2017) Dip-coated PbS/PVP nanocomposite films with tunable band gap. *RSC Advances*, 7(8), 4422–4429. https://doi.org/10.1039/c6ra25935a (In English)

Pentia, E., Draghici, V., Sarau, G. et al. (2004) Structural, Electrical, and Photoelectrical Properties of $Cd_x Pb_{1-x}S$ Thin Films Prepared by Chemical Bath Deposition. *Journal of The Electrochemical Society*, 151 (11), G729. https://doi.org/10.1149/1.1800673 (In English)

Popov, V. S., Ponomarenko, V. P., Dymkin, D. V. et al. (2023) Photosensitivity of the PbS Colloidal Quantum Dot-Based Nanostructures with an Energy Barrier. *Doklady Physics*, 68 (7), 233. https://doi.org/10.1134/S1028335823070066 (In English)

Quanjiang, L., Rongfan, L., Liangchao, F. et al. (2023) High detectivity of PbS films deposited on quartz substrates: the role of enhanced photogenerated carrier separation. *Sensors*, 20, 8413. https://doi.org/10.3390/s2320841322 (In English)

Rajashree, C., Balu, A. R., Nagarethinam, V. S. (2014) Substrate Temperature effect on the Physical properties of Spray deposited Lead sulfide Thin Films suitable for Solar control coatings. *Journal of ChemTech Research*, 6, 347–360. (In English)

Ravich, Yu. I., Efimova, B. A., Smirnov, I. A. (1968) *Metody issledovania poluprovodnikov v primenenii k chalkogenidam svintsa PbTe, PbSe, PbS [Methods of semiconductor research applied to lead chalcogenides PbTe, PbSe, PbS]*. Moscow: Nauka Publ., 383 p. (In Russian)

Ren, Z., Sun, J., Li, H. et al. (2017) Bilayer PbS Quantum Dots for High-Performance Photodetectors. *Advanced Materials*, 29 (33). https://doi.org/10.1002/adma.201702055 (In English)

Rosario, S. R., Kulandaisamy, I., Arulanantham, A. M. S. et al. (2019) Analysis of Cu doping concentration on PbS thin films for the fabrication of solar cell using feasible nebulizer spray pyrolysis. *Materials Research Express*, 6 (5), 056201. https://doi.org/10.1088/2053-1591/aafb9a (In English)

Sadovnikov, S. I., Gusev, A. I. (2013) Structure and properties of PbS films. *Journal of Alloys and Compounds*, 573, 65–75. https://doi.org/10.1016/j.jallcom.2013.03.290 (In English)

Seghaier, S., Kamoun, N., Brini, R., Amara, A. B. (2006). Structural and optical properties of PbS thin films deposited by chemical bath deposition. *Materials Chemistry and Physics*, 97 (1), 71–80. https://doi.org/10.1016/j.matchemphys.2005.07.061 (In English)

Shuklov, I. A., Razumov, V. F. (2020) Lead chalcogenide quantum dots for photoelectric devices. *Russian Chemical Reviews*, 89 (3), 379–391. https://doi.org/10.1070/rcr4917 (In English)

Simić, V. M., Marinković, Ž. B. (1968) Influence of impurities on photosensitivity of chemically deposited lead sulphide layers. *Infrared Physics*, 8 (2), 189–195. https://doi.org/10.1016/0020-0891(68)90008-0 (In English)

Singh, B. P., Kumar, R., Kumar, A., Tyagi, R. C. (2015) Vacuum deposition of stoichiometric crystalline PbS films: The effect of sulfurizing environment during deposition. *Materials Research Express*, 2 (10), 106401. https://doi.org/10.1088/2053-1591/2/10/106401 (In English)

Suh, Y., Suh, S.-H. (2016) Effect of iodine pressure in the sensitization treatment on the structural and electrical properties of PbSe films. *Infrared Sensors, Devices, and Applications*, 9974, 997405. https://doi.org/10.1117/12.2237284 (In English)

Touati, B., Gassoumi, A., Kamoun Turki, N. (2017) Structural, optical and electrical properties of Ag doped PbS thin films: role of Ag concentration. *Journal of Materials Science: Materials in Electronics*, 28 (24), 18387–18395. https://doi.org/10.1007/s10854-017-7785-6 (In English)

Venkoba Rao, H. N., Kuppuswamy, J., Lakshminarayanan, R. (1963) Some Preliminary Studies And Observations On The Chemically Deposited Photosensitive Lead Sulphide Layers. *Indian Journal of Pure and Applied Physics*, 1 (9), 335. (In English)

Wolten, G. M. (1975) A Note on the Chemistry of Lead Sulfide Sensitization for Infrared Detection. *Journal of The Electrochemical Society*, 122 (8), 1149–1150. https://doi.org/10.1149/1.2134413 (In English)

Physics of Semiconductors.
Solid state physics

UDC 538.9

EDN DVYYWY
https://www.doi.org/10.33910/2687-153X-2026-7-1-31-35

Features of copper doping of $PbSb_2Te_4$ crystals

S. A. Nemov ✉[1], A. V. Povolotskiy [2], V. D. Andreeva [3], A. J. Aliabev [1]

[1] St. Petersburg State Electrotechnical University 'LETI' named after V. I. Ulyanov (Lenin),
5F Professora Popova Str., St. Petersburg 197022, Russia
[2] Saint Petersburg State University, 7/9 Universitetskaya Emb., Saint Petersburg 199034, Russia
[3] Peter the Great St. Petersburg State Polytechnical University,
29B Politekhnicheskaya Str., St. Petersburg 195251, Russia

Authors

Sergei A. Nemov, ORCID: 0000-0001-7673-6899, e-mail: nemov_s@mail.ru

Alexey V. Povolotskiy, e-mail: apov@inbox.ru

Valentina D. Andreeva, e-mail: avd2007@bk.ru

Aleksei J. Aliabev, e-mail: alyabjev_au@mail.ru

For citation: Nemov, S. A., Povolotskiy, A. V., Andreeva, V. D., Aliabev, A. J. (2026) Features of copper doping of $PbSb_2Te_4$ crystals. *Physics of Complex Systems*, 7 (1), 31–35. https://www.doi.org/10.33910/2687-153X-2026-7-1-31-35 EDN DVYYWY

Received 13 January 2025; reviewed 03 February 2026; accepted 03 February 2026.

Funding: The study did not receive any external funding.

Abstract. This paper presents the results of X-ray diffraction and Raman spectroscopy studies of Cu-doped $PbSb_2Te_4$ crystals grown by the Czochralski method. Electrophysical properties such as carrier concentration and thermoelectric Q factor ZT are discussed. A rationale is provided for introducing a donor impurity to optimize the properties of crystals as a potential thermoelectric material, and doping features are observed. The Bramfitt heterogeneous nucleation model is applied to calculate disregistry between the parameters of the crystal lattices of the phases occurring in crystals during the growth process. Possible copper-rich phases are predicted. The presence of chemically bound copper atoms forming new phases and their predominant location in the van der Waals gap between the septuple and quintuple layers is confirmed experimentally.

Keywords: semiconductors, $PbSb_2Te_4$, thermoelectricity, Czochralski method, carrier concentration, doping mechanism, Bramfitt heterogeneous nucleation model, X-ray diffraction analysis, Raman spectra, septuple layers

Introduction

Tetradymite-like ternary compounds $PbSb_2Te_4$, which belong to the homologous series $nPbTe{\cdot}mSb_2Te_3$, initially sparked interest among researchers as a basis for obtaining a medium-temperature thermoelectric material of p-type conductivity (Shelimova et al. 2004).

The compound has a complex structure formed from septuple layers (TeSbTePbTeSbTe). The bonds inside the septuple packages are ion-covalent, and the bond between the packages is carried out mainly by weak van der Waals forces. The presence of heavy elements in the composition of the material and the effective scattering of phonons by potential barriers at the boundaries between the layer packages ensure a decrease in lattice thermal conductivity (Shelimova et al. 2008), which is important for achieving high thermoelectric Q-factor (ZT) values (Ioffe 1956).

More interest in these compounds is generated by theory assuming that an ideal periodic structure may have protected surface states that can be localized in both surface and subsurface blocks (Menshchikova

et al. 2013). Such unusual surface properties — the state of a topological insulator — ensure the flow of spin-polarized current without loss of energy, which has the potential for application in quantum computers, spintronics and magneto-electric devices (Jayan, Rakesh 2022).

The first massive single crystals of this compound were grown by the Czochralski method with liquid phase feeding from a floating crucible in the late 2000s at the Institute of Metallurgy of the Russian Academy of Sciences by a team led by L. E. Shelimova. The grown crystals had a diameter of 20 to 30 mm and a length of about 100 mm.

X-ray studies on a Bruker D8 Advance diffractometer in Bragg–Brentano geometry (Cu-Ka radiation with a nickel filter) showed a complex crystal structure with the presence of two phases: the main $PbSb_2Te_4$ (about 70–80%) and Sb_2Te_3 (up to 20–30%). The main phase has rhombohedral symmetry and the spatial group R3m and the parameters of the hexagonal cell a = 0.435 nm and c = 4.171 nm (Nemov et al. 2024). The noted multiphase feature of the crystal structure is presumably caused by the fact that the synthesis of the compound $PbSb_2Te_4$ occurs by a peritectic reaction.

In non-cubic crystals most of the physical properties are tensor ones. The tensors of the main kinetic coefficients, such as electrical conductivity (σ) and thermal conductivity (ϰ), Seebeck coefficients (α) and Hall coefficients (R), are in particular characterized by two components, which are measured in the direction of the inversion-rotation axis of the third order $\bar{3}$ and in the cleavage plane perpendicular to axis $\bar{3}$.

Both components of the Seebeck coefficient tensor in the studied crystals are positive in the temperature range of 77–450 K (Nemov et al. 2012), which corresponds to the hole-like nature of the conductivity. The hole concentration was determined from the larger component of the Hall coefficient tensor at a temperature of 77 K, as is usually done in the study of chalcogenides of elements in group V of the periodic table (Goltsman et al. 1972). It was found that the $PbSb_2Te_4$ crystals have a hole concentration $p \approx (eR)^{-1}$ equal to 3.2×10^{20} cm^{-3}. Such a high concentration of holes in the $PbSb_2Te_4$ indicates a large number of acceptor-type point defects in the crystal lattice caused by a deviation from stoichiometry. Such defects in chalcogenides are vacancies in the metal sublattice. Interestingly, the deviation from the stoichiometric composition of the compound does not lead to a noticeable change in the Hall concentration of holes.

An estimate of the thermoelectric Q factor ZT equal to $ZT = \frac{\alpha^2 \cdot \sigma}{\kappa}$ gives the value of ZT~0.3 at 675 K (Shelimova et al. 2006), which shows that the hole concentration in $PbSb_2Te_4$ is nonoptimal from the point of view of thermoelectric energy conversion. Therefore, to optimize the thermoelectric properties, a significant reduction in the hole concentration is required by modifying the $PbSb_2Te_4$ crystals with electroactive impurities. Copper, which is a donor in lead chalcogenides, was chosen as such impurity. The effect of copper doping of $PbSb_2Te_4$ crystals on their electrophysical properties is studied in this work.

Experimental results and their discussion

As part of optimizing the electrophysical properties of the studied compound, a series of Cu-doped samples with the compositions $(PbTe+Sb_2Te_3)_{0.9995}Cu_{0.0005}$ and $(PbTe+Sb_2Te_3)_{0.999}Cu_{0.001}$ was synthesized and studied (Nemov et al. 2025). Introduction of copper slightly increases the lattice parameter to c = 4.173 nm. At the same time, even a small amount of copper (0.5 atm.%) significantly increases both components of the Hall tensor. It results in almost half as much the concentration of holes compared to the non-doped crystal. Increment of the proportion of the dopant additive in the initial mixture does not lead to a reduced hole concentration.

This fact may be due to a change in the mechanism of the incorporation of dopant atoms into the structure of the initial crystals with dopant proportion. Copper atoms initially fill vacancies in the metal sublattice (Pb, Sb), which leads to a decrease in the hole concentration. With a further increase in the proportion of Cu atoms in the mixture, these atoms begin to settle in the gaps between the septuple and quintuple layers and react with weakly bound Te atoms (the outermost atoms in septuples and quintuples), forming new copper-containing phases.

To calculate the probability of phase formation in doped crystals containing copper chemically bound to the atoms composing the initial compound, as well as to analyze the crystal growth sequence on a temperature scale, we used the Bramfitt nucleation model (Bramfitt 1970) for high-temperature alloys. The Bramfitt heterogeneous nucleation model is a further development of the Turnbull–Vonnegut

 https://www.doi.org/10.33910/2687-153X-2026-7-1-31-35

approach for evaluating the crystallographic interaction at the phase boundary during growth. From the formula

$$\xi_{(hkl)_n}^{(hkl)_s} = \frac{1}{3}\sum_{i=1}^{3} \frac{d_{[uvw]_s^i}\cos\theta - d_{[uvw]_n^i}}{d_{[uvw]_n^i}} \cdot 100\%$$

it is possible to determine the degree of disregistry between the parameters of the crystal lattices of the phases that occur in crystals during the growth process.

The formula uses the following notation: ξ is the lattice disregistry, $(hkl)_s$ is a low-index plane of the substrate, $(hkl)_n$ is a low-index plane of the nucleated solid, $[uvw]_s$ is a low-index direction in $(hkl)_s$, $[uvw]_n$ is a low-index direction in $(hkl)_n$, θ is the angle between $[uvw]_s$ and $[uvw]_n$, $d_{[uvw]s}$ is the interatomic spacing along $[uvw]_s$, and $d_{[uvw]n}$ is the interatomic spacing along $[uvw]_n$.

According to the Bramfitt model, in copper-doped samples, only phases with copper compounds can be observed, the coefficient of disregistry of the lattices with the lattices of the main phases for which does not exceed 6.

Table 1. Bramfitt phase lattice disregistry parameters of the $PbSb_2Te_4$:Cu system

Phase	$PbSb_2Te_4$	$PbSb_2Te_4$	Sb_2Te_3	PbTe	PbTe	Cu_2Te	Cu_2Te	Cu_7Te_4	(CuSb)Te_2
Symmetry	R-3m	R32	R-3m	Fm-3m	Pn-3m	F4-3m	P6/mmm	P3m1	R-3m
Cell type	Rhombohedral			cubic			hexagonal		rhombohedral
d	4.35	4.35	4.25	4.57	5.04	4.364	4.25	4.32	4.22
T_{melt}	800		622	924		900		773	
ξ %	4.7 on PbTe Fm-3m	13.5 on PbTe Pn-3m	2.3 on $PbSb_2Te_4$	–	–	4.5 on PbTe Fm-3m	7.0 on PbTe Fm-3m	5.4 on PbTe Fm-3m	7.54 on PbTe Fm-3m
			7.0 on PbTe Fm-3m	–	–	13.5 on PbTe Pn-3m	15.8 on PbTe Pn-3m	13.3 on PbTe Pn-3m	16.3 on PbTe Pn-3m
			13.5 on PbTe Pn-3m	–	–	-0.3 on $PbSb_2Te_4$	2.3 on $PbSb_2Te_4$	7.0 on $PbSb_2Te_4$	3.0 on $PbSb_2Te_4$

Calculations of the disregistry parameter for the main and copper-containing phases are shown in Table 1. Phases with a value of ξ more than 6, the existence of which is possible based on the phase diagram, could be detected on radiographs in significantly smaller quantities.

The results of X-ray diffraction analysis are shown in Fig. 1. Calculated disregistry values allowed us to estimate the probability of formation of phases with copper that correlates with the experimental results.

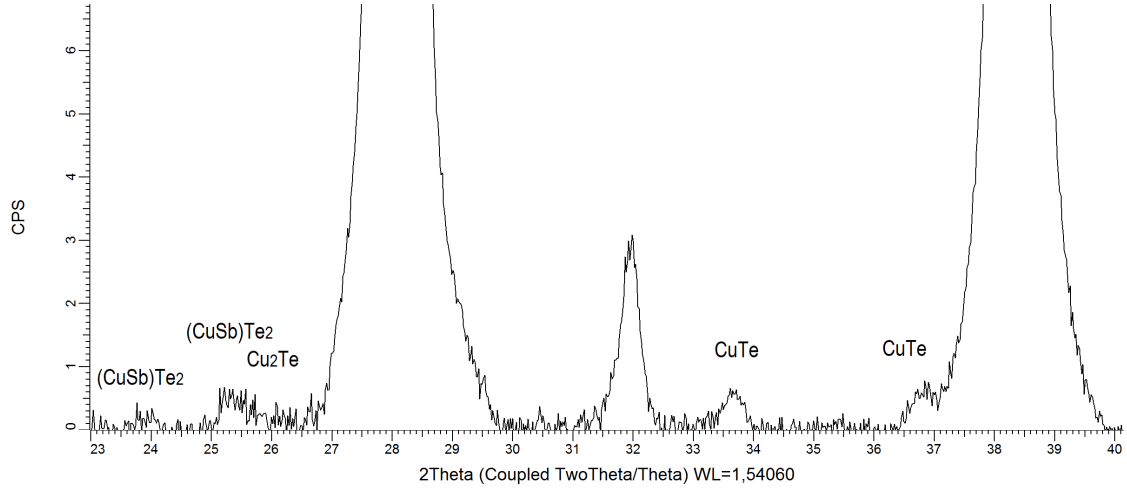

Fig. 1. Radiograph of the $PbSb_2Te_4$:Cu system

The reflexes of the copper-containing phases, despite their significantly lower intensity than those of the main phases $PbSb_2Te_4$ and Sb_2Te_3, are determined on the radiograph and interpreted using the ICDD PDF-2 powder database and the Rietveld method using Bruker TOPAS4 software. The sizes of the coherent scattering regions were determined using the Scherrer formula: Cu_2Te up to 120 nm, CuTe up to 95 nm and $(CuSb)Te_2$ up to 75 nm.

Since copper-containing phases are recorded on the X-ray at the trace level, measurements of the Raman spectra were performed to confirm the existence of additional copper-containing phases in the crystals.

The Raman spectra were measured using a LabRam HR800 spectrometer (Horiba) equipped with a confocal microscope. The use of a single monochromator in the spectrometer caused the introduction of an edge filter into the recording channel, cutting off the laser excitation line, which limits the possibility of measuring spectra in the region of less than 100 cm^{-1}. A continuous laser with a wavelength of 488 nm and a power of 100 mW was used as the source of exciting radiation. The laser radiation was focused on the sample surface using a 50x micro lens in an area of about 4 mm^2. Each spectrum was recorded with an accumulation of 30 seconds and averaged over 9 spectra. To measure the Raman spectra, fresh fragments were prepared along the planes of layered structures.

Raman spectra of two types were obtained (Fig. 2): in the cleavage plane and in the plane perpendicular to the cleavage plane (the end face). The two peaks at 121 cm^{-1} and 139 cm^{-1} are known as A^1 and E^2 vibrational modes of Te respectively (Lal et al. 2020). The peak at 161 cm^{-1} is closely related to the Sb_2Te_3 A^1 mode (Guo et al. 2016). The wide peak with a maximum of about 268 cm^{-1} which refers to the vibrational modes of the CuTe or Cu_2Te crystal phase (Park et al. 2011) is clearly visible, clearer on the spectrum taken from the end surface.

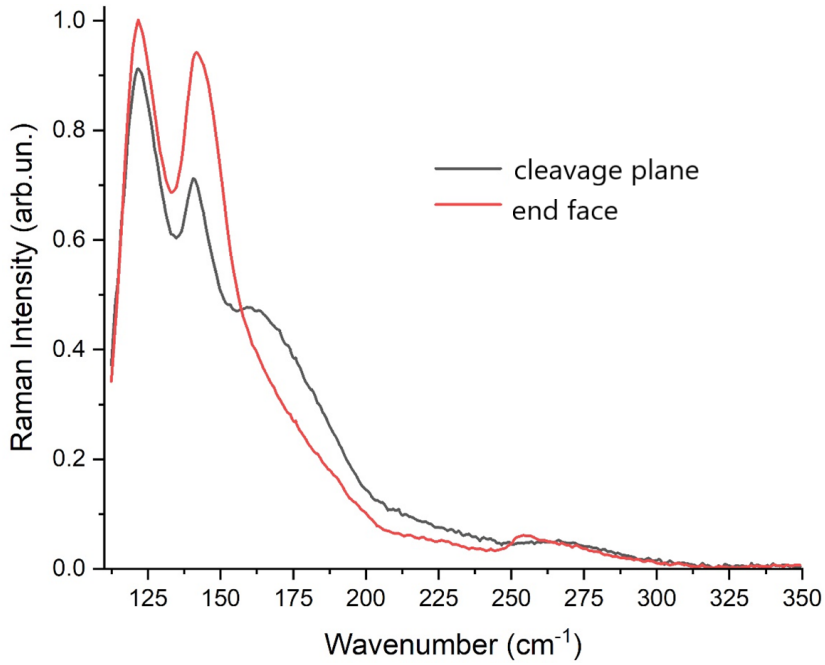

Fig. 2. $PbSb_2Te_4$:Cu crystals Raman spectra

The presence of a peak related to a copper-containing phase on the Raman spectra of the samples confirms that the studied crystals contain chemically bound copper atoms. Clearly expressed maximum when measuring the spectrum from the end surface confirms the assumption of localization of the phase with copper mainly in the van der Waals gap between the septuple and quintuple layers.

Conclusions

The mechanism of the copper doping of $PbSb_2Te_4$ crystals has been studied. X-ray diffraction analysis and Raman spectroscopy have shown that copper phases are present in doped crystals, the formation of which indicates the chemical bonding of copper atoms to Te atoms. With a relatively low copper content, there is a decrease in the concentration of holes, associated with filling vacancies in the metal sublattice. As the concentration of the alloying additive increases, copper atoms chemically bond

 https://www.doi.org/10.33910/2687-153X-2026-7-1-31-35

to Te atoms to form new phases, which does not lead to a decrease in carrier concentration. The assumed location of CuTe (Cu_2Te) phase in the van der Waals gaps between the septuple and quintuple layers is validated by the Raman spectra of the end surface of the $PbSb_2Te_4$:Cu crystalline samples.

We would also like to note that the complex multiphase composition of $PbSb_2Te_4$ crystals grown by the peritectic reaction by the Czochralski method and doped with copper, in our opinion, indicates that the melt is apparently structured and contains all the phases observed by us. The resulting crystals are a 'frozen melt.'

Conflict of Interest

The authors declare that there is no conflict of interest, either existing or potential.

Author Contributions

S. A. Nemov designed and directed the project; V. D. Andreeva performed the X-ray measurements and analysed the spectra; A. V. Povolotskiy performed the Raman spectra measurements, analysed the spectra and reviewed the overall text; A. Yu. Aliabev processed the experimental data, performed the analysis, drafted the manuscript and designed the figures. All the authors discussed the final work and took part in writing the article.

Acknowledgment

The Raman spectra were measured using the equipment of the Centre for Optical and Laser Materials Research — a resource centre of the St. Petersburg State University Research Park.

References

Bramfitt, B. L. (1970) The effect of carbide and nitride additions on the heterogeneous nucleation behavior of liquid iron. *Metalurgical Transactions*, 1, 1987–1995. https://doi.org/10.1007/BF02642799 (In English)

Goltsman, B. M., Kudinov, B. A., Smirnov, I. A. (1972) *Semiconductor Thermoelectric Materials Based on Bi2Te3*. Moscow: Nauka Publ., 320 p. (In English)

Guo, S., Xu, L., Zhang, J. et al. (2016) Enhanced Crystallization Behaviors of Silicon-Doped Sb2Te Films: Optical Evidences. *Scientific Reports*, 6 (1), article 33639. https://doi.org/10.1038/srep33639 (In English)

Ioffe, A. F. (1956) *Semiconductor Thermocells*. Moscow, Leningrad: USSR Academy of Sciences Publ., 104 p. (In Russian)

Jayan, K. D., Rakesh, P. (2022) First principles roadmap to topological insulators for quantum computing applications. In: *Recent Trends in Chemical and Material Sciences*, 8, pp. 136–148. https://doi.org/10.9734/bpi/rtcams-v8/2319B (In English)

Lal, S., Razeeb, K. M., Gautam, D. (2020) Enhanced Thermoelectric Properties of Electrodeposited Cu-Doped Te Films. *ACS Applied Energy Materials*, 3 (4), 3262–3268. https://doi.org/10.1021/acsaem.9b02153 (In English)

Menshchikova, T. V., Eremeev, S. V., Chulkov, E. V. (2013) Electronic structure of SnSb2Te4 and PbSb2Te4 topological insulators. *Applied Surface Science*, 267, 1–3. https://doi.org/10.1016/J.APSUSC.2012.04.048 (In English)

Nemov, S. A., Andreeva, V. D., Aliabev, A. Yu. (2025) Composition, structure and properties of PbSb2Te4 crystals grown by the Czochralski method. *Physics of Complex Systems*, 6 (3), 144–149. https://doi.org/10.33910/2687-153X-2025-6-3-144-149 (In English)

Nemov, S. A., Andreeva, V. D., Povolotskiy, A. V. et al. (2024) Study of the structure of composite materials based on PbSb2Te4 obtained by the Czochralski method. *Glass Physics and Chemistry*, 50 (5), 553–560. (In English)

Nemov, S. A., Blagih, N. M., Dema, N. S. et al. (2012) Effect of copper doping on kinetic coefficients and their anisotropy in PbSb2Te4. *Semiconductors*, 46 (4), 447–451. (In English)

Park, B. J., Seo, H. S., Ahn, J. T. et al. (2011) An investigation on photoluminescence and AC powder electroluminescence of ZnS:Cu,Cl,Mn,Te phosphor. *Journal of Materials Research*, 26, 2394–2399. https://doi.org/10.1557/jmr.2011.260 (In English)

Shelimova, L. E., Karpinski, O. G., Konstantinov, P. P. et al. (2006) Layered chalcogenides in quasi-binary AIVBVI — AV2BVI3 systems (AIV — Ge,Sn,Pb; BVI — Te, Se; AV — Bi,Sb) are promising thermoelectric materials for thermogenerators. *Perspective materials*, 4, 5–17. (In Russian)

Shelimova, L. E., Karpinski, O. G., Konstantinov, P. P. et al. (2008) Anisotropic thermoelectric materials for thermogenerators based on layers of tetrademite-like chalcogenides. *Perspective materials*, 2, 28–38. (In Russian)

Shelimova, L. E., Karpinskii, O. G., Svechnikova, T. E. et al. (2004) Synthesis and structure of layered compounds in the PbTe-Bi2Te3 and PbTe-Sb2Te3 systems. *Inorganic Materials*, 40 (5), 1264–1270. https://doi.org/10.1007/s10789-005-0069-1 (In English)

Theoretical physics.
Cosmic rays. Relativistic astrophysics.
Cosmology

UDC 524.83

EDN DMXJNM
https://www.doi.org/10.33910/2687-153X-2026-7-1-36-44

Potential for a transition from standard to phantom dark energy in the FLRW cosmology: A dynamical systems analysis

V. D. Vertogradov ✉[1,2,3], U. V. Yamaltdinova [2]

[1] Herzen State Pedagogical University of Russia, 48 Moika Emb., Saint Petersburg 191186, Russia
[2] Saint Peterburg Branch of Special Astrophysical Observatory of the Russian Academy of Sciences, 65 Pulkovskoe Highway, Saint Petersburg 196140, Russia
[3] Center for Theoretical Physics, Khazar University, 41 Mehseti Street, Baku AZ-1096, Azerbaijan

Authors

Vitaly D. Vertogradov, ORCID: 0000-0002-5096-7696, e-mail vdvertogradov@gmail.com

Ulyana V. Yamaltdinova, ORCID: 0009-0001-8451-0950, e-mail ulanav498@gmail.com

For citation: Vertogradov, V. D., Yamaltdinova, U. V. (2026) Potential for a transition from standard to phantom dark energy in the FLRW cosmology: A dynamical systems analysis. *Physics of Complex Systems*, 7 (1), 36–44. https://www.doi.org/10.33910/2687-153X-2026-7-1-36-44 EDN DMXJNM

Received 18 December 2025; reviewed 20 January 2026; accepted 20 January 2026.

Funding: The study did not receive any external funding.

Abstract. Modern cosmology is based on the ΛCDM model, in which the Universe's accelerated expansion is driven by dark energy with equation of state $w = -1$. While ΛCDM agrees well with observational data — from CMB anisotropies to large-scale structure — both theoretical considerations and emerging observations suggest that dark energy may be dynamical, with $w(z)$ that evolves over time. A scenario of particular interest is a potential transition from standard dark energy ($w \geq -1$) to phantom energy ($w < -1$), which violates the strong energy condition and may lead to a 'Big Rip'. Planck data (Aghanim et al. 2020) confirm that, as of today, dark energy dominates ($\Omega_{DE} \approx 0.685$) and w is consistent with -1; however, combined analyses (Planck + BAO + supernovae) permit slight deviations into the phantom regime ($w \approx -1.03 \pm 0.03$). Though marginal, this possibility motivates the study of models where $w(z)$ crosses the $w = -1$ barrier. Moreover, recent JWST observations reveal unexpectedly massive galaxies at $z > 10$, challenging ΛCDM predictions of structure formation and hinting at modified expansion histories that may involve evolving — or phantom — dark energy. This work investigates whether phantom energy can act as a future attractor in a flat FLRW cosmology. Using autonomous dynamical systems, we analyse the evolution of density parameters $\Omega_i(z)$ and $w(z)$ in a model that permits crossing the $w = -1$ divide.

Keywords: cosmology, dark energy, phantom energy, FLRW model, dynamical systems, equation of state

Einstein's field equations

In 1905, Albert Einstein formulated the special theory of relativity (STR), which unified space and time into a single four-dimensional spacetime and rejected Newton's concept of absolute space and time (Blau 2024). However, STR is restricted to inertial reference frames and does not incorporate gravity.

Seeking to include gravitation into the relativistic worldview, Einstein completed the general theory of relativity (GTR) in 1915 — a geometric theory in which gravitational interaction is interpreted not as a force, but as a manifestation of spacetime curvature induced by the distribution of energy and

momentum (Blau 2024). The foundation of the theory is given by Einstein's equations, which in their modern form read:

$$G_{\mu\nu} + \Lambda g_{\mu\nu} = \frac{8\pi G}{c^4} T_{\mu\nu}, \tag{1}$$

where $G_{\mu\nu} = R_{\mu\nu} - \frac{1}{2} R\, g_{\mu\nu}$ is the Einstein tensor, expressing spacetime curvature via the Ricci tensor $R_{\mu\nu}$ and Ricci scalar R; $g_{\mu\nu}$ is the metric tensor, defining intervals and angles; $T_{\mu\nu}$ is the energy–momentum tensor, describing the densities and fluxes of energy, momentum, and stresses; G is the gravitational constant, c is the speed of light, and Λ is the so-called *cosmological constant* (Adler et al.1995; Blau 2024).

A crucial feature of the left-hand side is that, owing to the Bianchi differential identity ($\nabla^\mu G_{\mu\nu} = 0$) and metric compatibility ($\nabla^\mu g_{\mu\nu} = 0$), Einstein's equations automatically imply the law of local energy–momentum conservation:

$$\nabla^\mu T_{\mu\nu} = 0. \tag{2}$$

This ensures that GTR remains consistent with fundamental physical principles, even within curved spacetime (Perko 2001).

As early as 1916, Karl Schwarzschild found the first exact vacuum solution ($T_{\mu\nu} = 0$) to Einstein's equations, describing spacetime around a spherically symmetric body — a result that later became the cornerstone for the theory of black holes (Blau 2024). However, as it turned out, local solutions were only a first step: to describe the Universe as a whole, a solution satisfying the new physical principle of large-scale homogeneity and isotropy was required (Coley 2003).

A significant difficulty then arose: the original field equations (with $\Lambda = 0$) admit no static, homogeneous, and isotropic solution — any such model is necessarily dynamical, either expanding or contracting. This conflicted with the early-20$^{\text{th}}$-century view of a static, eternal Universe (Weinberg 1989).

To resolve this inconsistency, Einstein in 1917 introduced the additional term $\Lambda g_{\mu\nu}$ into the field equations. Initially, Λ had no physical interpretation — it was a *geometric parameter* introduced *ad hoc* to allow for a static cosmological solution. In his paper 'Cosmological Considerations in the General Theory of Relativity', he showed that the condition

$$\Lambda = \frac{4\pi G\rho}{c^2}, \tag{3}$$

where ρ is the average mass density in a homogeneous Universe, yields a static model (later termed *Einstein's Universe* — a closed three-dimensional hypersphere of finite radius). Thus, Λ functioned as *gravitational repulsion*, precisely compensating the attraction of matter (Adler et al. 1995; Weinberg 1989).

Importantly, the term $\Lambda g_{\mu\nu}$ was mathematically permissible — it preserved general covariance and automatically satisfied $\nabla^\mu(\Lambda g_{\mu\nu}) = 0$, thereby not violating energy–momentum conservation (Blau 2024). However, in 1922–1929, A. A. Friedmann, G. Lemaître, and E. Hubble demonstrated the Universe's expansion, rendering the static model obsolete. Einstein soon abandoned Λ, calling it 'the greatest blunder' of his life.

Paradoxically, observations of the Universe's accelerated expansion from Type Ia supernovae data in 1998 revived Λ as central to modern cosmology (Dungan, Prosper 2011; Riess et al. 1998). It is now interpreted as the simplest model of *dark energy* — a homogeneous vacuum energy with an equation of state $p = -\rho c^2$ (Carroll 2001; Peebles, Ratra 2003; Weinberg 1989). Thus, the parameter introduced to salvage an outdated cosmological picture proved essential for describing the observed accelerated expansion. It is with this modern interpretation that Λ enters the subsequent stage: constructing a dynamical cosmological model.

The Friedmann metric

The expansion of the Universe, discovered by Hubble, necessitated a transition from static to dynamical cosmological models (Aghanim et al. 2020). Already in the 1920s, A. A. Friedmann, and independently G. Lemaître, H. Robertson, and A. Walker, showed that assuming the *cosmological principle* — homogeneity and isotropy of the Universe on scales $\gtrsim 100$ Mpc — uniquely determines spacetime geography via the Friedmann–Robertson–Walker (FRW) metric (Coley 2003).

Although the Universe is structured on small scales (galaxies, clusters, filaments, and voids), averaging over sufficiently large volumes allows its description as a smooth medium (Barreiro et al. 2000; Nunes, Mimoso 2000). Based on this, the most general spacetime metric consistent with the cosmological principle is:

$$ds^2 = -c^2dt^2 + a^2(t)[\frac{dr^2}{1-kr^2} + r^2(d\theta^2 + \sin^2\theta\, d\phi^2)], \quad (4)$$

where: ds^2 is the spacetime interval squared; t is *cosmic time*, measured by an observer comoving with the average matter flow; $a(t)$ is the *scale factor*, a dimensionless function of time that determines the relative change in distances between comoving points (e. g., unbound galaxies); (r, θ, ϕ) are comoving spherical coordinates ('attached' to the expanding medium); k is the dimensionless spatial curvature parameter, taking one of three values:

$$k = \begin{matrix} +1 & \text{— closed (spherical) space,} \\ 0 & \text{— flat (Euclidean) space,} \\ -1 & \text{— open (hyperbolic) space.} \end{matrix} \quad (5)$$

The scale factor $a(t)$ itself has no absolute physical meaning — it may be normalised arbitrarily (e. g., $a(t_0) = 1$ at the present epoch). Observable quantities depend only on its *derivatives*. Hence, the key dynamical characteristic in cosmology is the *Hubble parameter*:

$$H(t) = \frac{\dot{a}(t)}{a(t)}, \quad (6)$$

where the dot denotes differentiation with respect to cosmic time t. The quantity $H_0 = H(t_0)$ characterises the current expansion rate (Aghanim et al. 2020).

Consider the physical meaning of the three possible values of k:

- $k = +1$ (*closed Universe*). Spatial sections have positive curvature and the topology of a three-sphere S^3. The volume is finite and unbounded. If the total energy density ρ exceeds the *critical density*

$$\rho_{\text{cr}}(t) = \frac{3H^2(t)}{8\pi G}, \quad (7)$$

gravitational attraction will eventually halt expansion, and the Universe will recollapse into a singularity — the 'Big Crunch' (Coley 2003).

- $k = 0$ (*flat Universe*). Space is Euclidean ($\mathbb{R}^3$) and infinite. In the absence of dark energy, expansion continues forever but gradually decelerates. Modern CMB data (*Planck,* 2018) indicate a high degree of flatness:

$$\Omega_k \equiv -\frac{kc^2}{a^2H^2} = -0.011^{+0.010}_{-0.012}, \quad (8)$$

consistent with $k = 0$ at the 1% level (Aghanim et al. 2020).

- $k = -1$ (*open Universe*). Space has negative curvature (Lobachevskian geometry), is infinite, and geodesics diverge. This model occurs when $\rho < \rho_{\text{cr}}$, and expansion proceeds indefinitely. The sum of angles in a triangle is less than 180 °, and the volume of a sphere of radius R grows faster than R^3 (Coley 2003).

Thus, the FRW metric is not an arbitrary choice, but the *only* form compatible with the cosmological principle. It provides the geometric 'stage' on which cosmic dynamics unfolds. To 'activate' these dynamics — that is, to determine how exactly $a(t)$ evolves with time — one must substitute the FRW metric into Einstein's equations and specify the material content of the Universe. This step leads directly to the system of equations governing cosmological evolution.

 https://www.doi.org/10.33910/2687-153X-2026-7-1-36-44

Dynamics of cosmic expansion: From Einstein's equations to the evolution of the scale factor

Our primary objective is to determine the time evolution of the scale factor $a(t)$ — i. e., to describe the dynamics of cosmic expansion (or contraction). To this end, we begin with the fundamental equations of general relativity — Einstein's field equations in their general form:

$$G_{\mu\nu} + \Lambda\, g_{\mu\nu} = \frac{8\pi G}{c^4}\, T_{\mu\nu}. \tag{9}$$

Here: $G_{\mu\nu} = R_{\mu\nu} - \frac{1}{2} R\, g_{\mu\nu}$ is the Einstein tensor, expressing spacetime curvature; $g_{\mu\nu}$ is the metric tensor (in this context, the Friedmann metric); Λ is the cosmological constant, introduced to describe homogeneous vacuum energy; $T_{\mu\nu}$ is the energy–momentum tensor, describing the distribution and motion of matter and energy; G and c are fundamental constants (Blau 2024).

Since matter on cosmological scales can be modeled as a perfect fluid (dust, radiation, dark energy), we adopt

$$T_{\mu\nu} = (\rho + \frac{p}{c^2}) u_\mu u_\nu + p\, g_{\mu\nu}, \tag{10}$$

where $\rho(t)$ is the energy density, $p(t)$ is the pressure, and u^μ is the four-velocity of a comoving observer (Coley 2003).

Substituting the FRW metric and this form of $T_{\mu\nu}$ into Eq. (9) — a technically cumbersome but straightforward procedure — yields two independent differential equations for $a(t)$, known as the *Friedmann equations*:

$$\left(\frac{\dot{a}}{a}\right)^2 = \left(\frac{8\pi G}{3}\right)\rho - \left(k\frac{c^2}{a^2}\right) + \left(\Lambda\frac{c^2}{3}\right), \tag{11}$$

$$\frac{\ddot{a}}{a} = -\left(\frac{4\pi G}{3}\right)\left(\rho + \frac{3p}{c^2}\right) + \frac{\Lambda c^2}{3}. \tag{12}$$

The first equation (often called the *Hubble equation*) links the current expansion rate to the total energy content and geometry of the Universe. The second equation shows that acceleration is determined not only by density but also by pressure: when $\rho + 3p/c^2 < 0$, gravity becomes effectively repulsive — this is the precise mechanism driving the accelerated expansion observed today (Copeland et al. 2006; Feng et al. 2005).

However, the system (11)–(12) contains three time-dependent unknowns: $a(t)$, $\rho(t)$, and $p(t)$. To obtain a unique solution, the system must be closed by an additional relation.

This relation emerges naturally from the structure of Einstein's equations. As noted earlier, the left-hand side of (9) is identically conserved: $\nabla^\mu(G_{\mu\nu} + \Lambda g_{\mu\nu}) = 0$, and therefore Einstein's equations imply the local energy–momentum conservation law:

$$\nabla_\mu T^{\mu\nu} = 0. \tag{13}$$

For a perfect fluid in the FRW metric, Eq. (13) reduces to a single nontrivial scalar equation — the *continuity equation*:

$$\dot{\rho} + 3H(\rho + \frac{p}{c^2}) = 0, H = \frac{\dot{a}}{a}. \tag{14}$$

Physically, it expresses energy balance in an expanding volume: as the scale factor grows ($a \uparrow$), the volume increases as a^3, thereby decreasing density; the pressure p determines whether additional energy loss occurs (e. g., photons lose energy not only due to dilution but also due to cosmological redshift) (Coley 2003).

Despite the presence of Eq. (14), the system remains underdetermined: ρ and p are still independent. To resolve this, we introduce an *equation of state* — a physical relation derived from the microscopic nature of the matter:

$$p = w\,\rho c^2, \tag{15}$$

where w is a dimensionless parameter characteristic of the given component:

- $w = 0$ — non-relativistic matter ('dust'): $\rho \propto a^{-3}$;
- $w = \frac{1}{3}$ — radiation: $\rho \propto a^{-4}$;
- $w = -1$ — cosmological constant: ρ = const;
- $w < -1$ — phantom energy: ρ *increases* with expansion (Cai et al. 2010; Garcia-Salcedo et al. 2013).

Substituting (15) into (14) yields the explicit dependence:

$$\rho(a) = \rho_0\, a^{-3(1+w)}, \tag{16}$$

which, when inserted into the first Friedmann equation (11), transforms it into a closed differential equation for $a(t)$. Thus, from fundamental Einstein equations — through geometry (FRW), matter ($T_{\mu\nu}$), and microphysics (w) — we arrive at a complete description of cosmic evolution.

Dynamical systems method in cosmology

Consider a homogeneous and isotropic Universe described by the Friedmann–Robertson–Walker (FRW) metric with zero spatial curvature ($k = 0$). The first Friedmann equation then takes the form:

$$\left(\frac{\dot{a}}{a}\right)^2 = H^2 = \frac{1}{3}\rho, \tag{17}$$

where $a(t)$ is the scale factor, $H \equiv \dot{a}/a$ is the Hubble parameter, and ρ is the total energy density. We assume the Universe consists of four components:

- radiation (r),
- non-relativistic matter (m),
- standard dark energy (DE),
- phantom energy (ph).

Consequently,

$$\rho = \rho_r + \rho_m + \rho_{\mathrm{DE}} + \rho_{\mathrm{ph}}. \tag{18}$$

The evolution of each component is governed by the continuity equation, derived from energy–momentum conservation in the FRW metric:

$$\dot{\rho}_i + 3H(\rho_i + p_i) = 0, \tag{19}$$

where p_i is the pressure of the i-th component. Introducing the equation-of-state parameter $w_i \equiv p_i/\rho_i$, Eq. (19) becomes

$$\dot{\rho}_i = -3H(1 + w_i)\rho_i. \tag{20}$$

For convenience, we define

$$\gamma_i \equiv 1 + w_i, \tag{21}$$

so that

$$\dot{\rho}_i = -3H\gamma_i\rho_i. \tag{22}$$

 https://www.doi.org/10.33910/2687-153X-2026-7-1-36-44

The specific values of γ_i for the components under consideration are determined by their physical nature:

$$\gamma_r = \frac{4}{3}, \gamma_m = 1{,}0 \leq \gamma_{\mathrm{DE}} < \frac{2}{3}, \gamma_{\mathrm{ph}} < 0. \tag{23}$$

Direct integration of the system (17)–(22) is difficult, as $\rho_i(a)$ are governed by nonlinear differential equations. Therefore, for qualitative analysis, we employ the dynamical systems method. We introduce dimensionless density parameters

$$\Omega_i \equiv \frac{\rho_i}{3H^2}, i = r, m, \mathrm{DE}, \mathrm{ph}, \tag{24}$$

and substituting (18) into (17) yields the normalisation condition:

$$\Omega_r + \Omega_m + \Omega_{\mathrm{DE}} + \Omega_{\mathrm{ph}} = 1. \tag{25}$$

Thus, only three variables are independent. We choose as phase-space coordinates:

$$x \equiv \Omega_m, y \equiv \Omega_{\mathrm{DE}}, z \equiv \Omega_{\mathrm{ph}}, \tag{26}$$

from which it follows that

$$\Omega_r = 1 - x - y - z. \tag{27}$$

To obtain an autonomous system, we differentiate (26) with respect to the logarithm of the scale factor, $N = \ln a$ (noting that $d/dN = H^{-1}d/dt$). For example, for x:

$$\frac{dx}{dN} = \frac{1}{H}\frac{d}{dt}\left(\frac{\rho_m}{3H^2}\right) = \frac{1}{H}\left(\frac{\dot{\rho}_m}{3H^2} - \frac{2\rho_m\dot{H}}{3H^3}\right) = \frac{\dot{\rho}_m}{3H^3} - 2\frac{\rho_m\dot{H}}{3H^4}. \tag{28}$$

Substituting $\dot{\rho}_m = -3H\gamma_m\rho_m$ from (22) and expressing $\dot{H}$ via the second Friedmann equation:

$$\dot{H} = -\frac{1}{2}\sum_i (\rho_i + p_i) = -\frac{1}{2}\sum_i \gamma_i\rho_i, \tag{29}$$

and using $\rho_i = 3H^2\Omega_i$ and (27), we obtain:

$$\dot{H} = -\frac{3}{2}H^2[\gamma_r(1 - x - y - z) + \gamma_m x + \gamma_{\mathrm{DE}} y + \gamma_{\mathrm{ph}} z]. \tag{30}$$

Insertion of (22) and (30) into (28), together with $\gamma_m = 1$, $\gamma_r = 4/3$, yields after simplification:

$$\frac{dx}{dN} = x[1 - x + y(3\gamma_{\mathrm{DE}} - 4) + z(3\gamma_{\mathrm{ph}} - 4)]. \tag{31}$$

Analogously, the equations for y and z are:

$$\frac{dy}{dN} = y[4 - 3\gamma_{\mathrm{DE}} + x + y(3\gamma_{\mathrm{DE}} - 4) + z(3\gamma_{\mathrm{ph}} - 4)], \tag{32}$$

$$\frac{dz}{dN} = z[4 - 3\gamma_{\mathrm{ph}} + x + y(3\gamma_{\mathrm{DE}} - 4) + z(3\gamma_{\mathrm{ph}} - 4)]. \tag{33}$$

The system (31)–(33) is autonomous (right-hand sides depend only on x, y, z), allowing the application of dynamical systems theory (Boehmer, Chan 2014; Boehmer et al. 2012; Coley 2003; Perko 2001).

Critical points and the Jacobian matrix

Critical points are obtained from $\dot{x} = \dot{y} = \dot{z} = 0$. Nontrivial solutions yield four physically meaningful points:

$$\begin{aligned} \mathbf{P}_r &= (0,0,0) && \text{— radiation domination,} \\ \mathbf{P}_m &= (1,0,0) && \text{— matter domination,} \\ \mathbf{P}_{\mathrm{DE}} &= (0,1,0) && \text{— standard dark energy domination,} \\ \mathbf{P}_{\mathrm{ph}} &= (0,0,1) && \text{— phantom energy domination.} \end{aligned} \tag{34}$$

To analyse their stability, we compute the Jacobian matrix $J = (\partial f_i / \partial x_j)$, where $f_1 = dx/dN$, etc. Denoting for brevity $A = 3\gamma_{\mathrm{DE}} - 4$, $B = 3\gamma_{\mathrm{ph}} - 4$, $C = 4 - 3\gamma_{\mathrm{DE}}$, $D = 4 - 3\gamma_{\mathrm{ph}}$, we obtain:

$$J(x,y,z) = \begin{pmatrix} 1 - 2x + Ay + Bz & Ax & Bx \\ y & C + x + 2Ay + Bz & By \\ z & Az & D + x + Ay + 2Bz \end{pmatrix}. \tag{35}$$

Substituting the coordinates of each critical point:

1. Point $\mathbf{P}_r$ = (0, 0, 0)

$$J(\mathbf{P}_r) = \begin{pmatrix} 1 & 0 & 0 \\ 0 & 4 - 3\gamma_{\mathrm{DE}} & 0 \\ 0 & 0 & 4 - 3\gamma_{\mathrm{ph}} \end{pmatrix}. \tag{36}$$

Eigenvalues: $\lambda_1 = 1$, $\lambda_2 = 4 - 3\gamma_{\mathrm{DE}}$, $\lambda_3 = 4 - 3\gamma_{\mathrm{ph}}$.
For $0 \le \gamma_{\mathrm{DE}} < 2/3$ and $\gamma_{\mathrm{ph}} < 0$, all $\lambda_i > 0$.
Conclusion: $\mathbf{P}_r$ is an unstable source (repeller), corresponding to the initial state.

2. Point $\mathbf{P}_m$ = (1, 0, 0)

$$J(\mathbf{P}_m) = \begin{pmatrix} -1 & 3\gamma_{\mathrm{DE}} - 4 & 3\gamma_{\mathrm{ph}} - 4 \\ 0 & 5 - 3\gamma_{\mathrm{DE}} & 0 \\ 0 & 0 & 5 - 3\gamma_{\mathrm{ph}} \end{pmatrix}. \tag{37}$$

Eigenvalues: $\lambda_1 = -1$, $\lambda_2 = 3(1 - \gamma_{\mathrm{DE}})$, $\lambda_3 = 3(1 - \gamma_{\mathrm{ph}})$.
For $\gamma_{\mathrm{DE}} < 1$ and $\gamma_{\mathrm{ph}} < 0$, we have $\lambda_1 < 0$, $\lambda_2 > 0$, $\lambda_3 > 0$.
Conclusion: $\mathbf{P}_m$ is a saddle point, corresponding to an intermediate epoch.

3. Point $\mathbf{P}_{\mathrm{DE}}$ = (0, 1, 0)

$$J(\mathbf{P}_{\mathrm{DE}}) = \begin{pmatrix} 3(\gamma_{\mathrm{DE}} - 1) & 0 & 3\gamma_{\mathrm{ph}} - 4 \\ 1 & 0 & 0 \\ 0 & 0 & 3(\gamma_{\mathrm{DE}} - \gamma_{\mathrm{ph}}) \end{pmatrix}. \tag{38}$$

Eigenvalues: $\lambda_1 = 3(\gamma_{\mathrm{DE}} - 1) < 0$, $\lambda_2 = 3\gamma_{\mathrm{DE}} - 4 <$ since $(\gamma_{\mathrm{DE}} < 2/3)$, $\lambda_3 = 3(\gamma_{\mathrm{DE}} - \gamma_{\mathrm{ph}}) > 0$ as $(\gamma_{\mathrm{ph}} < 0 < \gamma_{\mathrm{DE}})$.
Conclusion: $\mathbf{P}_{\mathrm{DE}}$ is a saddle point.

4. Point $\mathbf{P}_{\mathrm{ph}}$ = (0, 0, 1)

$$J(\mathbf{P}_{\mathrm{ph}}) = \begin{pmatrix} 3(\gamma_{\mathrm{ph}} - 1) & 3\gamma_{\mathrm{DE}} - 4 & 0 \\ 0 & 3(\gamma_{\mathrm{ph}} - \gamma_{\mathrm{DE}}) & 0 \\ 1 & 3\gamma_{\mathrm{DE}} - 4 & 0 \end{pmatrix}. \tag{39}$$

Eigenvalues: $\lambda_1 = 3(\gamma_{\mathrm{ph}} - 1) < 0$, $\lambda_2 = 3(\gamma_{\mathrm{ph}} - \gamma_{\mathrm{DE}}) < 0$, $\lambda_3 = 3\gamma_{\mathrm{ph}} - 4 < 0$, for all admissible $\gamma_{\mathrm{ph}} < 0$, $\gamma_{\mathrm{DE}} > 0$.
$\mathbf{P}_{\mathrm{ph}}$ is a **stable node** — a future attractor (Garcia-Salcedo et al. 2013).

 https://www.doi.org/10.33910/2687-153X-2026-7-1-36-44

Phase portrait description

This phase diagram (Fig. 1) illustrates the dynamical evolution of the Universe in the y-z plane, where $y = \Omega_{DE}$ (the density parameter of standard dark energy) and $z = \Omega_{ph}$ (the density parameter of phantom energy), under the constraint $x + y + z = 1$ (with $x = \Omega_m$ fixed or negligible).

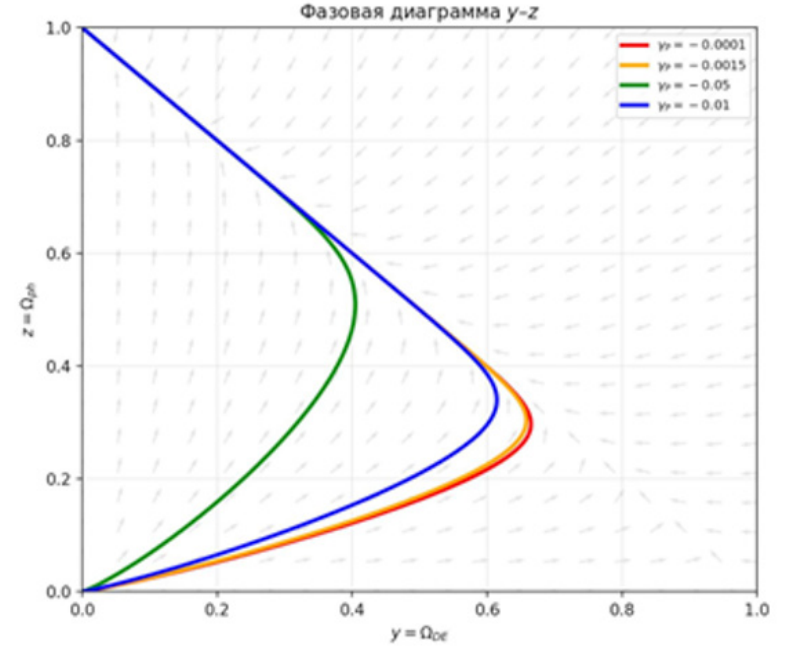

Fig. 1. Phase portrait

The trajectories (colored curves) represent cosmic evolution for different values of the phantom equation-of-state parameter $\gamma_{ph} = 1 + w_{ph}$. All trajectories originate near the origin ($y = 0, z = 0$) — corresponding to matter/radiation domination — and converge toward the point ($y = 0$, $z = 1$), which is the **phantom attractor** (Garcia-Salcedo et al. 2013).

The vector field (gray arrows) confirms that the phantom-dominated state is globally stable: all flows are directed toward the upper-left corner. The shape of the trajectories shows that as γ_{ph} becomes more negative (i. e., phantom energy becomes 'stronger'), the transition from standard dark energy to phantom dominance occurs earlier and more rapidly.

This visualization supports the key result: **phantom energy acts as a future attractor**, regardless of its initial abundance or the specific value of $w_{ph} < -1$ (Ashmita et al. 2024; Cai, Saridakis 2009).

Conclusions

The results indicate the following sequence of cosmological epochs:

1. evolution begins near P_r (radiation domination),
2. passes through the saddle point P_m (matter era, structure formation) (Nunes, Mimoso 2000),
3. then through P_{DE} (standard dark energy era) (Copeland et al. 2006),
4. and inevitably approaches P_{ph} (phantom energy domination) (Garcia-Salcedo et al. 2013).

Phantom energy domination ($w_{ph} < -1$) implies monotonic growth of its density, with $\rho_{ph} \propto a^{-3(1+w_{ph})}$ (where the exponent is positive), leading to a divergence of the scale factor, density, and curvature in finite cosmic time — the 'Big Rip' scenario (Copeland et al. 2006).

Thus, within the considered non-interacting four-component model, phantom energy is a globally stable future attractor. This is rigorously proven: all eigenvalues of the Jacobian at P_{ph} are negative for physically admissible $\gamma_{ph} < 0$ (Garcia-Salcedo et al. 2013). Although the model is primarily pedagogical (due to the absence of interactions and potential tensions with H_0 and S_8 measurements), it demonstrates the fundamental possibility of realising the phantom phase as the natural endpoint of cosmological evolution (Ashmita et al. 2024; Nojiri et al. 2017).

Conflict of Interest

The authors declare that there is no conflict of interest, either existing or potential.

Author Contributions

Vitaly D. Vertogradov supervised the project and provided guidance at all its stages; formulated the physical problem, developed the stability analysis methodology, interpreted the cosmological implications, and revised the manuscript.

Ulyana V. Yamaltdinova performed analytical and numerical calculations, constructed the phase-space portrait, and prepared figures and diagrams.

References

Adler, R. J., Casey, B. and Jacob, O. C. (1995) Vacuum Catastrophe: An Elementary Exposition of the Cosmological Constant problem. *American Journal of Physics*, 63, 620-626. https://doi.org/10.1119/1.17850 (In English)

Aghanim, N., Akrami, Y., Ashdownet, M. et al. (2020) Planck 2018 results. VI. Cosmological parameters. *Astronomy & Astrophysics*, 641, A6. https://doi.org/10.1051/0004-6361/201833910 (In English)

Ashmita, R., Kinjal, B., Prasanta, K. D. (2024) Constructing viable interacting dark matter and dark energy models: a dynamical systems approach. *Journal of Cosmology and Astroparticle Physics*, 2024 (034), 1–36. https://doi.org/10.1088/1475-7516/2024/11/034 (In English)

Barreiro, T., Copeland, E. J., Nunes, N. J. (2000) Quintessence model with a non-minimal coupling to dark matter. *Physical Review D*, 61, 12, article 127301. (In English)

Blau, M. (2024) *Lecture notes on General Relativity*. Bern: Albert Einstein Center for Fundamental Physics Publ., 990 p. (In English)

Boehmer, C. G., Chan, N. (2017) Dynamical Systems in Cosmology. In: *Dynamical and Complex Systems*. Singapore: World Scientific Publ., pp. 121–156. https://doi.org/10.1142/9781786341044_0004 (In English)

Boehmer, C. G., Chan, N., Lazkoz, R. (2012) Dynamics of dark energy models and centre manifolds. *Physics Letters B*, 714 (1), 11–17. https://doi.org/10.1016/j.physletb.2012.06.064 (In English)

Cai, Y.-F., Saridakis, E. N. (2009) A model of vacuum energy transition: slow-roll to quintessence. *Physics Letters B*, 672 (3), 389–393. https://doi.org/10.1016/j.physletb.2009.01.044 (In English)

Cai, Y.-F., Saridakis, E. N., Setare, M. R., Xia, J.-Q. (2010) Quintom cosmology: Theoretical implications and observations. *Physics Reports*, 493 (1), 1– 60. https://doi.org/10.1016/j.physrep.2010.04.001 (In English)

Carroll, S. M. (2001) The cosmological constant. *Living Reviews in Relativity*, 4, article 1. (In English)

Coley, A. A. (2003) *Dynamical Systems and Cosmology*. Dordrecht: Springer, 264 p. (In English)

Copeland, E. J., Sami, M., Tsujikawa, S. (2006) Dynamics of dark energy. *International Journal of Modern Physics D*, 15 (11), 1753–1936. https://doi.org/10.1142/S021827180600942X (In English)

Dungan, R., Prosper, H. B. (2011) Cosmological parameter estimation using supernova data. *American Journal of Physics*, 79 (1), 57–62. https://doi.org/10.48550/arXiv.0909.5416 (In English)

Feng, B., Wang, X., Zhang, X. (2005) Dark energy constraints from the cosmic age and supernova. *Physics Letters B*, 607 (1–2), 35–41. https://doi.org/10.1016/j.physletb.2004.12.071 (In English)

Garcia-Salcedo, R., Gonzalez, T., Quiros, I., Thompson-Montero, M. (2013) Phantom dark energy as the driver of the universe's cosmic history. *Physical Review D*, 88 (4), article 043008. https://doi.org/10.1103/PhysRevD.88.043008 (In English)

Nojiri, S., Odintsov, S. D., Oikonomou, V. K. (2017) Modified gravity theories on a nutshell: Inflation, bounce and late-time evolution. *Physics Reports*, 692, 1–104. https://doi.org/10.1016/j.physrep.2017.06.001 (In English)

Nunes, A., Mimoso, J. P. (2000) Cosmological scaling solutions and multiple dark matter species. *Physics Letters B*, 488 (5–6), 423–427. (In English)

Peebles, P. J. E., Ratra, B. (2003) The cosmological constant and dark energy. *Reviews of Modern Physics*, 75 (2), 559–606. http://dx.doi.org/10.1103/RevModPhys.75.559 (In English)

Perko, L. (2001) *Differential Equations and Dynamical Systems*. New York: Springer, 553 p. (In English)

Riess, A. G., Filippenko, A. V., Challis, P. et al. (1998) Observational evidence from supernovae for an accelerating universe and a Cosmological Constant. *Astronomical Journal*, 116 (3), 1009–1038. https://doi.org/10.1086/300499 (In English)

Weinberg, S. (1989) The cosmological constant problem. *Reviews of Modern Physics*, 61 (1), 1–23. (In English)

Theoretical physics.
Optics of condensed matter

UDC 535.3

EDN DQWTCV
https://www.doi.org/10.33910/2687-153X-2026-7-1-45-53

Interaction of ultrashort light pulses with an ensemble of quantum V-emitters

D. Ya. Bayramdurdiyev [1], R. F. Malikov ✉[1]

[1] Bashkir State Pedagogical University Named After M. Akmulla,
3A Oktyabrskoy Revolutsii Str., Ufa 450008, Russia

Authors

Davut Ya. Bayramdurdiyev, e-mail: d.bayramdurdiyev@gmail.com

Ramil F. Malikov, ORCID: 0000-0003-3457-0135, e-mail: rfmalikov@mail.ru

For citation: Bayramdurdiyev, D. Ya., Malikov, R. F. (2026) Interaction of ultrashort light pulses with an ensemble of quantum V-emitters. *Physics of Complex Systems*, 7 (1), 45–53. https://www.doi.org/10.33910/2687-153X-2026-7-1-45-53
EDN DQWTCV

Received 10 November 2025; reviewed 14 January 2026; accepted 15 January 2026.

Funding: The study did not receive any external funding.

Abstract. The paper reports the results of a theoretical study of the optical response of a two-dimensional supercrystal composed of quantum emitters with a doublet excited state (V-emitters) to a monochromatic external Gaussian pulse. The response dynamics are studied as a function of the input field's pulse area. It is shown that the field pulses interacting with the supercrystal lead to the generation of single, double, triple, and arc pulses with durations ten times shorter than those of the exciting pulses. The generation of single ultrashort pulses is shown to be independent of the magnitude of population excitation and can be realized in the presence of phase relaxation. The properties and effects of the optical response considered in this system suggest it may prove promising for applications in nanophotonics and quantum technologies.

Keywords: 2D superlattice, supercrystal, metasurface, three-level quantum emitters, quantum dots, self-oscillations, V-circuit, interaction of light pulses with 2D crystals, generation of optical pulses, phase relaxation

Introduction

Active research into metamaterials began following the discovery of graphene (Castro Neto et al. 2009; Novoselov et al. 2004). In recent decades, numerous reviews have been written on metamaterials and their applications in quantum photonics (Baimuratov et al. 2013; Bekenstein et al. 2020; Boneschanscher et al. 2014; Ding, Bozhevolnyi 2023; Solntsev et al. 2021; Soukoulis, Wegener 2010; Zheludev 2010). Ensembles of two- and three-level quantum systems represent the most widely used models for the theory of resonant laser-matter interactions. Within such models, foundational results have been obtained concerning various phenomena, such as photon echo (Kopvillem, Nagibarov 1963; Kurnit et al. 1964), self-induced transparency (McCall, Hahn 1967), electromagnetically induced transparency (Marangos 1998; Kasapi et al. 1995; Bloch 1946), optical nutation (Abragam 1963; Brewer, Shoemaker 1971), superradiance (Bonifacio et al. 1971; Bonifacio, Lugiato 1975a; 1975b; Dicke 1954; Trifonov et al. 1979), and the coherent amplification of light pulses (Basov, Letokhov 1965; Frantz, Nodvik 1963; Hopf, Scully 1969; Kryukov, Letokhov 1970; Icsevgi, Lamb 1969; Varnavskii et al 1984), etc.

The discovery of new materials in the form of metasurfaces with lattices of regular quantum emitters (superlattices or supercrystals) has prompted intensive study of the optical response properties of supercrystals for two- and three-level electronic transition schemes (Basharov 1988; Vlasov et al 2013; Malikov, Malyshev 2017; 2025; Ryzhov et al 2019; 2021; Bayramdurdiyev et al. 2020; Timoshchenko 2023).

In this paper, we investigate the nonlinear optical response of a supercritical structure consisting of ordered quantum emitters (quantum dots) with an excited-state doublet to an external field pulse. A pertinent example is semiconductor quantum dots with a degenerate valence band in a magnetic field (Efros et al. 1996). The high density and oscillator strength, along with the dipole-dipole interaction of the quantum emitters, play a significant role in the optical response of the supercrystal. Since the average dipole moment is directly dependent on the instantaneous quantum state, their interrelation is state-dependent. This relationship, combined with the intrinsic nonlinearity of the quantum emitter, provides positive feedback leading to highly stable dynamics, as observed in single layers of quantum emitters with ladder (Ryzhov et al. 2019) and lambda (Ryzhov et al. 2021) configurations. These systems exhibit monolayer responses characterized by self-oscillations, dynamic chaos, and high reflectivity within their operational frequency bands (Bayramdurdiyev et al. 2020; Ryzhov et al. 2019; 2021).

Model

The energy level and transition scheme for isolated, identical V-type quantum emitters is shown in Fig. 1. It is assumed that a plane wave with a frequency quasi-resonant to the optical transitions of V-quantum emitters falls on the monolayer. Here, |1> is the ground state with energy ε_1, |2> and |3> are the doublet states with energies ε_2 and ε_3, respectively. Optically resolved transitions are |1> and |2>, |1> and |3>, characterized by transition dipole moments d_{21} and d_{31}. The excited states |2> and |3> spontaneously decay into the ground state |1> with decay constants γ_{21} and γ_{31}, respectively. Non-radiative relaxation within the doublet is accounted for by the constant γ_{32}.

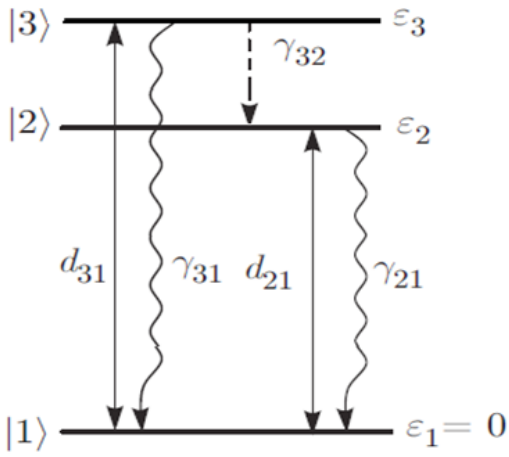

Fig. 1. Energy level diagram of a V-type quantum emitter

Basic equations

The optical dynamics of the quantum V-emitters within the supercrystal is described by the following system of equations for the density matrix (Bayramdurdiyev et al. 2020):

$$\dot{\rho}_{33} = -(\rho_{31}\Omega^* + \rho^*{}_{31}\Omega) - (\gamma_{31} + \gamma_{32})\rho_{33}\,, \tag{1a}$$

$$\dot{\rho}_{22} = -\mu(\rho^*{}_{21}\Omega + \rho_{21}\Omega^*) - (\gamma_{21} + \gamma_{32})\rho_{33}\,, \tag{1b}$$

$$\dot{\rho}_{11} = \rho^*{}_{31}\Omega + \rho_{31}\Omega^* + \mu * (\rho^*{}_{21}\Omega + \rho_{21}\Omega^*) + \gamma_{31}\rho_{33} + \gamma_{21}\rho_{22}\,, \tag{1c}$$

 https://www.doi.org/10.33910/2687-153X-2026-7-1-45-53

$$\dot{\rho}_{32} = -i\Delta_{32}\rho_{32} - \Omega\rho^*_{21} - \mu\rho_{31}\Omega^* - 0.5(\gamma_{31} + \gamma_{21} + \gamma_{32})\rho_{32} - 2\Gamma\cdot\rho_{32}\,, \tag{1d}$$

$$\dot{\rho}_{31} = -i\Delta_{31}\rho_{31} + \Omega Z_{31} + \mu\Omega\rho_{32} - 0.5(\gamma_{31} + \gamma_{32})\rho_{31} - \Gamma\cdot\rho_{31}, \tag{1e}$$

$$\dot{\rho}_{21} = -i\Delta_{21}\rho_{21} + \mu\Omega Z_{21} + \Omega\rho^*_{32} - 0.5\gamma_{21}\rho_{21} - \Gamma\cdot\rho_{21}\,, \tag{1f}$$

where the dot above ρ_{ij} denotes the time derivative, Δ_{32} is the doublet splitting, $\Delta_{31}=\omega_0-\omega_3$ and $\Delta_{32}=\omega_0-\omega_2$ are the detuning frequencies of the external field ω_0 from the resonant frequencies of the transitions 3↔1 and 3↔2, respectively; $\mu=(\gamma_{21}/\gamma_{31})^{1/2}$, and Γ is the parameter corresponding to for the dephasing of the energy states. The diagonal elements of the density matrix ρ_{33}, ρ_{22}, ρ_{11} represent level populations, while the off-diagonal elements ρ_{31} and ρ_{21} correspond to the radiative transitions of the emitter, and ρ_{32} describes the coherence between the quantum radiative transitions. The radiation field is described by the Rabi amplitude Ω of the active field, which is the sum of the external field Ω_0 and the field radiated by all other quantum emitters at the location of a given emitter (the second term):

$$\Omega = \Omega_0 + (\gamma_R - i\Delta_L)(\rho_{31} + \mu\rho_{21})\,, \tag{2}$$

Here, γ_R and Δ_L are the amplitudes of the secondary field in the far and near zones, respectively. The first term determines the collective dynamic broadening, while the second determines the dynamic shifts of the quantum emitter energy levels, both of which depend on the population differences.

An optical oscillation generator

Figure 2 presents stationary solutions of equations (1)–(2). The left panel shows the dependence of the absolute Rabi amplitude $|\Omega|$ within the monolayer on the Rabi amplitude $|\Omega_0|$ of the external field. The right panel shows the dependence of the senior Lyapunov exponent of the solution on $|\Omega|$. In Figure 2 (b, c), for the case of monolayer excitation at the center of the V-quantum emitter's doublet splitting ($\Delta_{31}=\Delta_{32}/2$, $\Delta_{32}=40$, $\Delta_{21}=-20$), the dependence of $|\Omega|$ on $|\Omega_0|$ is unambiguous within a certain range of $|\Omega_0|$. However, for other considered values of the doublet splitting, the dependence of $|\Omega|$ on $|\Omega_0|$ is ambiguous, indicating multistability in the monolayer response of an isolated V-quantum emitter.

Let us consider the interaction of light pulses with the supercrystal when the quantum emitter system is in its ground state ($\rho_{33}=0$, $\rho_{22}=0$, $\rho_{11}=1$). Excitation of the electronic system by an external field can be carried out on the second, third or at the center of the doublet splitting. In this study, we consider the case where the supercrystal's electronic system is excited at the center of the doublet ($\Delta_{31}=\Delta_{32}/2$), corresponding to the stationary solution shown in Fig. 2 (b, c).

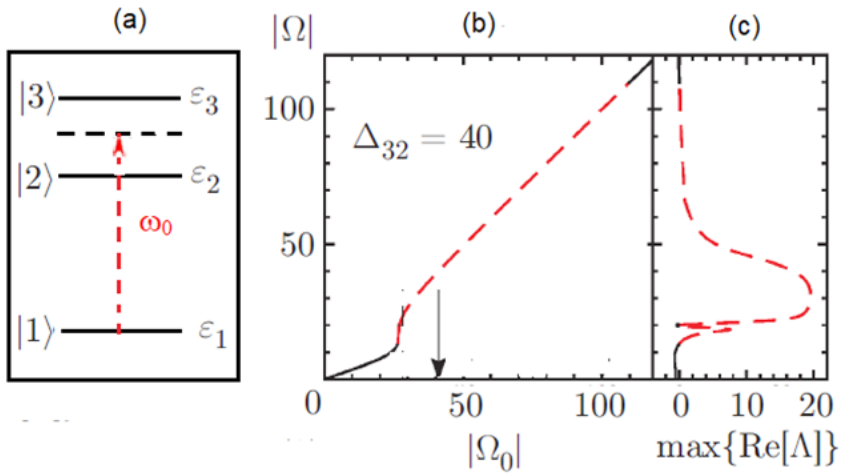

Fig. 2. Stationary solutions of equations (1)–(2)

We perform calculations for supercrystal parameters when the doublet width of the energy system is $\Delta_{32} = 40$. As follows from the stationary solutions, instabilities in the dynamic mode lead to the generation of oscillatory radiation, which eventually settles into the attractor (Fig. 3). The oscillatory optical response mode is realized at input field values in the range $|\Omega_0| = 26–100$.

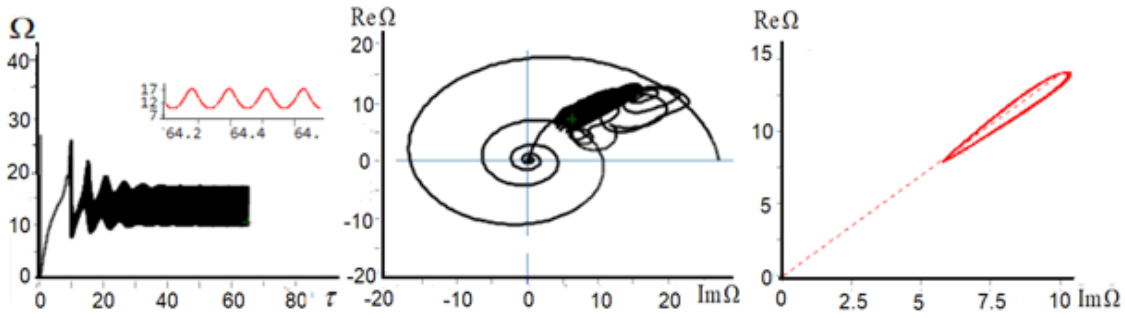

Fig. 3. Optical dynamics of a monolayer during the interaction of a field pulse with a supercrystal at the center of the doublet of V-quantum emitters ($\Delta_{31} = \Delta_{32}/2$). The field pulse magnitude is constant $Re\ \Omega_0 = 26$, $Im\Omega_0 = 0$. $g_{32} = 0.01$, $\Delta_{32} = 40$, $\Delta_{21} = -20$, $\Delta_L = 1000$, $\gamma_R = 100$

Figure 3 shows the dynamics of the field response and the corresponding phase portrait, illustrating an optical field generator. The system evolves into a periodic mode in the attractor (see inset); other modes of optical field generators can be found in (Malikov, Malyshev 2025). The first graph in Fig. 3 shows the response field dynamics $|\Omega(t)|$, the second shows the phase portrait of the dynamical system on the plane (Re[Ω], Im[Ω]), and the third shows the phase portrait of the attractor, which is a limit cycle. All quantities with dimensions of frequency are given in units of γ_{31}, time is given in units of γ^{-1}_{31}.

Interaction of a short field pulse with a monolayer

Let us consider the interaction of short light pulses with a supercrystal when the quantum emitter system is in the ground state ($\rho_{33} = 0$, $\rho_{22} = 0$, $\rho_{11} = 1$), and the emitters are excited at the center of the doublet ($\Delta_{31} = \Delta_{32}/2$, $\Delta_{32} = 40$, $\Delta_{21} = -20$). The field pulse interacting with the supercrystal is defined as a Gaussian function with a temporal width τ_p.

Here, τ_0 is the time of the pulse maximum. The integral of this function is equal to the pulse area θ_0, which in the coherent interactions is measured in units of π and is given by $\theta_0 = \int \mathrm{Re}\Omega_0(\tau)d\Omega = \Omega_1\pi$. Figure 4 shows numerical solutions for different values of the pulse area interacting with the supercrystal, with a pulse width of $\tau_p = 1$.

In all subsequent figures, the first graph shows the input field pulse $|\Omega_0(t)|$ and the supercrystal response $|\Omega(t)|$; the second shows the dynamics of energy level populations; and the third shows the phase portrait on the plane (Re[Ω], Im[Ω]). All quantities with dimensions of frequency are given in units of γ_{31}, time is given in units of γ^{-1}_{31}.

As a result of numerical experiments, we found that when excited by a Gaussian pulse, the monolayer generates an optical response in the form of single, binary, ternary, etc. pulses. The optical response of the supercrystal in these modes becomes evident at pulse area values of $\theta_0 = 40\pi$. Moreover, the duration of the generated field pulses is ten times less than that of the exciting pulse. Studies with different doublet splitting values Δ_{32} have shown that stable generation of single, double, and triple pulses is observed even at lower values of the unput pulse area and duration.

The simulation results indicate that the duration of the generated pulses depends on the magnitude of the doublet splitting. Smaller splitting leads to shorter generated pulse durations. Within the duration of the exciting pulse, one, two, three, etc. pulses are generated, corresponding to periods of the optical generator. We cut out the corresponding oscillations from the optical pulse generator (Fig. 3) using an external field pulse of finite duration (3). As follows from the calculations, the optical response of the supercrystal takes the form of either a single pulse or a pulse cluster.

The generation of single pulses does not depend on the population state (ground or excited) of the overall system (see Fig. 5)

 https://www.doi.org/10.33910/2687-153X-2026-7-1-45-53

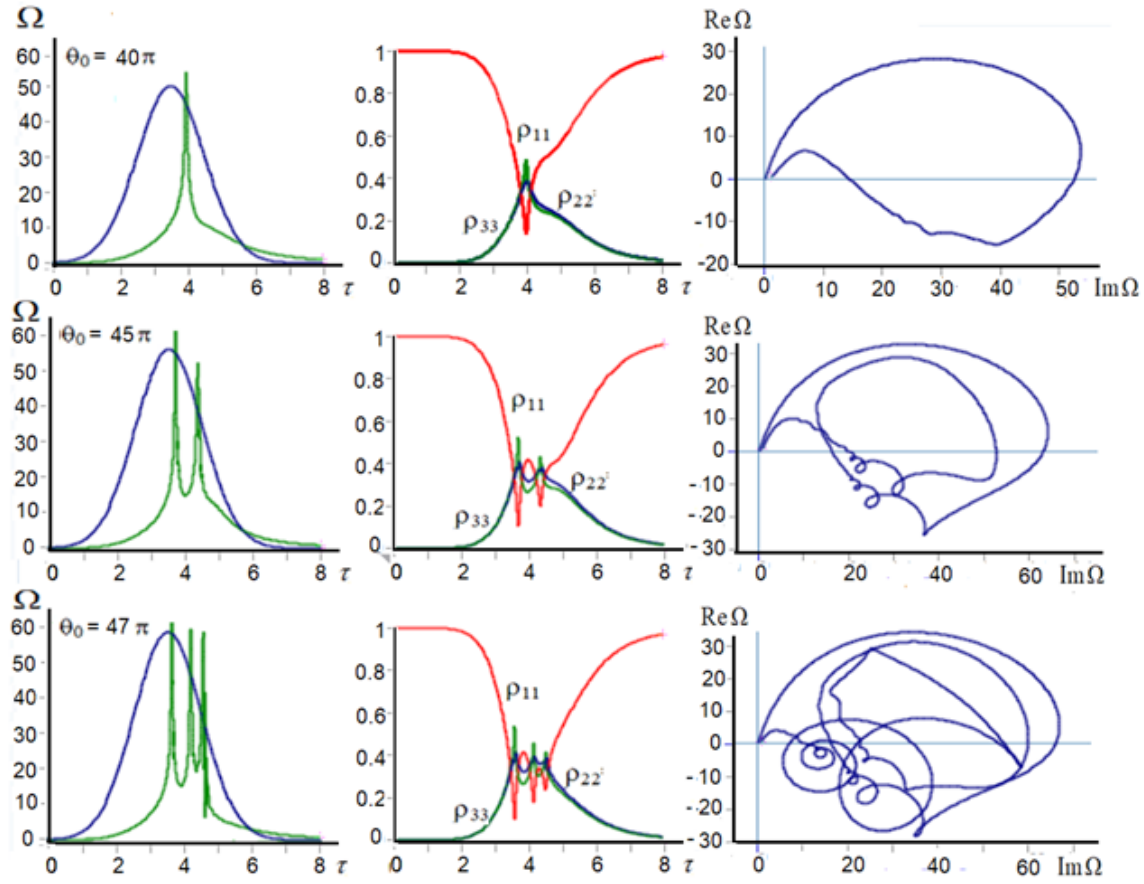

Fig. 4. Optical dynamics of a monolayer during the interaction of a field pulse of different areas with a supercrystal, with system excitation at the center of the V-quantum emitters ($\Delta_{31} = \Delta_{32}/2$), $\Delta_{32} = 40$, $\Delta_{21} = -20$ in the absence of phase relaxation $g2 = 0, \tau p = 1$, $\Delta_L = 1000$, $\gamma_R = 100$

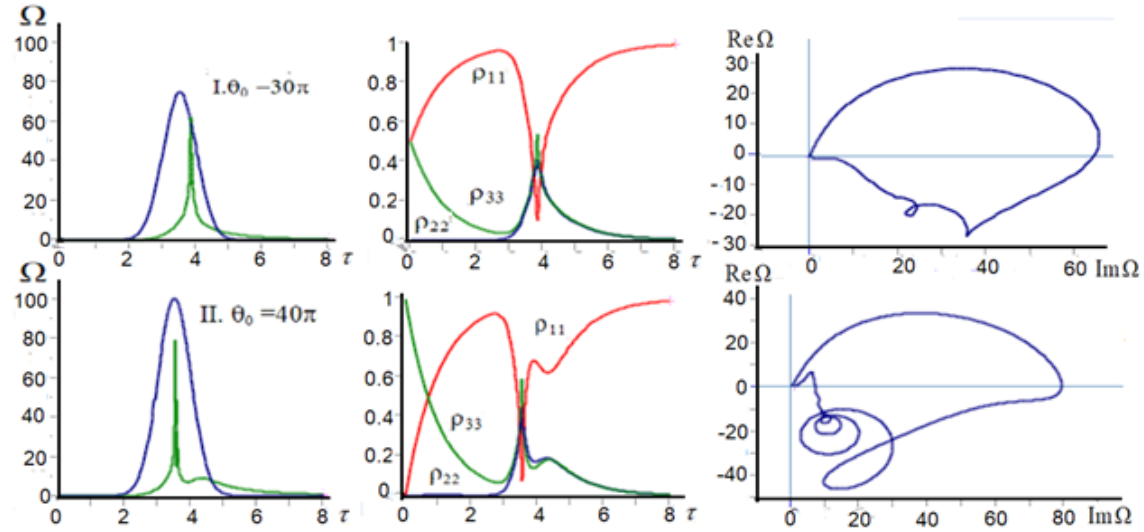

Fig. 5. Optical dynamics of a monolayer during the interaction of a field pulse with a supercrystal, with system excitation at the center of the doublet of V-emitters ($\Delta_{31}=\Delta_{32}/2$) in the absence of phase relaxation $g_2 = 0$, $\Delta_{32} = 40$, $\Delta_{21} = -20$. $\tau_p = 0.4$, $\Delta_L = 1000$, $\gamma_R = 100$ and different initial conditions *I.* $\rho_{33} = 0.5$, $\rho_{22} = 0.0$, $\rho_{11} = 0.5$. *II.* $\rho_{33} = 1.0$, $\rho_{22} = 0.0$, $\rho_{11} = 0.0$

The effect of phase relaxation on pulse generation

The influence of phase relaxation was studied for the three cases shown in Fig. 4. Figure 6 below presents numerical calculations of the effect of a short pulse on a supercrystal with phase relaxation g_2 = 1 and 1.2.

As the calculations show, phase relaxation affects the peak intensity and ultimately suppresses the single pulse generation.

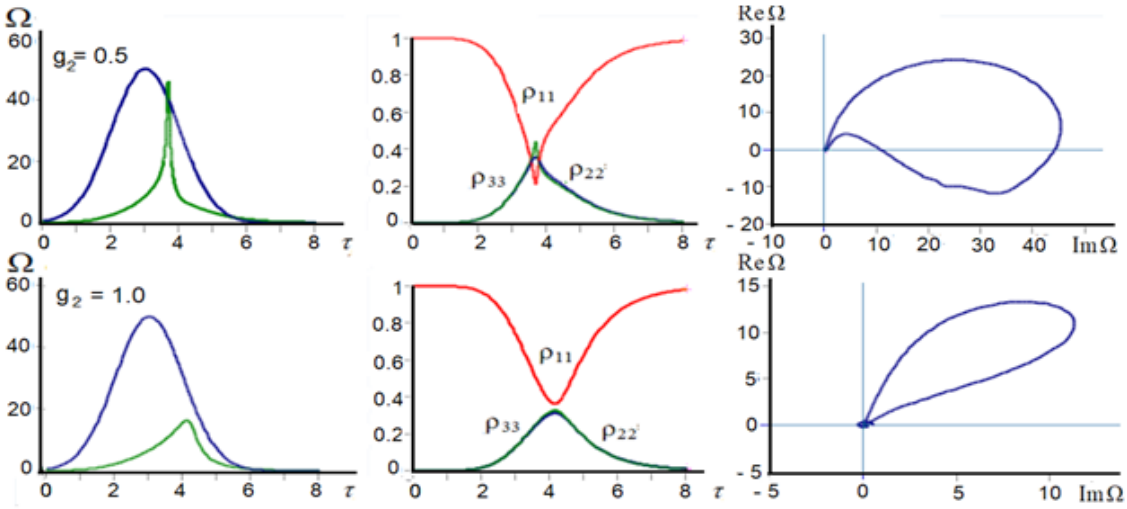

Fig. 6. Effect of phase relaxation on pulse generation by a supercrystal. The field pulse area is $\theta_0 = 40\pi$, with a duration of $\tau_p = 1$. The supercrystal parameters are $\Delta_{31} = \Delta_{32}/2$, $\Delta_{32} = 40$, $\Delta_{21} = -20$, $\Delta_L = 1000$, $\gamma_R = 100$

For the second case, where a binary pulse is observed, an increase in the magnitude of phase relaxation leads to the suppression and disappearance of the second pulse, i. e., the binary pulse is converted into a single pulse (see Fig. 7).

For the third case, shown in Fig. 4, an increase in phase relaxation initially leads to the formation of a pulse train, then to the fusion of these pulses, resulting in a shortened pulse with a significantly steeper leading edge compared to the incident Gaussian field pulse (Fig. 8).

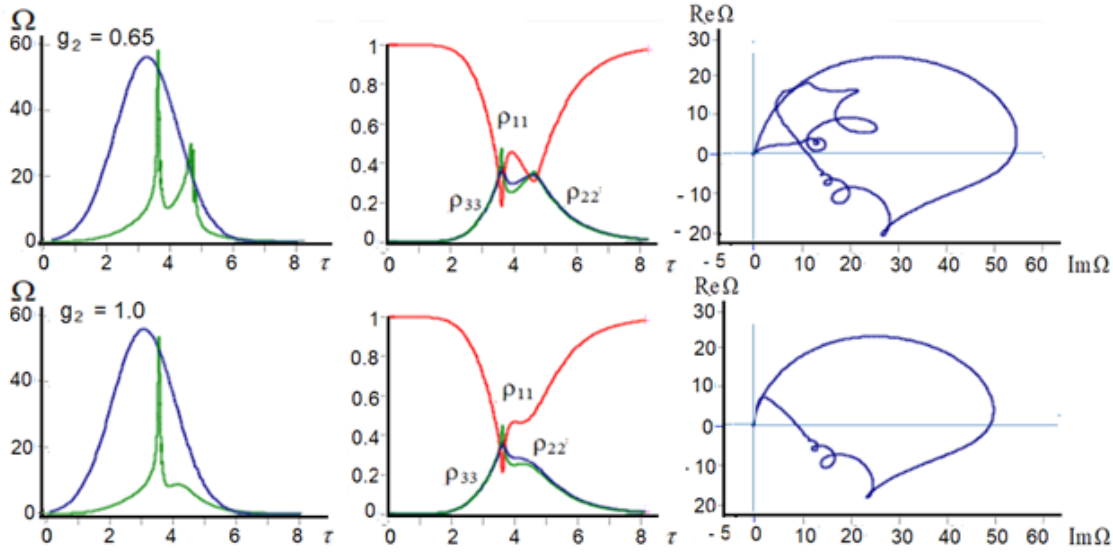

Fig. 7. Effect of phase relaxation on pulse generation by a supercrystal. The field pulse area is $\theta_0 = 50\pi$, with a duration of $\tau_p = 1$. The supercrystal parameters are $\Delta_{31} = \Delta_{32}/2$, $\Delta_{32} = 40$, $\Delta_{21} = -20$, $\Delta_L = 1000$, $\gamma_R = 100$

https://www.doi.org/10.33910/2687-153X-2026-7-1-45-53

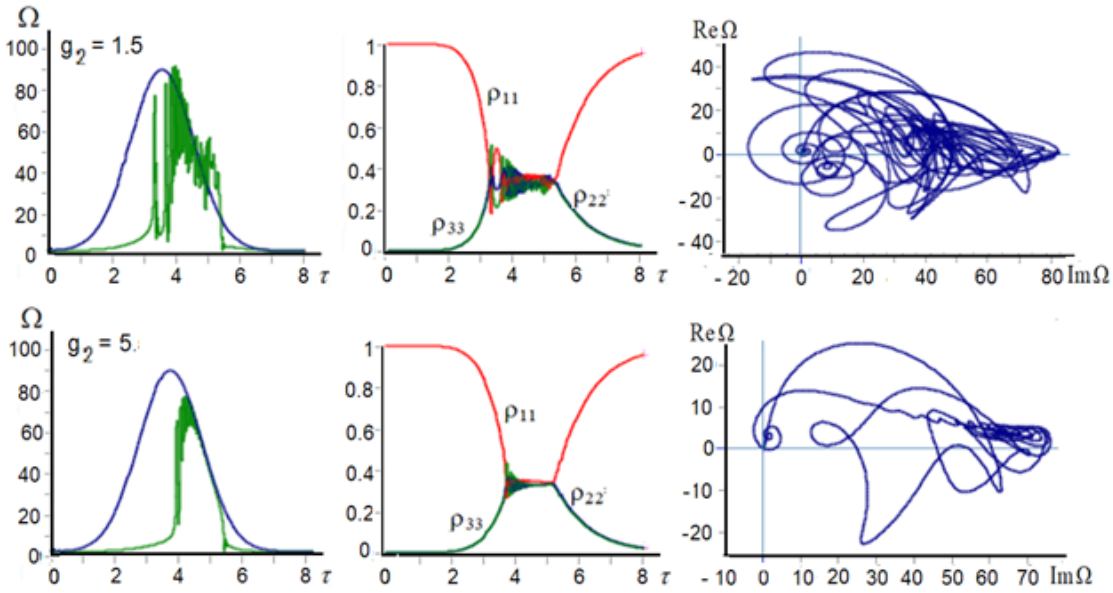

Fig. 8. Effect of phase relaxation on pulse generation by a supercrystal.
The supercrystal parameters are $\Delta_{31} = \Delta_{32}/2$, $\Delta_{32} = 40$, $\Delta_{21} = -20$, $\Delta_L = 1000$, $\gamma_R = 100$

Conclusions

Previous studies (Basov, Letokhov 1965; Frantz, Nodvik 1963; Kryukov, Letokhov 1970; Icsevgi, Lamb 1969; Hope, Scully 1969; Varnavskii et al. 1984) examined the propagation of a light pulse through a dense absorbing (or amplifying) medium. In such a medium, the propagation of an ultrashort light pulse alters the entire population of the electronic subsystem, leading to various coherent effects — coherent absorption, coherent amplification, self-induced transparency, photon echo, and others. All of them depend critically on the sample length.

In contrast, the interaction of a light pulse with a constant field amplitude and a supercrystal results in the generation of an optical response in the form of self-oscillations and dynamic chaos (Bayramdurdiyev et al., 2020).

When a Gaussian pulse interacts with a supercrystal, we observe the generation of single, double, and finite pulse trains whose durations are tens of times shorter than the exciting Gaussian pulse. This generation stems from the multistability and instability of the supercrystal's electronic quantum subsystem (Bayramdurdiyev et al., 2020), which arise from collective spontaneous emission (Arkhipov, Rozanov 2021), and, in our specific case, from both collective emission γ_R and the dipole-dipole interaction between quantum emitters Δ_L. Notably, the latter condition is an order of magnitude stronger than the collective interaction (superradiance) ($\Delta_L = 1000$, $\gamma_R = 100$).

The generation of a single ultrashort light pulse remains possible even in the presence of phase relaxation.

Thus, the results of this study on light pulse interaction with a supercrystal suggest that a V-type supercrystal can be recommended as a component in laser systems for generating single, binary, and train field pulses with durations tens of times shorter than of the input external pulse. The properties and effects of the supercrystal's optical response discussed here indicate that an ordered system of V-type quantum emitters holds considerable promise for applications in nanophotonics and in optical-based quantum computing.

Conflict of Interest

The authors declare that there is no conflict of interest, either existing or potential.

Author Contributions

All authors made an equivalent contribution to the preparation of this publication.

References

Abragam, A. (1963) *The Principles of Nuclear Magnetism*. Oxford: Clarendon Press, 599 p. (In English)

Arkhipov, R. M., Rozanov, N. N. (2021) Generation of extremely short pulses of terahertz radiation based on superradiation of a three-level resonant medium. *Optics and Spectroscopy*, 129 (3), 289–296. https://doi.org/10.21883/OS.2021.03.50659.274-20 (In Russian)

Baimuratov, A. S., Rukhlenko, I. D., Turkov, V. K. et al. (2013) Quantum-dot supercrystals for future nanophotonics. *Scientific reports*, 3, 1727. https://doi.org/10.1038/srep01727 (In English)

Basharov, A. (1988) Thin film of two-level atoms: A simple model of optical bistability and self-pulsation. *Journal of Experimental and Theoretical Physics*, 67 (9), 1741 (In English)

Basov, N. G., Letokhov, V. S. (1965) Propagation of a light pulse in an environment with an inversion. *Optics and Spectroscopy*, 18, 1042–1046. (In Russian)

Bayramdurdiyev, D. Ya., Malikov, R. F., Ryzhov, I. V., Malyshev, V. A. (2020) Nonlinear optical dynamics and high reflectance of a monolayer of three-level quantum emitters with a doublet in the excited state. *Zhurnal Eksperimental'noj i Teoreticheskoj Fiziki*, 158, 2 (8), 269–281. https://doi.org/10.31857/S0044451020080040 (In Russian)

Bekenstein, R., Pikovski, I., Pichler, H. et al. (2020) Quantum metasurfaces with atom arrays. *Nature Physics*, 16 (6), 676–681. https://doi.org/10.1038/s41567-020-0845-5 (In English)

Bloch, F. (1946) Nuclear Induction. *Physical Review*, 70, 460. https://doi.org/10.1103/PhysRev.70.460 (In English)

Boneschanscher, M. P., Evers, W. H., Geuchies, J. J. et al. (2014) Long-range orientation and atomic attachment of nanocrystals in 2D honeycomb superlattices. *Science,* 344 (6190), 1377–1380. https://doi.org/10.1126/science.1252642 (In English)

Bonifacio, R., Lugiato, L. A. (1975a) Cooperative radiation processes in two-level systems: Superfluorescence. *Physical Review A*, 11 (5), 1507–1521. https://doi.org/10.1103/PhysRevA.11.1507 (In English)

Bonifacio, R., Lugiato, L. A. (1975b) Cooperative radiation processes in two-level systems: Superfluorescence. II. *Physical Review A*, 12 (2), 587–598. https://doi.org/10.1103/PhysRevA.12.587 (In English)

Bonifacio, R., Schwendimann, P., Haake, F. (1971) Quantum statistical theory of superradiance. II. *Physical Review A*, 4, 302. https://doi.org/10.1103/PhysRevA.4.854 (In English)

Brewer, R. G., Shoemaker, R. L. (1971) Photo Echo and Optical Nutation in Molecules. *Physical Review Letters*, 27, 631–634. https://doi.org/10.1103/PhysRevLett.27.631 (In English)

Castro Neto, A. H., Guinea, F., Peres, N. M. R. et al. (2009) The electronic properties of grapheme. *Reviews of Modern Physics*, 81 (1), 109–162. https://doi.org/10.1103/RevModPhys.81.109 (In English)

Dicke, R. H. (1954) Coherence in Spontaneous Radiation Processes. *Physical Review*, 93, 99–110. https://doi.org/10.1103/PhysRev.93.99 (In English)

Ding, F., Bozhevolnyi, S. I. (2023) Advances in quantum meta-optics. *Materials Today*, 71 (1), 63–72. https://doi.org/10.1016/j.mattod.2023.07.021 (In English)

Efros, Al. L., Rosen, M., Kuno, M. et al. (1996) Band-edge exciton in quantum dots of semiconductors with degenerate valence band: dark and bright exciton states. *Physical Review B*, 54 (7), 4843–4856. https://doi.org/10.1103/PhysRevB.54.4843 (In English)

Frantz, L. M., Nodvik, J. S. (1963). Theory of pulse propagation in laser amplifier. *Journal of Applied Physics*, 34, 2346−2349. https://doi.org/10.1063/1.1702744 (In English)

Hope, F. A., Scully, M. O. (1969) Theory of an inhomogeneously broadened laser amplifier. *Physical Review*, 179, 339. https://doi.org/10.1103/PhysRev.179.399 (In English)

Icsevgi, A., Lamb, W. E. (1969) Propagation of light pulses in a laser amplifier. *Physical Review*, 185, 517. https://doi.org/10.1103/PhysRev.185.517 (In English)

Kasapi, A., Jain, M., Yin, G. Y., Harris, S. E. (1995) Electromagnetically induced transparency: Propagation dynamics. *Physical Review Letters*, 74 (13), 2447–2450. https://doi.org/10.1103/PhysRevLett.74.2447 (In English)

Kopvillem, U. H., Nagibarov, V. R. (1963) Light echo on paramagnetic crystals. *Fizika metallov i metallovedenie*, 15 (2), 313–315. (In Russian)

Kryukov, P. G., Letokhov, V. S. (1970) Propagation of a Light pulse in a Resonantly amplifying (absorbing) medium. *Uspekhi Fizicheskikh Nauk*, 12, 641–672. https://doi.org/10.3367/UFNr.0099.196910a.0169 (In Russian)

Kurnit, N. A., Abella, I. D., Hartmann, S. R. (1964) Observation of a Photon echo. *Physical Review Letters*, 13, 567–568. https://doi.org/10.1103/PhysRevLett.13.567 (In English)

Malikov, R. F., Malyshev, V. A. (2017) Optical bistability and hysteresis of a thin layer of resonant emitters: interplay of inhomogeneous broadening of the absorption line and the Lorentz local field. *Optics and Spectroscopy*, 122 (6), 955–963. https://doi.org/10.1134/S0030400X17060121 (In English)

Malikov, R. F., Malyshev, V. A. (2025) *Optical dynamics of an ensemble of quantum emitters*. Sankt Petersburg: Lan' Publ., 320 p. (In Russian)

Marangos, J. P. (1998) Electromagnetically induced transparency. *Journal of Modern Optics*, 45 (3), 471–503. https://doi.org/10.1080/09500349808231909 (In English)

McCall, S. L., Hahn, E. L. (1967) Self-Induced Transparency by Pulsed Coherent Light. *Physical Review Letters*, 18, 908–911. https://doi.org/10.1103/PhysRevLett.18.908 (In English)

Novoselov, K. S., Geim, A. K., Morozov, S. V. et al. (2004) Electric field effect in atomically thin carbon films. *Science*, 306, 666–669. https://doi.org/10.1126/science.1102896 (In English)

Ryzhov, I. V., Malikov, R. F., Malyshev, A. V., Malyshev, V. A. (2021) Quantum metasurfaces of arrays of Λ-emitters for photonic nano-devices. *Journal of Optics*, 23 (11), 115102. https://doi.org/10.1088/2040-8986/ac2788 (In English)

Ryzhov, I. V., Malikov, R. F., Malyshev, A. V., Malyshev, V. A. (2019) Nonlinear optical response of a two-dimensional quantum-dot supercrystal: Emerging multistability, periodic and aperiodic self-oscillations, chaos, and transient chaos. *Physical Review A*, 100 (3), 033820. https://doi.org/10.1103/PhysRevA.100.033820 (In English)

Solntsev, A. S., Agarwal, G. S., Kivshar, Y. S. (2021) Metasurfaces for quantum photonics. *Nature Photonics*, 15 (5), 327–336. https://doi.org/10.1038/s41566-021-00793-z (In English)

Soukoulis, C. M., Wegener, M. (2010) Optical metamaterials-More bulky and less lossy. *Science*, 330 (6011), 1633–1634. https://doi.org/10.1126/science.1198858 (In English)

Timoshchenko, E. V. (2023) *Modeling of nonlinear dynamics of the material response of dense optical layers to resonant radiation*. Mogilev: Mogilev state A. Kuleshov University Publ., 236 p. (In Russian)

Trifonov, E. D., Zaitsev, A. I., Malikov, R. F. (1979) Superradiance of an extended system. *Zhurnal eksperimentalnoj i teoreticheskoj fiziki*, 76 (1), 65–75. (In Russian)

Varnavskii, O. P., Kirkin, A. N., Leontovich, R. F. et al. (1984) Coherent amplification of ultrashort pulses in activated crystals. *Zhurnal eksperimentalnoj i teoreticheskoj fiziki*, 86 (4), 1227–1239. (In Russian)

Vlasov, R. A., Lemeza, A. M., Gladush, M. G. (2013) Resonance Fluorescence of optically dense ensembles of three-level resonant centers under conditions of energy-level population auto-oscillations. *Journal of Applied Spectroscopy*, 80 (3), 698–706. https://doi.org/10.1007/s10812-013-9829-x (In English)

Zheludev, N. I. (2010) The road ahead for metamaterials. *Science*, 328 (5978), 582–583. https://doi.org/10.1126/science.1186756 (In English)

Summaries in Russian / Информация о статьях на русском языке

Физика полупроводников

SERS-ЭФФЕКТ НА ПОВЕРХНОСТИ НАНОСТЕРЖНЕЙ ZnO, ПОКРЫТЫХ $CsPbBr_3$

Валерия Анатольевна Гущина, Евгений Павлович Аверочкин, Мария Александровна Теплоногова, Егор Александрович Лебедев, Сергей Александрович Козюхин

Аннотация. Гетероструктуры на основе наностержней ZnO и наночастиц $CsPbBr_3$ были исследованы с целью оценки их потенциала в качестве полупроводниковых SERS-субстратов. Было выявлено, что морфология ZnO определяет эффективность межфазного переноса энергии, увеличивая фотолюминесценцию при длине возбуждения 390 нм и вызывая снижение ширины запрещенной зоны в композитах. Анализ спектров комбинационного рассеяния выявил значительное усиление интенсивности и появление низкочастотных мод $CsPbBr_3$, выделенных с помощью гауссовой деконволюции, что подтверждает SERS-подобное поведение гибридных структур. Полученные результаты демонстрируют перспективность ZnO/$CsPbBr_3$-гетероструктур для сенсорики и оптоэлектронных приложений.

Ключевые слова: наностержни ZnO, наночастицы $CsPbBr_3$, SERS-эффект, комбинационное рассеяние света, гетероструктуры, перенос энергии, низкочастотные фононы

Для цитирования: Gushchina, V. A., Averochkin, E. P., Teplonogova, M. A., Lebedev, E. A., Kozyukhin, S. A. (2026) SERS effect on the surface of ZnO nanorods coated with $CsPbBr_3$. *Physics of Complex Systems*, 7 (1), 3–15. https://www.doi.org/10.33910/2687-153X-2026-7-1-3-15 EDN SOAOFH

ФОРМИРОВАНИЕ ДИМЕРОВ В ГАЗООБРАЗНОЙ ФАЗЕ GeTe КАК СПОСОБ ИЗГОТОВЛЕНИЯ ТОНКИХ КРИСТАЛЛИЧЕСКИХ ПЛЕНОК БЕЗ ВАКАНСИЙ

Александр Владимирович Колобов

Аннотация. Теллурид германия (GeTe) — многофункциональный материал, обладающий множеством полезных свойств. В частности, это один из лучших термоэлектрических материалов. На термоэлектрические свойства GeTe влияют вакансии на узлах Ge, которые всегда присутствуют в кристаллической фазе из-за низкой энергии образования таких дефектов. В этой работе, используя моделирование молекулярной динамики ab-initio, мы демонстрируем, что благодаря особой природе связей в этом материале, часто называемой резонансной и/или метавалентной, теллурид германия испаряется в виде гетеродимеров, а не отдельных молекул. Эта особенность GeTe может быть использована для изготовления ориентированных пленок GeTe без вакансий, когда материал термически испаряется на нагретую шаблонную подложку.

Ключевые слова: фазопеременные материалы, теллурид германия, первопринципная молекулярная динамика, резонансная связь, испарение, димеры

Для цитирования: Kolobov, A. V. (2026) The formation of dimers in the gaseous phase of GeTe as a way to fabricate vacancy-free crystalline thin films. *Physics of Complex Systems*, 7 (1), 16–21. https://www.doi.org/10.33910/2687-153X-2026-7-1-16-21 EDN YXMPGU

ВЛИЯНИЕ ПРЕКУРСОРОВ $K_2Cr_2O_7$ И NH_4I НА СОСТАВ, МОРФОЛОГИЮ И ТЕМНОВОЕ СОПРОТИВЛЕНИЕ ФОТОЧУВСТВИТЕЛЬНЫХ ЭЛЕМЕНТОВ НА ОСНОВЕ PbS

Кристина Сергеевна Макарук, Ирина Николаевна Мирошникова, Борис Николаевич Мирошников, Анатолий Игоревич Попов, Лариса Николаевна Маскаева, Лилия Сергеевна Волкова

Аннотация. Представлены результаты исследования структуры, морфологии и состава фоточувствительных элементов на основе тонких пленок сульфида свинца (PbS), полученных химическим осаждением в присутствии одного (дихромата калия — $K_2Cr_2O_7$) или двух (йодида аммония — NH_4I совместно с $K_2Cr_2O_7$) прекурсоров. По данным, полученным с помощью растровой электронной и атомно-силовой микроскопии, поверхность образцов, осажденных в присутствии только $K_2Cr_2O_7$, состоит из кристаллитов размером от 300 до 900 nm, обладающих кубической огранкой. Добавление в реакционную ванну NH_4I приводит к уменьшению размера зерен (более 75 % поверхности состоит из кристаллитов от 100 до 325 nm), появлению двух

процентов наноразмерных структур (до 100 nm) и изменению морфологии поверхности на более сглаженную. Установлено, что йод и его соединения приводят к существенному увеличению темнового сопротивления (в 10…250 раз), что, в свою очередь, обеспечивает увеличение чувствительности пленок.

Ключевые слова: сульфид свинца, тонкие пленки, морфология, химический метод осаждения, фоточувствительные элементы

Для цитирования: Makaruk, K. S., Miroshnikova, I. N., Miroshnikov, B. N., Popov, A. I., Maskaeva, L. N., Volkova, L. S. (2026) The effects of the precursors $K_2Cr_2O_7$ and NH_4I on the composition, morphology and dark resistance of photosensitive elements based on PbS. *Physics of Complex Systems*, 7 (1), 22–30. https://www.doi.org/10.33910/2687-153X-2026-7-1-22-30 EDN JKAFHD

ОСОБЕННОСТИ ЛЕГИРОВАНИЯ МЕДЬЮ КРИСТАЛЛОВ $PbSb_2Te_4$

Сергей Александрович Немов, Алексей Валерьевич Поволоцкий, Валентина Дмитриевна Андреева, Алексей Юрьевич Алябьев

Аннотация. В статье представлены результаты исследований методом рентгеновской дифракции и спектроскопии комбинационного рассеяния кристаллов $PbSb_2Te_4$, легированных медью, выращенных по методу Чохральского. Обсуждаются такие электрофизические свойства кристаллов, как концентрация собственных носителей заряда и термоэлектрическая добротность ZT. Обоснована необходимость введения донорной примеси для оптимизации свойств кристаллов как потенциального материала для термоэлектрического преобразования энергии. Отмечены особенности механизма легирования. Модель гетерогенной нуклеации Брамфитта применена для расчета отклонения параметров кристаллических решеток фаз, которые образуются в кристаллах в процессе роста. Предсказаны возможные фазы, содержащие медь. Экспериментально подтверждено наличие химически связанных атомов меди, образующих новые фазы, и их преимущественное расположение в ван-дер-ваальсовом зазоре между семи- и пятислойными пакетами.

Ключевые слова: полупроводники, $PbSb_2Te_4$, термоэлектричество, метод Чохральского, концентрация носителей, механизм легирования, модель гетерогенной нуклеации по Брамфитту, рентгеноструктурный анализ, спектры комбинационного рассеяния, семислойные пакеты

Для цитирования: Nemov, S. A., Povolotskiy, A. V., Andreeva, V. D., Aliabev, A. J. (2026) Features of copper doping of $PbSb_2Te_4$ crystals. *Physics of Complex Systems*, 7 (1), 31–35. https://www.doi.org/10.33910/2687-153X-2026-7-1-31-35 EDN DVYYWY

Теоретическая физика

ВОЗМОЖНОСТЬ ПЕРЕХОДА ОТ СТАНДАРТНОЙ ТЕМНОЙ ЭНЕРГИИ К ФАНТОМНОЙ ФАЗЕ В КОСМОЛОГИЧЕСКОЙ МОДЕЛИ FLRW: АНАЛИЗ ДИНАМИЧЕСКИХ СИСТЕМ

Виталий Дмитриевич Вертоградов, Ульяна Вадимовна Ямалтдинова

Аннотация. В работе исследуется динамика космологической эволюции в рамках метрики Фридмана–Леметра–Робертсона–Уокера (ФЛРУ) с нулевой кривизной пространства. Рассматривается четырёхкомпонентная модель Вселенной, включающая излучение, нерелятивистскую материю, стандартную тёмную энергию (с уравнением состояния $w \geq -1$) и фантомную энергию ($w < -1$). С использованием формализма автономных динамических систем показано, что фантомная энергия является глобально устойчивым будущим аттрактором: независимо от начальных условий, эволюция Вселенной неизбежно стремится к режиму доминирования фантомной компоненты, что ведёт к сингулярности типа «Большой разрыв». Анализ собственных значений матрицы Якоби подтверждает устойчивость фантомной точки при физически допустимых параметрах уравнения состояния. Результаты согласуются с современными наблюдательными указаниями на возможное пересечение барьера $w = -1$.

Ключевые слова: космология, тёмная энергия, фантомная энергия, модель ФЛРУ, динамические системы, уравнение состояния

Для цитирования: Vertogradov, V. D., Yamaltdinova, U. V. (2026) Potential for a transition from standard to phantom dark energy in the FLRW cosmology: A dynamical systems analysis. *Physics of Complex Systems*, 7 (1), 36–44. https://www.doi.org/10.33910/2687-153X-2026-7-1-36-44 EDN DMXJNM

ВЗАИМОДЕЙСТВИЕ УЛЬТРАКОРОТКИХ ИМПУЛЬСОВ СВЕТА С АНСАМБЛЕМ КВАНТОВЫХ V- ИЗЛУЧАТЕЛЕЙ

Давут Язмуратович Байрамдурдыев, Рамиль Фарукович Маликов

Аннотация. Проводится теоретическое исследование оптического отклика 2D суперкристалла квантовых излучателей с дублетом в возбужденном состоянии (V-излучателей) на воздействие монохроматического внешнего поля в виде гауссовского импульса поля. Изучена динамика отклика в зависимости от площади входного поля. Показано, что импульсы воздействующего на суперкристалл поля приводят к генерации одиночных, двойных, тройных и цуга импульсов с длительностями в десятки раз меньшими, чем длительность возбуждающих импульсов поля. Показано, что генерация одиночных ультракоротких импульсов не зависит от величины возбуждения населенностей и может реализоваться и при наличии фазовой релаксации. Рассмотренные свойства и эффекты оптического отклика суперкристалла позволяют надеяться, что данная система может оказаться перспективной для приложений в области нанофотоники и квантовых вычислений.

Ключевые слова: 2D-сверхрешётка, суперкристалл, метаповерхность, трёхуровневые квантовые излучатели, квантовые точки, автоколебания, V-схема, взаимодействие импульсов света с двумерными кристаллами, генерация оптических импульсов, фазовая релаксация

Для цитирования: Bayramdurdiyev, D. Ya., Malikov, R. F. (2026) Interaction of ultrashort light pulses with an ensemble of quantum V-emitters. *Physics of Complex Systems*, 7 (1), 45–53. https://www.doi.org/10.33910/2687-153X-2026-7-1-45-53 EDN DQWTCV